PREDICTION OF MATERIAL FRACTURE TOUGHNESS AS FUNCTION OF MICROSTRUCTURE

A Dissertation
Presented to
The Academic Faculty

by

Yan Li

In Partial Fulfillment
of the Requirements for the Degree
Doctor of Philosophy in the
School of Mechanical Engineering

Georgia Institute of Technology
December, 2014

PREDICTION OF MATERIAL FRACTURE TOUGHNESS AS FUNCTION OF MICROSTURCTURE

Approved by:

Dr. Min Zhou, Advisor
G.W.W. School of Mechanical Engineering
Georgia Institute of Technology

Dr. Ting Zhu
G.W.W. School of Mechanical Engineering
Georgia Institute of Technology

Dr. David L. McDowell
G.W.W. School of Mechanical Engineering
Georgia Institute of Technology

Dr. Shuman Xia
G.W.W. School of Mechanical Engineering
Georgia Institute of Technology

Dr. Richard W. Neu
G.W.W. School of Mechanical Engineering
Georgia Institute of Technology

Dr. Donald S. Shih
Boeing Research & Technology
The Boeing Company

Date Approved: July 31, 2014

To my parents and grandma

ACKNOWLEDGEMENTS

Foremost, I would like to express my sincere gratitude to my advisor Dr. Min Zhou for his continuous support of my Ph.D study and research. His patience, motivation, enthusiasm, and immense knowledge have greatly influenced me and made me determined to be a faculty member. I am also grateful for the hospitality of his family when I first came to the U.S.

I also would like to thank my thesis committee members, Dr. David McDowell, Dr. Rick Neu, Dr. Ting Zhu, Dr. Shuman Xia and Dr. Donald Shih, for their encouragement and insightful comments on my thesis.

I feel privileged to have had the opportunity to work on research projects supported by the NSF Center for Computational Materials Design (CCMD) at Georgia Institute of Technology and Pennsylvania State University. Specially, working with my mentors Dr. Donald Shih from the Boeing Company, and Dr. Mark Moss and Dr. Ed Nixon from the Gulfstream Company, have provided me a deep insight of how fundamental research at universities can lead into real industrial applications. I also would like to thank Ms. Sandra Watson and Ms. Cecelia Jones for their help and great assistance.

I would like to sincerely thank my friends and colleagues at Georgia Tech. I have been very fortunate to have worked with such talented members: Dr. Yifan Gao, Dr. Ananda Barua, Chris Lammi, Seokpum Kim, Siddharth Avachat, Barrett Hardin, Jong Boo Jung and David Weichsel. Also I would like to thank my friends in the Mechanics of

Materials group at Georgia Tech: Dr. Yuan Zhong, Dr. Shan Huang, Dr. Brett Ellis, Dr. Jeff Lloyd, Dr. Bill Musinski, Dr. Michael Kirka, Sam Britt, Matthew Priddy, Ben Smith, Feifei Fan, Xueju Wang, Zhi Zeng, Ran Liu and Yuan Li. Their company really made my PhD life much more enjoyable than I could have imagined.

Last but not least, I would like to thank my parents Shunqing Li and Qiaohuan Liu as well as my grandma Huanyou Wang. Thank you so much for your unconditional love, support and encouragement. You make my life beautiful and meaningful.

TABLE OF CONTENTS

Page

LIST OF TABLES

Page

LIST OF FIGURES

Page

LIST OF SYMBOLS

α, β	Dundurs parameters
a_d	crack extension length along an interface
a_p	crack extension length into reinforcement
A	crack area
$d_{\max}$	maximum distance of a reinforcement particle
D	crack propagation distance
ε	bi-elastic constant
E_i	Young's modulus (i = 0 or 1)
$\bar{E}$	effective Young's modulus of the composite material
f	volume fraction
H_m, H_{in}, H_p	fractions of matrix cracking, interface debonding and particle cracking
H_G, H_{GB}	fractions of transgranular and intergranular fracture
$\Phi_m, \Phi_{in}, \Phi_p$	surface energy of matrix cracking, interface debonding and particle cracking
Φ_G, Φ_{GB}	surface energy of grains and grain boundaries
J_d, J_p	energy release rates for crack deflection and crack penetration
K_i	bulk modulus (i = 0 or 1)
K_{IC}^i	initiation fracture toughness

K_{IC}	propagation fracture toughness
K^0	normalization factor
K^L	lower bound fracture toughness
K	complex stress intensity factor
K_1, K_2	mode I and mode II stress intensity factors
k_I	amplitude factor
ξ	crack length multiplication factor (CLMF)
μ_i	shear modulus (i = 0 or 1)
n	number of reinforcement particles
λ	state variable for interfacial separation
P_{ij}	two-point correlation functions (i = 0 or 1; j = 0 or 1)
p	crack deflection probability
$\bar{\rho}$	mean reinforcement particle roundness
$Q_1(Q_2)$	interfacial bonding strength ratio
r_p	plastic zone size
R	particle radius
s	characteristic reinforcement size
$T_{\max}^{in}$	interfacial bonding strength
$T_{\max}^0$	baseline reference bonding strength
$T_{\max}\big\|_G$	cohesive strength in the grains
$T_{\max}\big\|_{GB}$	cohesive strength along the grain boundaries

U_0	parameter in He and Hutchinson's crack deflection criterion
U	parameter in modified crack deflection criterion
U_f	total fracture energy released
X	probability of fracture
Δ_{tc}	critical tangential separation
Δ_{nc}	critical normal separation
v_i	Poisson's ratio (i = 0 or 1)
$\overline{v}$	effective Poisson's ratio of the composite material
V	crack speed
ω	crack incident angle
ω_0	critical crack angle for crack deflection
W	total projected crack length

SUMMARY

Microstructure determines fracture toughness of materials through the activation of different fracture mechanisms. To tailor the fracture toughness through microstructure design, it is important to establish relations between microstructure and fracture toughness. To this end, systematic characterization of microstructures, explicit tracking of crack propagation process and realistic representation of deformation and fracture at different length scales are required. A cohesive finite element method (CFEM) based multiscale framework is proposed for analyzing the effect of microstructural heterogeneity, phase morphology, texture, constituent behavior and interfacial bonding strength on fracture toughness. The approach uses the *J*-integral to calculate the initiation/propagation fracture toughness, allowing explicit representation of realistic microstructures and fundamental fracture mechanisms.

Both brittle and ductile materials can be analyzed using this framework. For two-phase Al_2O_3/TiB_2 ceramics, the propagation fracture toughness is improved through fine microstructure size scale, rounded reinforcement morphology and appropriately balanced interphase bonding strength and compliance. These microstructure characteristics can promote interface debonding and discourage particle cracking induced catastrophic failure. Based on the CFEM results, a semi-empirical model is developed to establish a quantitative relation between the propagation toughness and statistical measures of microstructure, fracture mechanisms, constituent and interfacial properties. The analytical model provides deeper insights into the fracture process as it quantitatively predicts the proportion of each fracture mechanism in the heterogeneous microstructure. Based on the

study on brittle materials, the semi-analytical model is extended to ductile materials such as AZ31 Mg alloy and Ti-6Al-4V alloy. The fracture resistance in these materials not only depends on the crack surfaces formed during the failure process, but also largely determined by the bulk plastic energy dissipation. The CFEM simulation permits surface energy release rate to be quantified through explicit tracking of crack propagation in the microstructure. The plastic energy dissipation rate is evaluated as the difference between the predicted J value and the surface energy release rate. This method allows competition between material deformation and fracture as well as competition between transgranular and intergranular fracture to be quantified. The methodology developed in this thesis is potentially useful for both the selection of materials and tailoring of microstructure to improve fracture resistance.

1 INTRODUCTION

1.1 Background and Motivation

Material fracture is the major cause of structure degradation, which can lead to serious hazards such as plane crash, pipe leakage and bridge collapse, etc. In 1983, the National Bureau of Standards and Battelle Memorial Institute estimated that the annual cost of structural failure due to fracture was $119 billion dollars. Other costs, such as loss of life, personal injury, and damaged reputations were unmeasured, but obviously could be devastating to individuals, companies, and maybe entire industries [1].

In order to prevent fracture induced failure, several approaches have been proposed in engineering practices. Traditionally, a strength based approach, which assumes a pristine, flaw-free material, is employed in the structural design. A material with strength greater than the expected applied stress is considered as adequate. However, this approach has been proved to be unreliable in real structure design and material selection. First of all, every material has flaws, which can be in the form of large, visible cracks or almost undetectable microcracks. These flaws could be inherent in defective materials, introduced during the manufacturing process, or created by extreme environmental conditions during operation. Besides, the presence of flaw cracks modifies the local stresses to an extent that the strength based material approach is not accurate in evaluating the reliability of the structure. When a crack reaches a certain critical length, it can propagate catastrophically through the structure, even though the gross stress is much less than would normally cause yield or failure in the material.

In contrast to the strength based approach, fracture mechanics provides a more rational basis to describe the actual material behavior and the reliability of structures. It employs concepts from applied mechanics and material science to assess structural integrity by assuming the presence of a crack. In addition, this approach considers the combined effect of applied stress; location, size, and shape of cracks; and the resistance of the material to crack growth.

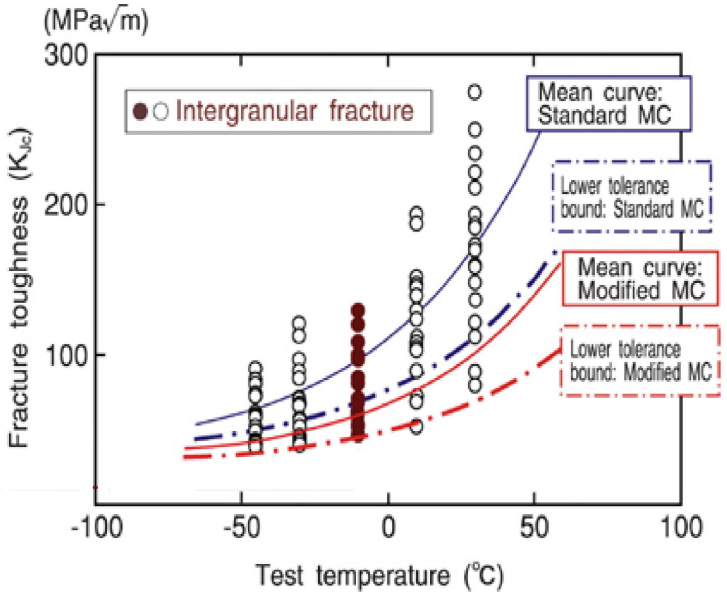

Fig. 1.1 Scattering of fracture toughness under different test temperatures. Identical sample configurations and loading conditions are maintained under each test temperature. Reproduced from Ref. [2].

Although fracture mechanics has been very successful in analyzing crack propagation at the structure level, it does not include fundamental physics that governs the failure process. Firstly, fracture mechanics fails to capture the multiscale nature of material fracture. This approach only focuses at the macrostructural scale and cannot account for stochastic variations of material behavior which is intrinsic at the

microstructural level. For example, scattering of fracture toughness is observed for samples with identical material configurations and loading conditions, as shown in Fig. 1.1. This is in contradiction with predictions using fracture mechanics approach.

It has been proved that microstructural constitutes, phase morphology, phase distribution and texture ultimately determine the material fracture toughness through activation of different failure mechanisms [3-5]. Therefore, the fundamental avenue for designing structure material with improved toughness is to tailor microstructure with designated properties. Tasks in this regard include proper characterization of microstructures and quantitative correlation of microstructural attributes with overall material response. Most analytical models allow the macroscopic response of materials to be estimated but yet do not allow the predictions of response that are unknown a priori. Such models usually require extensive experimental data to calibrate parameters that have little or no physical significance [6]. Experimental studies can quantify macroscopic behavior and establish response-microstructure relations, but cannot be used to explore material configurations not yet in existence. The trial-and-error empirical approach for materials development is associated with high cost and long cycles. Computational modeling and simulation can provide an alternative and allow exploration of material configurations not yet in existence. The advent of parallel computing greatly contributed to the development of multiscale modeling with more degrees of freedom being resolved efficiently and accurately. A review of multiscale modeling approaches in fracture analysis is presented in Section 1.2.

1.2 Review of Multiscale Modeling Methods in Fracture Analysis

The recent rapid growth in multiscale modeling arose from the confluence of parallel computing power and experimental capabilities to characterize structure-property relations across different length scales [7]. This section summarizes some of the latest developments in multiscale modelling techniques over the past decade, as applied to fracture analysis.

So far, two different multiscale methodologies exist in the solid mechanics continuum theory paradigm: hierarchical and concurrent. The key difference lies in the bridging methodology. In concurrent methods, the bridging methodology is numerical or computational in nature. In the hierarchical methods, numerical techniques are independently run at disparate length scales. Then, a bridging methodology such as statistical analysis methods, homogenization techniques, or optimization methods can be used to distinguish the pertinent cause-effect relations at the lower scale to determine the relevant effects for the next higher scale [8].

1.2.1 Hierarchical methods

Most of the current hierarchical methods employ the thermodynamically constrained Internal State Variables (ISVs) to address microstructure-property relations across different length scales. It is a top-down approach, meaning the ISVs exist at the macroscale but can reach down to various subscales to receive pertinent information [9]. Talrejia [10] developed a continuum model for determining mechanical response of ceramic matrix composites with elementary damage entities, i.e. cracks, debonds and

slipped surfaces regarded as internal variables. Gailly and Espinosa [11] proposed a multiple-plane-microcracking (MPM) model to track microcracking on 13 orientations under high pressure, high strain rate and high deformation. This model provides the elastic and inelastic response of the material before massive crack coalescence. For viscoelastic materials, such as polymers, the time dependent fracture behavior requires coupling among thermal, mechanical and other physicochemical effects. Yoon and Allen [12] developed a cohesive fracture model into an ISV formulation for nonlinear viscoelasticity materials. Chen [13] introduced a consistent thermodynamic formulation of a coupled hygro-thermo-viscoelastic fracture theory from the global energy balance equation and the requirement of non-negativity of the global energy dissipation rate. The crack parameter is first introduced as an internal state variable in the Helmholtz free energy functional expression depending on the histories of strain, temperature and fluid concentration.

In addition to the top-down internal state variable methods, the bottom-up methods emerge as a more appealing method for the development of new materials. Leng et al. [14] used a bottom-up numerical method to explore the dynamic impact fracture behavior of nanoparticle-reinforced composites. Rinaldi [15] provides a physically based solution that starts from the direct consideration of the microscale properties and, in a bottom-up view, recovers a continuum elastic description of quasi-brittle solids. The microscale data from simulations are used to identify the “exact” (macro-) damage parameter and to build up the (macro-) Helmholtz function for the equivalent elastic model.

1.2.2 Concurrent methods

Compared with hierarchical methods, concurrent methods try to combine different scale algorithms together with matching procedures invoked in some overlapping domain [8]. Typical concurrent methods include two different length scales.

Research in this area initially focuses on the coupling between the atomistic and continuum scale. Gumbsch [16] introduced a Finite Element-Atomistic (FEAt) coupling scheme to study brittle fracture under opening mode and mixed mode loading conditions. The core region near the crack tip is analyzed using atomistic simulations with appropriate boundary conditions while the region away from the crack tip is analyzed using FEA. The embedded atom method (EAM) potentials are employed in the transitional region to examine fracture in brittle materials under dynamic loads. In addition to Gumbsch's work, Coarse Grained Molecular Dynamics (CGMD) method [17, 18], Quasicontinuum (QC) method [19] and Coupling of Length Scales (CLS) method [20] are widely used to couple the atomic scale to the continuum scale. A later research by Bazant [21] argued that these atomistic-finite element multiscale methods fail to capture the physics of cracking and frictional slip in the mesostructure of concrete or the propagation of a softening kink band in fiber composites. Therefore, it is equally important to analyze the material fracture behavior at microstructure-structure level. Zhai et al. [22] developed a computational framework that allows representation of material microstructure and explicit account of different deformation and fracture mechanisms at microscale. Based on their work, Li and Zhou [23, 24] have developed an approach for evaluating the overall fracture toughness of materials based on a resolution of deformation and fracture processes at the microstructure level, accounting for

microscopic heterogeneity and hierarchy. The detailed microstructure-fracture toughness correlations will be discussed in Chapter 4.

1.3 Objective, Scope and Organization of This Thesis

The major objectives of this thesis are to:

1) Development and improvement of algorithms for relating microstructural characteristics such as crystalline response, composition, size scale, microstructure hierarchy, morphology, texture and constituent properties to failure resistance of materials as characterized by fracture toughness.

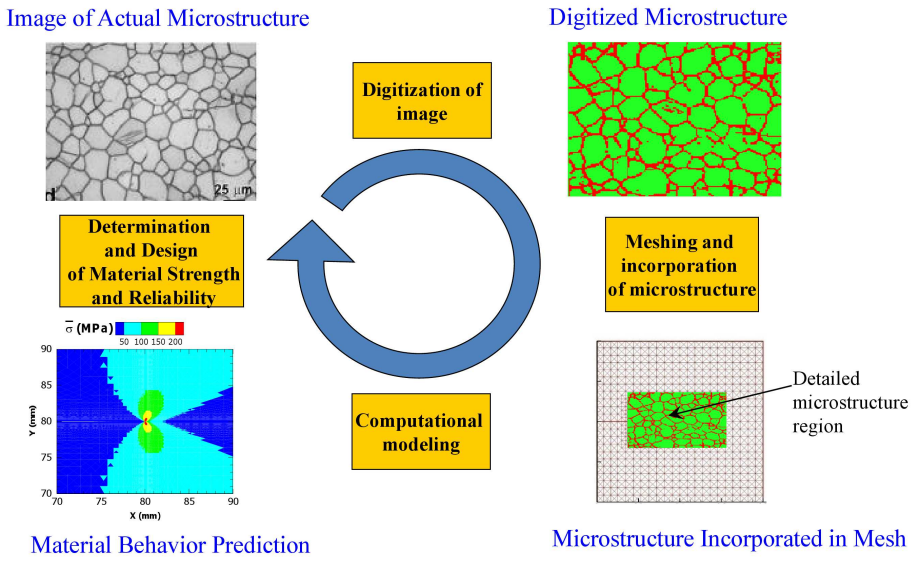

Fig. 1.2 Scheme of 2D multiscale material design framework.

2) Development of 2D and 3D representations of actual microstructures of materials with digitization of bulk constituents, precipitates, and interfaces (grain and phase boundaries) for explicit tracking of heterogeneous deformation and fracture processes.

3) Development of tools for microstructure characterization using two-point correlation functions reflecting the hierarchy of material structure heterogeneity.

4) Development of computational framework which allows fracture toughness optimization through iterative design processes. A 2D multiscale material design framework is illustrated in Fig. 1.2. A software, which includes 2D/3D microstructure generation/characterization/reconstruction, constitutive modeling, finite element analysis, and material property evaluation is developed to implements complex algorithms into design decisions. The GUI interface is shown in Fig. 1.3. This tool is not only useful for commercialization purposes, but also helpful for educating people with a broad, industrially relevant perspective on engineering research and practice.

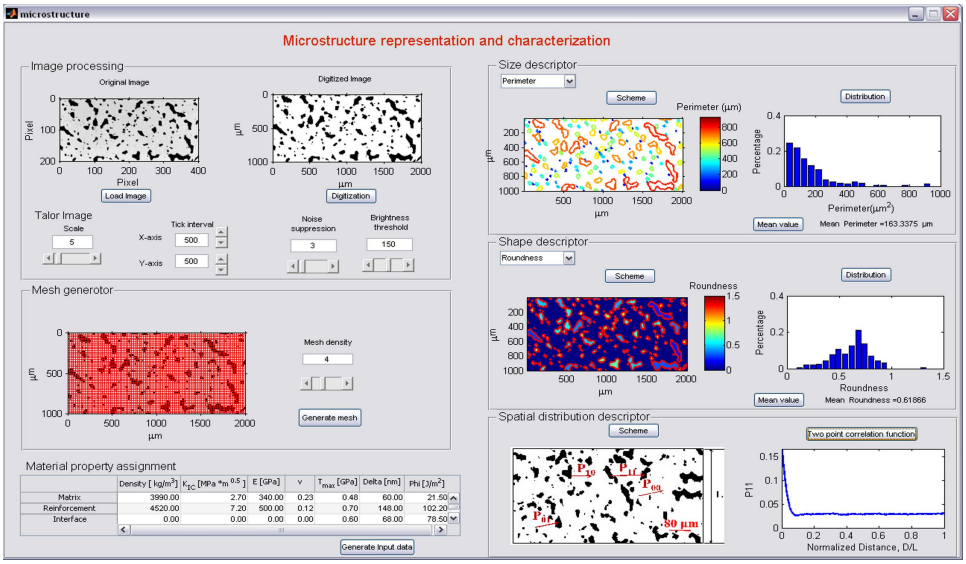

Fig. 1.3 GUI interface of the material design software.

Chapters 2 is dedicated to the objective 1 by establishing the cohesive finite element method (CFEM) based multiscale framework. The material fracture toughness,

which is predicted by calculating *J*-integral, considers microstructures with random heterogeneous phase distributions and fracture processes with arbitrary crack paths or micro-crack patterns. Objective 2 and 3 are achieved in Chapter 3. Microstructures with systematically varying attributes will be generated and characterized. Chapter 4 and chapter 5 focus on the microstructure-fracture mechanism-fracture toughness relations for both brittle and ductile materials. These conclusions can be used in the selection of materials and the design of new materials with tailored properties.

2 CFEM-BASED MULTISCALE FRAMEWORK

2.1 Introduction

In this chapter, a Cohesive Finite Element Method (CFEM) based multiscale framework is developed to evaluate material fracture toughness through simulation of fracture processes in microstructures. Using this framework, an approach for evaluating the overall fracture toughness of material is developed based on a resolution of deformation and fracture processes at the microstructure level, accounting for microscopic heterogeneity and hierarchy. This approach uses the *J*-integral to quantify the fracture resistance as a function of microstructural attributes. It also provides a means for calibrating model parameters at the microscale through macroscale responses which can be easily measured in experiments.

Section 2.2 provides detailed mathematical formulation of cohesive element. The implementation of cohesive elements in finite element modeling is discussed in Section 2.3. Both 2D and 3D framework will be presented in Section 2.4. The approach to evaluate material fracture toughness through calculation of *J*-integral is introduced in Section 2.5.

2.2 Cohesive Finite Element Formulation

Within this framework, two CFEM approaches exist for resolving fracture processes when crack paths are not known in advance. One is to insert cohesive elements ahead of the crack tip as crack develops [25, 26]. This method can avoid cohesive-surface-induced stiffness reduction of the overall model when the traction-separation

relation has finite initial stiffness. However, it is computationally expensive and requires specific fracture initiation criteria that are extrinsic to the overall finite element model. Another method entails embedding cohesive surfaces along all finite element boundaries as part of the physical model (Needleman [27], Xu and Needleman [28, 29] and Zhai et al. [30]). The cohesive surfaces permeate the whole microstructure as an intrinsic part of material characterization. Constitutive relations for the bulk phases and cohesive surfaces are specified separately. The cohesive relation allows damage and crack surface separation to be considered. Fracture emerges as a natural outcome of the deformation process without the use of any failure criterion. Although cohesive-surface-induced stiffness reduction is inevitable for this method if a cohesive relation with a finite initial stiffness is employed, proper choice of cohesive surface stiffness and finite element size [31] can effectively alleviate and minimize its influence on computational results.

In this study, the constitutive law of the cohesive element takes the form of a bilinear relation between traction and interfacial separation, as illustrated in

Fig. 2.1. The bilinear law used can be regarded as a generalized version of those with irreversibility given by Camacho and Ortiz [32] and Ortiz and Pandolfi [33]. However, as in Espinosa et al. [34], additional parameters are needed to define the finite initial stiffness of the cohesive surfaces and the irreversibility of separation with damage. This law is derived from a potential Φ which is a function of separation vector Δ through a state variable defined as $\lambda = \sqrt{\left(\Delta_n/\Delta_{nc}\right)^2 + \left(\Delta_t/\Delta_{tc}\right)^2}$. This variable describes the effective instantaneous state of mixed-mode separations. Here, $\Delta_n = \mathbf{n}\cdot\boldsymbol{\Delta}$ and $\Delta_t = \mathbf{t}\cdot\boldsymbol{\Delta}$ denote, respectively, the normal and tangential components of $\boldsymbol{\Delta}$, with $\mathbf{n}$ and $\mathbf{t}$

being unit normal and tangent vectors. For 3D cohesive element, Δ_t is further defined as

$$\Delta_t = \sqrt{\left(\Delta_p\right)^2 + \left(\Delta_q\right)^2} = \sqrt{\left[\left(\boldsymbol{\Delta} - \left(\boldsymbol{\Delta}\cdot\mathbf{n}\right)\mathbf{n}\right)\cdot\mathbf{p}\right]^2 + \left[\left(\boldsymbol{\Delta} - \left(\boldsymbol{\Delta}\cdot\mathbf{n}\right)\mathbf{n}\right)\cdot\mathbf{q}\right]^2} = \left|\boldsymbol{\Delta} - \left(\boldsymbol{\Delta}\cdot\mathbf{n}\right)\mathbf{n}\right| \quad \text{with}$$

$\mathbf{p}$ and $\mathbf{q}$ being two unit tangential vectors. Note that $\mathbf{n}$, $\mathbf{p}$ and $\mathbf{q}$ are mutually orthogonal to each other and form a right-handed triad. Δ_{nc} is the critical normal separation at which the cohesive strength of an interface vanishes under conditions of pure normal deformation ($\Delta_t = 0$). Similarly, Δ_{tc} is the critical tangential separation at which the cohesive strength of an interface vanishes under conditions of pure shear deformation ($\Delta_n = 0$). $T_{\max}$ represents the maximum traction that the cohesive element can sustain at the onset of irreversible separation.

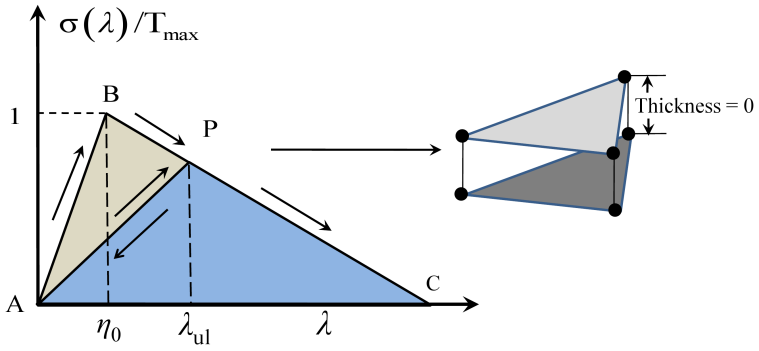

Fig. 2.1 Bilinear traction separation law.

In order to account for the irreversibility of separations, a parameter $\eta = \max\{\eta_0, \lambda_{ul}\}$ is defined. As illustrated in Fig. 2.1, η_0 is the initial value of η which defines the stiffness of the original undamaged cohesive surface, while λ_{ul} is the hitherto

maximum value of λ at which an unloading process was initiated. It should be noted that λ_{ul} is associated with the onset of an unloading event and is not necessarily the hitherto maximum value of λ. λ_{ul} represents the current (reduced) stiffness of the cohesive surfaces after damage and unloading have occurred. Furthermore, η_0 represents the characteristic value of effective separation λ at which the effective traction σ for a cohesive surface pair reaches the strength $T_{\max}$ of the undamaged surface. λ_{ul} stands for the critical level of λ at which σ reaches the reduced strength $T_{\max}(1-\eta)/(1-\eta_0)$ of the hitherto damaged cohesive surface pair. As indicated in Fig. 2.1 separation occurs elastically and the cohesive energy stored (work done in causing separation) is fully recoverable between A and B ($0 \le \lambda \le \eta_0$). Damage in the form of microcracks and other small-scale defects does not occur. Between B and C ($\eta_0 \le \lambda \le 1$), material degradation causes progressive reduction in the strength of the cohesive surfaces. This represents a phenomenological account of the effects of microcracks and other defects not explicitly modeled in the CFEM model. Unloading from any point P follows path PA and subsequent reloading follows AP and then PC. Part of the work expended on causing the separation in this regime is irreversible, as indicated by the hysteresis loop ABP which implies dissipation during the softening process. Correspondingly, there is a decrease in the maximum tensile strength of the cohesive surface. This is reflected in the elastic reloading of the interface along AP and further softening along path PC.

The specific expression for potential Φ is of the form

$$\Phi = \Phi(\lambda,\eta) = \begin{cases} \Phi_0 \left(\dfrac{1-\eta}{1-\eta_o}\right)\left(\dfrac{\lambda^2}{\eta}\right), & \text{if } 0 \le \lambda \le \eta, \\ \Phi_0 \left(\dfrac{1-\eta}{1-\eta_o}\right)\left(1-\dfrac{(1-\lambda)^2}{1-\eta}\right), & \text{if } \eta \le \lambda \le 1, \\ 0, \qquad \text{if } \lambda > 1. \end{cases} \tag{2.1}$$

The work per unit interface area for an arbitrary separation process is

$$\int_0^{\Delta_c} \mathbf{T} \cdot \mathrm{d}\,\boldsymbol{\Delta} = \Phi(1,\eta) = \frac{1}{2} \mathrm{T}_n^{\max} \Delta_{nc} = \frac{1}{2} \alpha \mathrm{T}_t^{\max} \Delta_{tc}, \tag{2.2}$$

where α is defined as $\Delta_{nc} / \Delta_{tc}$ and is assumed to be 1.

CFEM models with cohesive traction-separation laws with finite initial stiffness have two competing requirements on element size. The upper bound requires that the element size must be small enough to accurately resolve the stress distribution inside the cohesive zones at crack tips. The lower bound, on the other side, requires the cohesive surface induced stiffness reduction be small, such that the wave speed in the solid is not significantly affected due to the presence of the cohesive surfaces. For the conditions of this paper, the preferred range of the element size is $7\,\mu m \ll h \ll 14\,\mu m$, allowing the convergence criterion in Tomar et al. [31] to be satisfied.

2.3 2D Model Structure

Models at the macrostructural scale cannot account for material heterogeneity at the microstructural scale. The use of homogenized material properties yields results that do not reflect stochastic variations of material behavior which is intrinsic at the microstructural level. Such models cannot and do not attempt to explain the statistical variation in quantities such as K_{IC} [35]. On the other hand, models at the microstructual scale account for material heterogeneity and resolve different deformation and failure mechanisms. Such models have fine resolutions and, as a result, are computationally intensive and are impractical for use at the structural scale.

The computational framework developed here combines both scales and overcomes the shortcomings of each type of models. At the micro scale, it allows explicit representation of microstructures and account of microstructural level of deformation, damage and failure mechanisms. At the macro scale, it allows macroscopic conditions such as controlled loading and structural response to be considered at the same time. The 2D modeling aspects including specimen configuration, mesh generation algorithms and cohesive element insertion will be discussed in detail in this section.

2.3.1 2D configuration

The edge-cracked 2D square specimen under Mode I tensile loading is illustrated in Fig. 2.2. The entire specimen has a size length of 3.65 mm. The microstructure region has a length of 2 mm, width of 1 mm and a pre-crack length of 0.73 mm. A boundary velocity between $\mathrm{v} = 5\times10^{-4}\,\mathrm{mm/s}$ and $\mathrm{v} = 15\,\mathrm{mm/s}$ is imposed at the top and bottom

edges to effect tensile loading. The remaining edges of the specimen are traction-free. Conditions of plane strain are assumed to prevail.

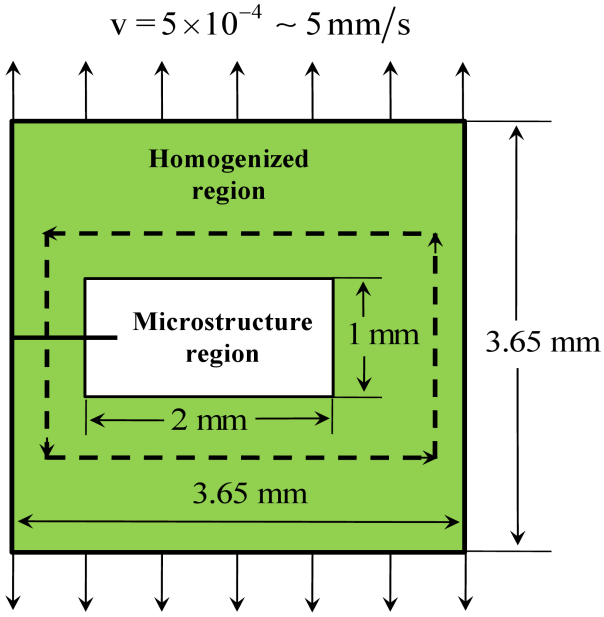

Fig. 2.2 2D specimen configuration used in the analysis.

Although the 2D framework developed here can be applied to any material system in principle, this section primarily focuses on Al_2O_3/TiB_2 ceramic composites.

Both the Al_2O_3 matrix and TiB_2 reinforcements in the composites follow isotropic linear elastic constitutive relations. Specifically, the constitutive law is

$$\boldsymbol{\sigma} = \frac{E}{1+\nu}\boldsymbol{\varepsilon} + \frac{\nu E}{(1+\nu)(1-2\nu)}\,\mathrm{tr}(\boldsymbol{\varepsilon})\mathbf{I}, \tag{2.3}$$

where $\boldsymbol{\sigma}$ and $\boldsymbol{\varepsilon}$ are the stress and strain, respectively, E is Young's modulus. ν is Poisson's ratio, $\mathrm{tr}(\boldsymbol{\varepsilon})$ is the trace of $\boldsymbol{\varepsilon}$ and $\mathbf{I}$ is the second order identity tensor. The values of the material constants for the constituents are summarized in Table 1.

Table 1. Constitutive parameters for bulk constituents and cohesive surfaces

Compound	Density (kg/m^3)	K_{IC} $(MPa\sqrt{m})$	E (GPa)	ν	T_{max} (GPa)	Δ_{tc} ,Δ_{nc} (nm)	Φ (J/m^2)
Al_2O_3	3990	2.7	340	0.23	0.48	90	21.5
TiB_2	4520	7.2	500	0.12	0.70	292	102.2
Interface					0.60	262	78.5

2D cohesive elements with 4-node zero thickness (COH2D4) permeate the entire microstructure representation. The parameters for the bilinear cohesive law are chosen such that the work of separation matches experimentally measured fracture toughness values for the corresponding constituent. For Al_2O_3/TiB_2 composites, three types of cohesive elements exist: Al_2O_3-Al_2O_3, TiB_2-TiB_2 and Al_2O_3-TiB_2. Xu and Needleman [36] suggested that the maximum traction $T_{\max}$ should be between $E/100$ and $E/200$. Therefore, Δ_{nc} and Δ_{tc} can be determined from Eqn (2.2). For linear elastic materials, $\Phi = G_{IC} = J_{IC} = \left[\left(1-\nu^2\right)/E\right]K_{IC}^2$, where K_{IC} is the fracture toughness of the material in question. According to the experimental results reported by Logan [37] and Wiederhorn [38], the K_{IC} values of the matrix Al_2O_3 and the reinforcement TiB_2 are chosen as 2.7 $MPa\sqrt{m}$ and 7.2 $MPa\sqrt{m}$, respectively. The cohesive strength $T_{\max}$ for each phase is calibrated accordingly to satisfy the fracture toughness of the single phase. Since the experimental K_{IC} value for the interface is not yet available in the current literature, its

cohesive strength $T_{\max}$ is considered as the average value of the matrix and reinforcement cohesive strength in most of the calculations unless specified. The effect of interfacial strength will be discussed in detail in Chapter 4. All the constitutive parameters for the bulk constituents and cohesive surfaces are listed in Table 1.

There are several methods to evaluate the effective properties of composite materials. The most popular ones include Eshelby method, Mori-Tanaka Method and self-consistent method. All the above methods ignore the size and spatial distribution of the inhomogeneities. The effective bulk and shear moduli in the Eshelby method are

$$\begin{cases} \overline{K} = K_0 + \dfrac{f(K_1 - K_0)(3K_0 + 4\mu_0)}{3K_1 + 4\mu_0} \quad \text{and} \\ \overline{\mu} = \mu_0 + \dfrac{5f\mu_0(\mu_1 - \mu_0)(3K_0 + 4\mu_0)}{3K_0(3\mu_0 + 2\mu_1) + 4\mu_0(2\mu_0 + 3\mu_1)}. \end{cases} \tag{2.4}$$

Here, f is the volume fraction of the TiB_2 phase, K_r and μ_r are the bulk and shear modulus, respectively for Al_2O_3 ($r = 0$) and TiB_2 ($r = 1$).

In Mori-Tanaka method,

$$\begin{cases} \overline{K} = K_0 + \dfrac{f(K_1 - K_0)(3K_0 + 4\mu_0)}{3K_0 + 4\mu_0 + 3(1-f)(K_1 - K_0)} \quad \text{and} \\ \overline{\mu} = \mu_0 + \dfrac{5f\mu_0(\mu_1 - \mu_0)(3K_0 + 4\mu_0)}{5\mu_0(3K_0 + 4\mu_0) + 6(1-f)(\mu_1 - \mu_0)(K_0 + 2\mu_0)}. \end{cases} \tag{2.5}$$

In self-consistent method,

$$\begin{cases} \bar{K} = K_0 + \dfrac{f(K_1 - K_0)(3\bar{K} + 4\bar{\mu})}{3K_1 + 4\bar{\mu}} \quad \text{and} \\ \bar{\mu} = \mu_0 + \dfrac{5f\bar{\mu}(\mu_1 - \mu_0)(3\bar{K} + 4\bar{\mu})}{3\bar{K}(3\bar{\mu} + 2\mu_1) + 4\bar{\mu}(2\bar{\mu} + 3\mu_1)}. \end{cases} \tag{2.6}$$

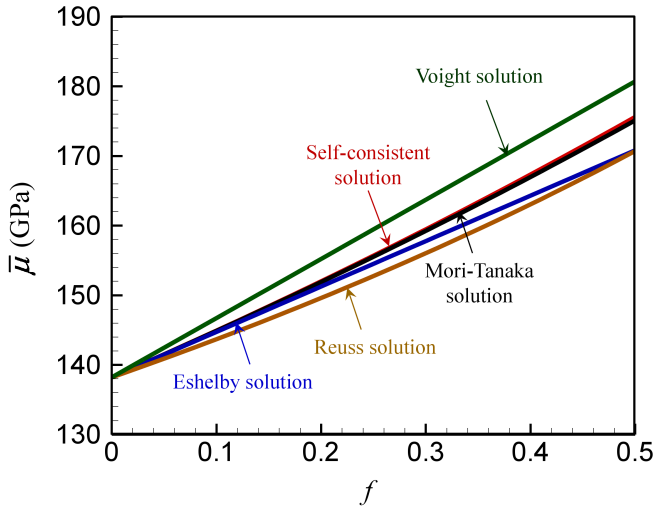

Fig. 2.3 Comparison of different homogenization methods.

Fig. 2.3 compares the solution of $\bar{\mu}$ using the above methods under different volume fraction f. The Voight solution and Reuss solution serve as the upper bound and lower bound, respectively. It is noted that the solutions in Eqn. (2.4), Eqn. (2.5) and Eqn. (2.6) are all within the bounds. Specifically, solutions using Mori-Tanaka method and self-consistent method are very close with each other. However, as indicated in Eqn. (2.6), $\bar{\mu}$ in self-consistent method is defined in an implicit manner. Its solution needs to be found numerically. Due to the uniqueness of the solution, selections has to be made judiciously if multiple roots are present. Therefore, Mori-Tanaka method provides a more efficient way for material property homogenization since $\bar{\mu}$ is defined explicitly. The Eshelby method works only for very dilute concentration ($f < 15\%$). When $f > 50\%$,

its solution will go beyond the lower bound and therefore does not make physical sense. In consideration of both accuracy and efficiency, the effective properties in the homogenized region are estimated using the Mori-Tanka method.

The effective Young's modulus $\bar{E}$ and Poisson's ratio $\bar{\nu}$ for the homogenized region are, respectively,

$$\begin{cases} \bar{E} = \dfrac{9\bar{K}\bar{\mu}}{3\bar{K}+\bar{\mu}} \quad \text{and} \\ \bar{\nu} = \dfrac{3\bar{K}-2\bar{\mu}}{6\bar{K}+2\bar{\mu}}. \end{cases} \tag{2.7}$$

The variations of $\bar{E}$ and $\bar{\nu}$ as functions of f are illustrated in Fig. 2.4.

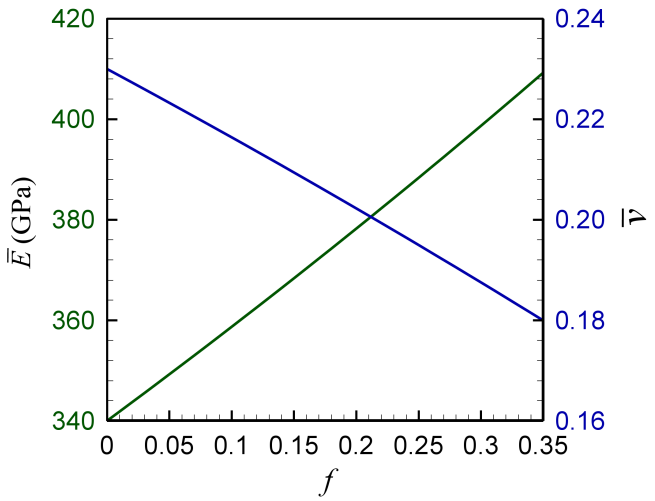

Fig. 2.4 Homogenized material properties at different TiB_2 volume fractions.

2.3.2 2D meshing scheme

The 2D finite element framework as described above requires refined meshes in the microstructure region so as to accurately delineate microstructure features and crack paths. The homogenized region, on the other hand, does not necessarily require the same mesh size. First of all, no fracture or specific detail is considered in the homogenized region. Its role is to capture the overall response of the whole structure as fracture develops in the microstructure. Besides, the computational time will be significantly increased if refined meshes are employed in both regions.

In consideration of accuracy and efficiency, uniform triangular elements with representative mesh size M_m and M_h are generated in the microstructure and the homogenized region, respectively. The mesh scheme is illustrated in Fig. 2.5. It is defined that $M_h = 2nM_m$ with n as an integer. A preferred range of n is from 3 to 5.

It is noted from Fig. 2.5 that the two regions with mesh size M_m and M_h are merged by the transitional meshes with geometrically similar equilateral triangles. The generation of transitional meshes starts from the microstructure region and continues to radiate to the homogenized region by following the recursive meshing algorithm as illustrated in Fig. 2.6.

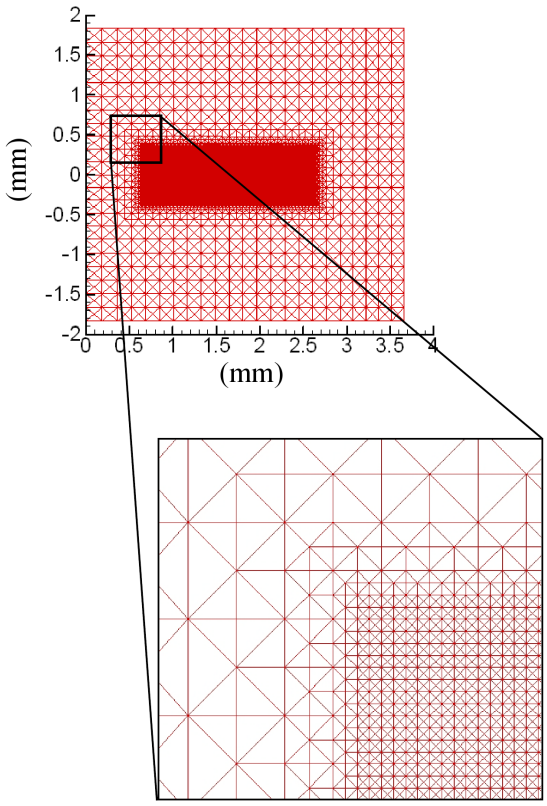

Fig. 2.5 2D structured meshes with varying densities across length scales.

The generation of transitional meshes follows 4 steps:

(1). Structured triangular meshes with side size M_m are generated in the microstructure region. The boundary nodes of the microstructure meshes are extracted and labeled with blue and purple dots with the pattern shown in Fig. 2.6(a).

(2). Each blue dot in Fig. 2.6(a) is considered as the center of a FCC cubic. The corner nodes of each cubic outside the microstructure mesh region are generated with pink dots as shown in Fig. 2.6(b). The new mesh boundaries

are formed by connecting the pink dots horizontally and vertically. Besides, the pink dots in each cubic are connected with the corresponding blue dot in the center. Each purple node is connected with the nearest pink node.

(3). A green dot is generated in the edge center of two pink dots as illustrated in Fig. 2.6(c). Each green dot is connected with the corresponding blue dot in the center.

(4). Each pink dot in Fig. 2.6(c) is considered as the center of a higher level FCC cubic. The generation of new corner nodes and connectivity exactly follow the procedures in step (2). The boundary nodes are labeled with blue and purple dots respectively as shown in Fig. 2.6(d). It is noted that the boundary node arrangement is identical with the node pattern in Fig. 2.6(a) with mesh size $M = 2M_m$. If $M = M_h$, uniform structured triangular meshes with size M_h will be generated in the rest of the homogenized region. If M has not reached the target size M_h, another loop of transitional mesh generation is activated by repeating step 2 to step 4.

The recursive meshing algorithm developed here is only valid for structured 2D triangular meshes with identical aspect ratios. The ratio between M_h and M_m has to be chosen carefully so that the transitional region does not exceed the homogenized region. The choice of M_m is discussed in Section 2.2. The range of M_h is defined so that the transitional region does not exceed 1/3 of the homogenized region. This algorithm cannot be applied to neither 3D or unstructured mesh configuration. Another modeling technique

to merge 3D unstructured and structured tetrahedral meshes will be discussed in Section 2.4.

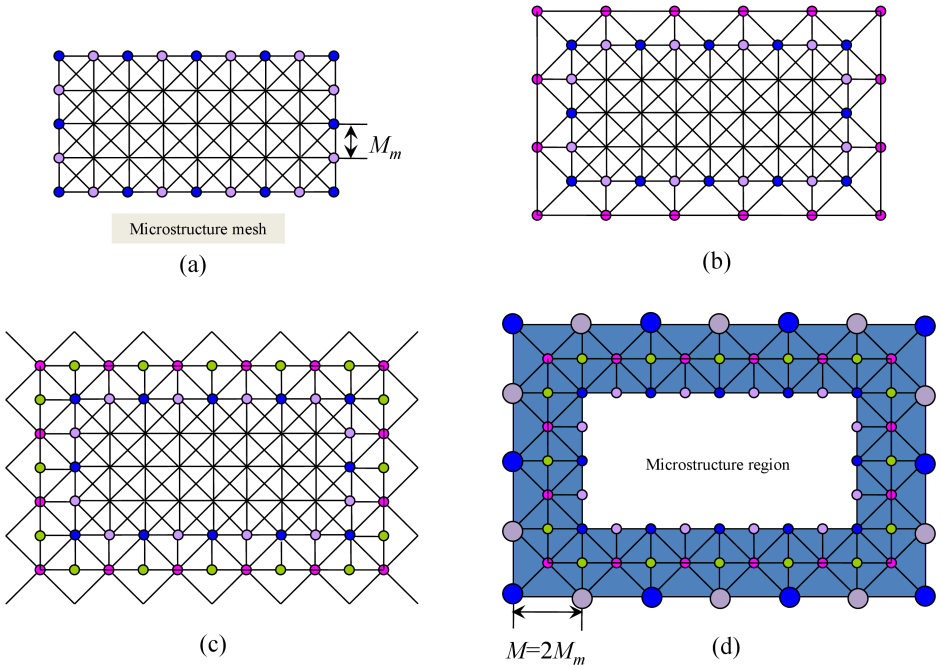

Fig. 2.6 Illustration of recursive meshing algorithm for transitional mesh generation.

2.3.3 Implementation of cohesive elements in 2D FEM

Insertion of cohesive elements in the finite element model requires node duplication and update of node connectivity in elements. A node map based algorithm is developed to efficiently embed cohesive elements in the structured triangular meshes as discussed in Section 2.3.2. As illustrated in Fig. 2.7, two types of nodes are considered in this mesh configuration. The corner nodes, which are labeled by upper case letters, have eight neighbor nodes. Therefore, seven additional nodes are duplicated from the original one. For example, node A is relabeled by A_1 with the seven duplicated nodes labeled from A_2 to A_8. Nodes A_1 to A_8 follow a counter clockwise order with A_1 locates at the top

of the horizontal edge. This pattern is followed by the entire corner nodes. Similarly, the center nodes, which are labeled by lower case letters, have four neighbor nodes. For example, node a is relabeled by a_1 with the three duplicated nodes labeled from a_2 to a_8. Nodes a_1 to a_4 follow a counter clockwise order with a_1 locates on the right. This pattern is followed by the entire center nodes.

The node map algorithm applies to all the nodes in the microstructure region. The node duplication is executed according to the node category. Afterwards, the duplicated nodes are redistributed to the corresponding element. For example, the element which is originally consisted of node A-B-b is updated to A1-B4-b4 as shown in Fig. 2.7. The 4-node 2D cohesive elements (COH2D4) with zero thickness are embedded along the edges of each bulk element by connecting the associated nodes in a counter clockwise order. For example, the cohesive elements embedded along the edge A-B, A-b and b-B are constructed as A_8-B_5-B_4-A_1, A_1-b_4-b_3-A_2 and b_4-B_4-B_3-b_1, respectively. The cohesive elements will permeate the entire microstructure region by following the above approach.

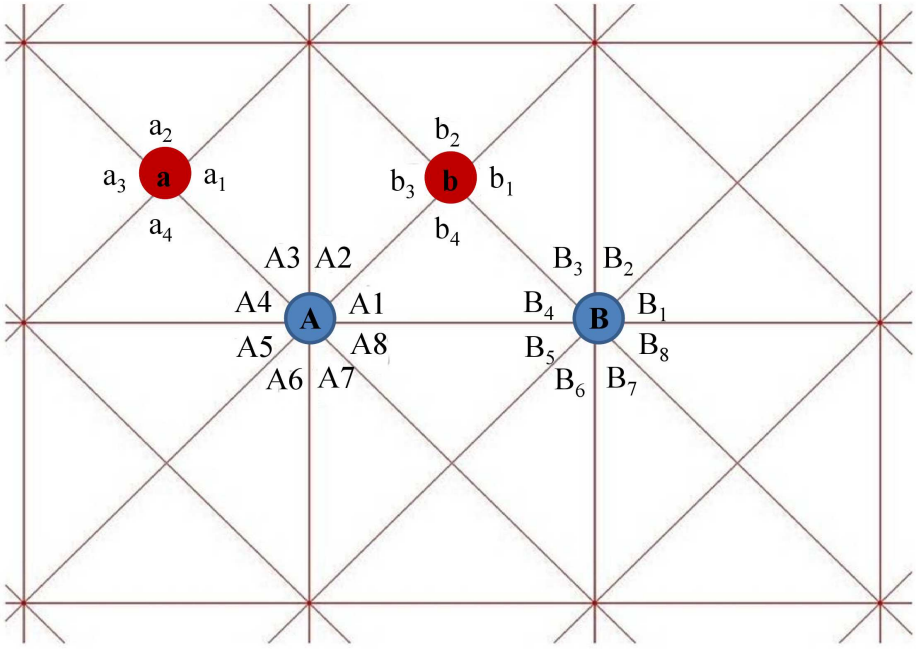

Fig. 2.7 Scheme of node map based algorithm for cohesive element insertion.

2.4 3D Model Structure

Fracture is inherently a 3D problem. 2D models, which simplify the problem by assuming plane strain conditions, cannot accurately capture the 3D morphology and orientation of grains, nor do they track crack-material interactions due to non-planar crack extension.

Over the past few years, the crystal plasticity based finite element method (CPFEM) has been widely used to analyze anisotropic deformation mechanisms in polycrystalline metals [39-41]. This method has also been coupled with the cohesive finite element method (CFEM) to address the material fracture behaviors [42-45]. Currently, most of these models only consider “virtual” idealized microstructures and intergranular fracture along the grain boundaries. None of them provides the capability to

explicitly capture both transgranular and intergranular fracture mechanisms and predict fracture toughness for realistic microstructures. The primary challenges lie in the geometrical complexity of 3D microstructures and difficulties to implement such information in finite element modeling. A 3D multiscale material design framework which includes 3D image based microstructure reconstruction, 3D meshing, and finite element implementation is developed. The 3D microstructures can be reconstructed from actual morphological features and crystallographic orientations, combining experimental investigations involving serial sectioning and electron backscatter diffraction (EBSD) with finite element modeling. For better delineation of grain boundaries and more realistic prediction of crack trajectory, unstructured tetrahedral meshes are employed by using the open source code iso2mesh [46]. Cohesive elements with traction-separation laws are embedded within grains and along the grain boundaries in order to respectively resolve transgranular and intergranular fracture modes. Crystal plasticity is incorporated into a User MATerial Subroutine (UMAT) for use in the commercially available FE software ABAQUS [47]. This modeling framework provides new insights into the physical aspects of competition between different fracture mechanisms and its correlation with the plastic deformation and crystallographic texture evolution.

2.4.1 3D configuration

The 3D framework is designed to study the fracture behavior of ductile polycrystalline materials. Calculations carried out concern Ti-6Al-4V alloy and focused on the two primary fracture mechanisms which are correlated with microstructure characteristics, constituent properties and deformation behaviors. An edge-cracked 3D

specimen under Mode I tensile loading is modeled as shown in Fig. 2.8. This proposed framework consists of two length scales. The microscopic subgrain scale with refined unstructured meshes has a size of $300\ \mu m \times 300\ \mu m \times 300\ \mu m$. 3D cohesive elements with 6-node zero thickness (COH3D6) fill the microstructure representation. Constitutive relations for the grains and separation laws for grain boundaries are specified separately. The cohesive relation allows damage and crack surface separation to be considered. Fracture emerges as a natural outcome of the deformation process based on these constitutive laws. Cohesive elements are embedded at the element surfaces both within the grains and along the grain boundaries to resolve transgranular and intergranular fracture. The macroscopic region with structured coarse meshes has a size of $900\,\mu m \times 900\,\mu m \times 300\,\mu m$. A boundary displacement $U = 10\,\mu m$ is imposed at the top and bottom surfaces to effect Mode I tensile loading. This region does not have any cohesive element and is employed to capture the overall material response at the structure level. We choose elastic parameters $C_{11} = 162{,}400$ MPa, $C_{12} = 92{,}000$ MPa, $C_{13} = 69{,}000$ MPa, $C_{33} = 180{,}700$ MPa, $C_{44} = C_{55} = 46{,}700$ MPa, $C_{66} = 35200$ MPa as reported by Mayeur [48]. The effective shear modulus $\bar{\mu}$ and bulk modulus $\bar{K}$ in the homogenized region are estimated following the self-consistent method as [49]

$$\begin{cases} \bar{\mu} = \dfrac{4\left(C_{11}-C_{13}\right)+2\left(C_{33}-C_{12}\right)+6\left(C_{66}+2C_{44}\right)}{60} + \\ \qquad \dfrac{15}{4}\left\{\dfrac{2\left(C_{11}+C_{12}\right)+C_{33}+4C_{13}}{\left(C_{11}+C_{12}\right)C_{33}-2C_{13}^2}+\dfrac{3}{C_{11}-C_{12}}+\dfrac{1.5}{C_{66}}+\dfrac{3}{C_{44}}\right\}^{-1} \quad \text{and} \\ \bar{K} = \dfrac{1}{18}\left(2C_{11}+C_{33}+2C_{12}+4C_{13}\right)+\dfrac{C_{33}\left(C_{11}+C_{12}\right)-2C_{13}^2}{2\left(C_{11}+C_{12}+2C_{33}-4C_{13}\right)}. \end{cases} \tag{2.8}$$

The effective Young's modulus $\bar{E} = 114.62$ GPa and Poisson's ratio $\bar{\nu} = 0.322$ are calculated according to

$$\begin{cases} \bar{E} = \dfrac{9\bar{K}\bar{\mu}}{3\bar{K} + \bar{\mu}} \text{ and} \\ \bar{\nu} = \dfrac{3\bar{K} - 2\bar{\mu}}{6\bar{K} + 2\bar{\mu}}. \end{cases} \tag{2.9}$$

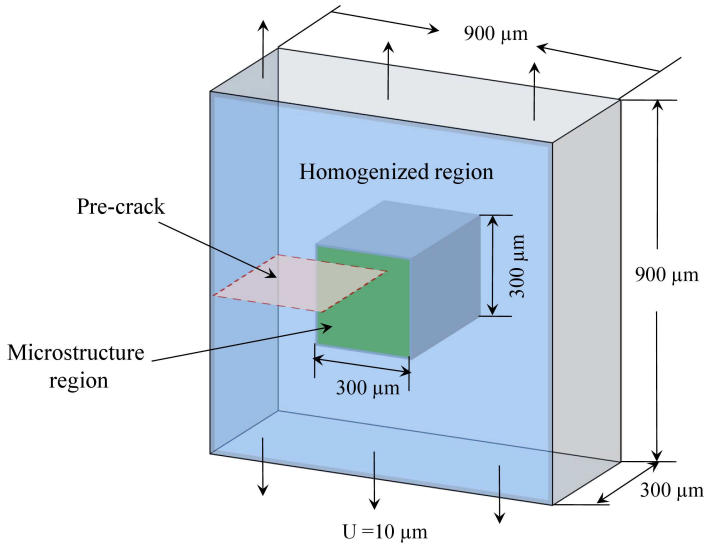

Fig. 2.8 3D specimen configuration used in the analysis.

2.4.2 Generation of mesh tie constraint

In order to obtain good delineation of grain boundaries and potential crack trajectories, unstructured tetrahedral meshes are generated in the microstructure region by iso2mesh [50]. Calculation of the *J*-integral in the homogenized region requires a closed contour connecting the upper and lower crack surfaces. It is very difficult to define contours if the homogenized region is meshed with unstructured elements as in the microstructure. One possible way to address this problem is to use structured tetrahedral

meshes in the homogenized region and generate a transitional region to connect the two types of meshes together. However, this method requires very sophisticated algorithms and may pose the challenge to change the size of the model when different mesh density is employed in the microstructure region. Apparently, the transitional region will increase as the discrepancy of mesh density between the two mesh regions increases. The size dependency of microstructure mesh density precludes the application of this method.

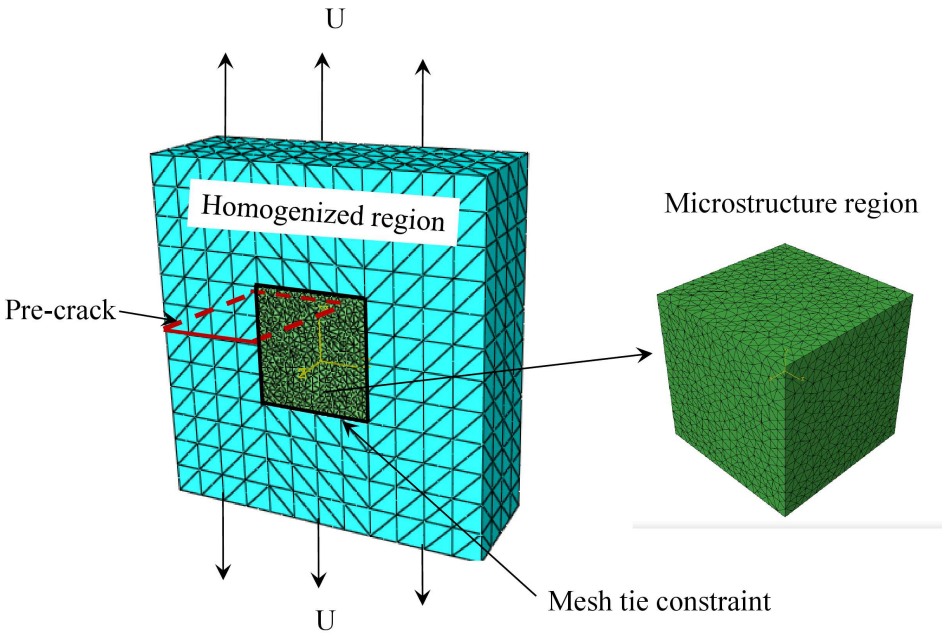

Fig. 2.9 Model assembly between the microstructure and homogenized region through mesh tie constraint.

In response to the modeling challenges, the mesh tie constraint is employed to assembly the two regions with different mesh types and densities as illustrated in Fig. 2.9. This constraint requires no conformity of nodal connectivity between the two regions. It circumvents the problem with acceptable accuracy. As illustrated for a 2D problem in Fig. 2.10, there is only a very minor difference between the *J* values for cases with and

without the mesh tie constraint. It should be noted that iso2mesh cannot generate perfect microstructure meshes with smooth exterior surfaces and sharp vertices as shown in Fig. 2.11. If the two regions cannot be seamlessly attached, the energy loss caused by the gap will significantly influence the accuracy of calculation. An innovative algorithm is developed to generate a shell mesh which is around the unsmoothed microstructure block to ensure proper node and element connectivity to the surrounding homogenized region. Now the two regions can be seamlessly assembled and be preceded to finite element analysis in ABAQUS [47].

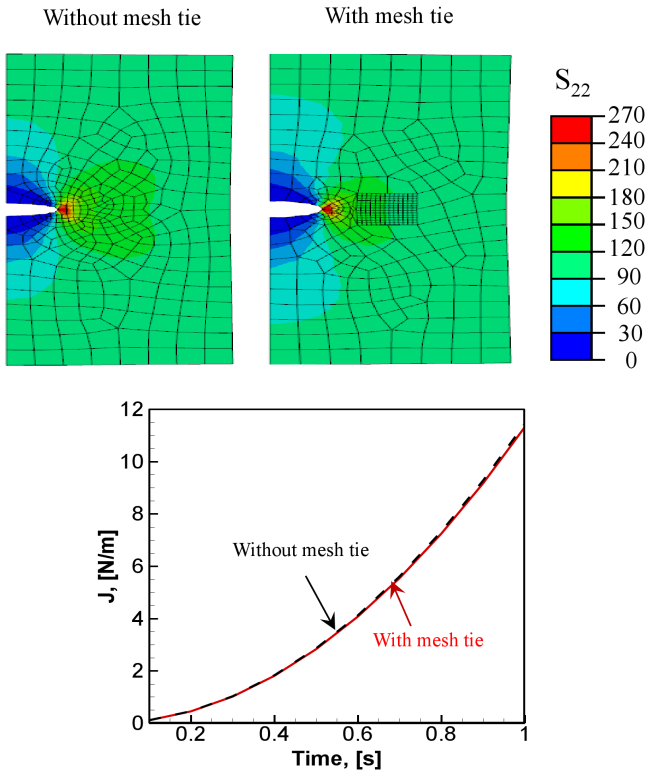

Fig. 2.10 Effect of mesh tie constraint on the calculated *J* values.

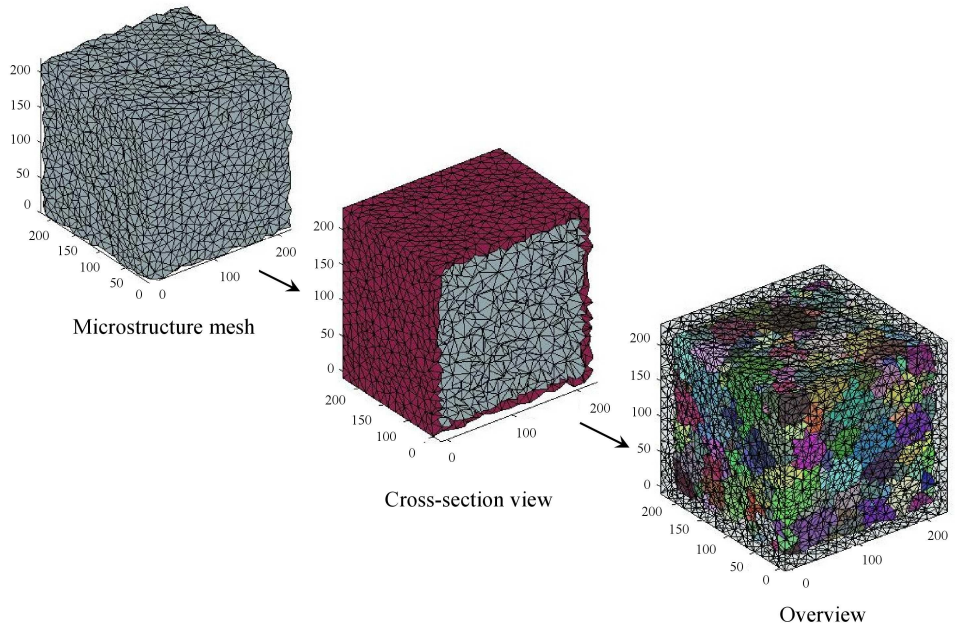

Fig. 2.11 Shell mesh region around the unsmoothed microstructure mesh.

2.4.3 Implementation of cohesive elements in 3D FEM

Specifying cohesive surfaces for complex 3D microstructure meshes is not a trivial task. The biggest challenge lies in how to effectively deal with the changes in the 3D nodal and elemental connectivities due to the introduction of cohesive surfaces. An algorithm has been developed to automatically insert 3D cohesive elements along grain boundaries and within individual grains, as illustrated in Fig. 2.12. The algorithm includes the following steps:

(1). Read the nodal coordinates and element arrangements of the microstructure meshes generated from iso2mesh.

(2). Separate the entire node and element information into grain and grain boundary sets, respectively.

(3). Define the location where cohesive elements will be inserted. The grain boundary is taken as an example.

(4). Sort out all the shared faces and the corresponding element indices within the grain boundary element set.

(5). Duplicate the nodes in the shared faces and redistribute the updated node label to the corresponding elements. As illustrated in Fig. 2.12, element 1 and element 2 shares the same face with node 2, 3 and 4. Assume N is the current total node number. Node N+1, N+2 and N+3 are cloned from node 2, 3 and 4, respectively. When distributing the duplicated nodes to elements (element 1 and element 2 in this case), it is crucial to make sure that the node labels in each element are only allowed to update once. For example, node 2 can be the member of another shared face in addition to face (2 3 4). Once node 2 in element 1 are replaced with node N+1, it is not allowed to be replaced by another duplicated node afterwards. This duplicated node can only be redistributed to the other element which shared the face.

(6). The cohesive element will be generated by connecting the 6 node label. As illustrated in Fig. 2.12, each cohesive element should follow the numbering pattern as [2 3 4 N+1 N+2 N+3].

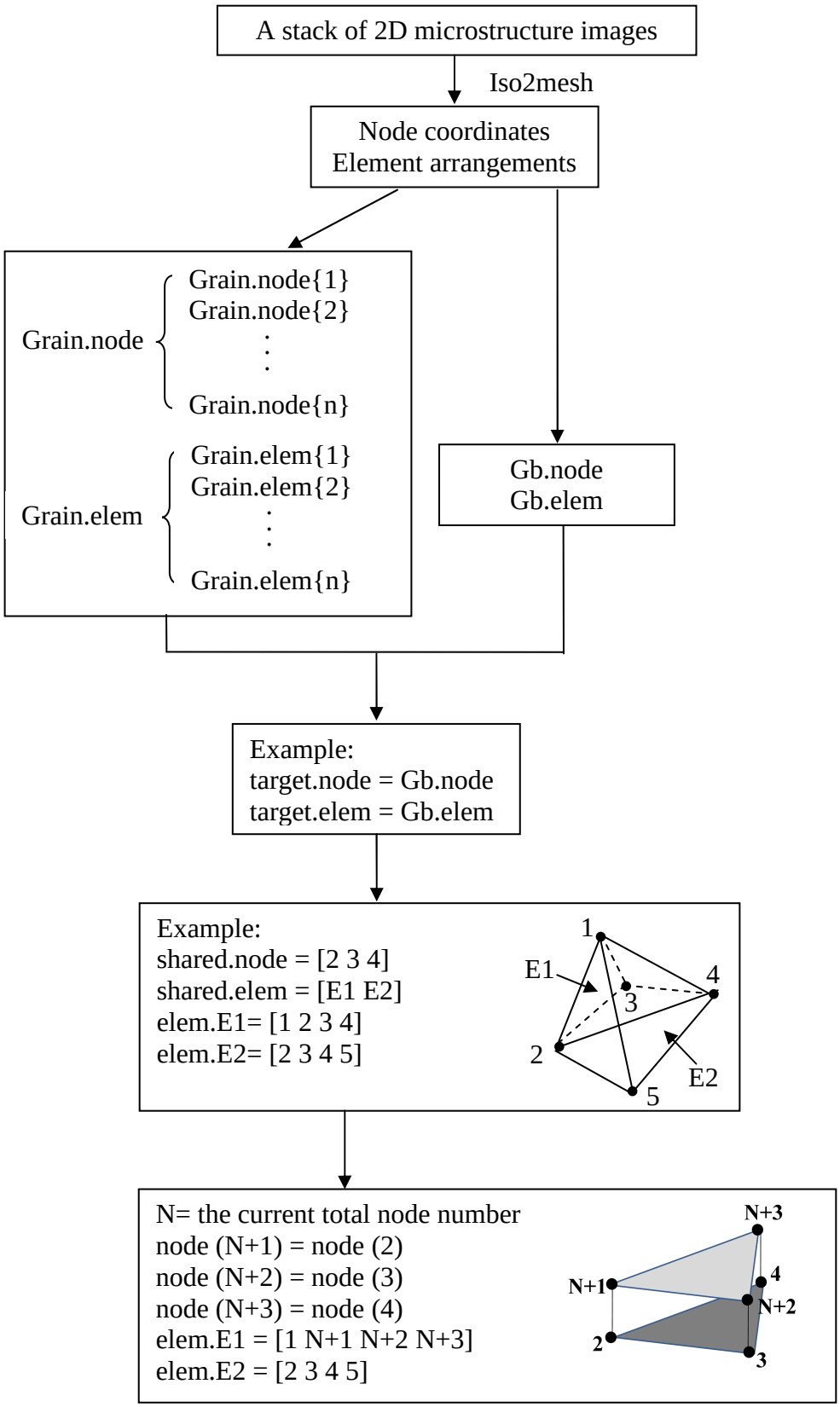

Fig. 2.12 Illustration of the algorithm for cohesive element insertion.

2.4.4 Insertion of pre-crack

It can be seen from Fig. 2.9 that the pre-crack locates both within the homogenized and microstructure region. The pre-crack plane introduced in the homogenized region is perpendicular to the applied displacement direction. However it is impossible to maintain the exactly identical pre-crack plane in the microstructure region since unstructured tetrahedral meshes are employed. To deal with this problem, a pre-crack path that consists of two layers of nodes is defined to extend the pre-crack to the microstructure as illustrated in Fig. 2.13. These nodes are selected according to their relative distances to the planer pre-crack. In our calculations, a tolerance of $\pm 5\,\mu m$ is considered. These nodes are duplicated and redistributed to elements that share the same surface patches. The node duplication and redistribution follow step (2) to step (4) as described in Section 2.4.3 and Fig. 2.12. The introduction of pre-crack facilitates crack initiation and propagation in the microstructure region.

2.4.5 Crystal plasticity formulation

Plastic deformation in metals is a manifestation of dislocation motion and interaction at the microscopic scale. The details are intimately related to the crystallographic structure of the material as well as the current state of the microstructure. Macroscopic models of plasticity lack the ability to link these fundamental mechanisms to the bulk material response without very substantial experimental characterization. Many formulations of constitutive laws for the elastic-plastic deformation of single and polycrystals have long been proposed [51-55]. The basic premise of these theories is that macroscopic plastic deformation is related to the cumulative process of slip system

shearing relative to the lattice. This methodology provides a physical link between the processes at different length scales. The two basic components of crystal plasticity model are the kinematic and kinetic relations.

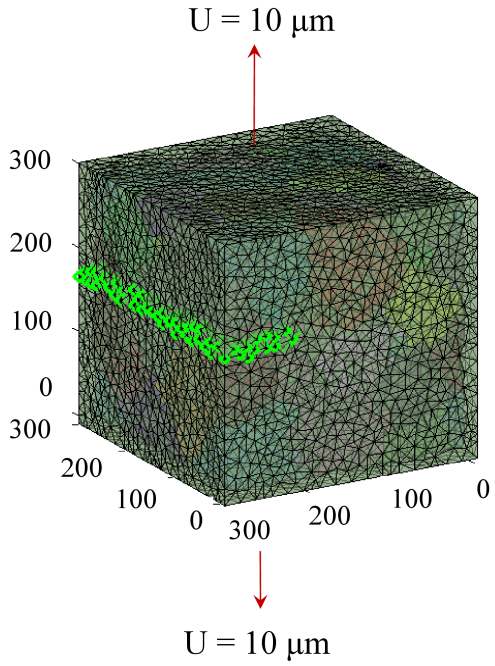

Fig. 2.13 Scheme of pre-crack location in the microstructure region.

The multiplicative decomposition of the total deformation gradient is given by

$$\mathbf{F} = \mathbf{F}^e \cdot \mathbf{F}^p, \tag{2.10}$$

where $\mathbf{F}^e$ is the elastic deformation gradient representing the elastic stretch and rotation of lattice, and $\mathbf{F}^p$ is the plastic deformation gradient describing the collective effects of dislocation motion along the active slip planes relative to a fixed lattice in the reference configuration. Unit vectors $\boldsymbol{s}_0^\alpha$ and $\boldsymbol{n}_0^\alpha$ denote the slip direction and the slip plane normal direction, respectively for the α^{th} slip system in the undeformed configuration. The

resolved shear stress on each slip system is related to the Cauchy stress tensor $\boldsymbol{\sigma}$ according to

$$\tau^{\alpha} = \boldsymbol{\sigma}:\left(\boldsymbol{s}^{\alpha} \otimes \boldsymbol{n}^{\alpha}\right), \tag{2.11}$$

where the slip vectors have been rotated into the current configuration. Under the application of the resolved shear stress, the shearing rates $\dot{\gamma}^{\alpha}$ on the slip systems are related to the plastic velocity gradient in the intermediate configuration according to

$$\mathbf{L}^{p} = \sum_{\alpha} \dot{\gamma}^{\alpha} \mathbf{s}_{0}^{\alpha} \otimes \mathbf{n}_{0}^{\alpha}, \tag{2.12}$$

with $\dot{\gamma}^{\alpha}$ ascribed to follow the rate-dependent flow rule as

$$\dot{\gamma}^{\alpha} = \dot{\gamma}_{0} \left\langle \frac{\tau^{\alpha} - \chi^{\alpha}}{g^{\alpha}} \right\rangle^{m} \operatorname{sgn}\left(\tau^{\alpha} - \chi^{\alpha}\right), \tag{2.13}$$

where m is the inverse strain rate sensitivity exponent and g^{α} and χ^{α} are drag stress and back stress, respectively on the α^{th} slip system. These quantities evolve according to

$$\begin{cases} \dot{g}^{\alpha} = H \sum_{\beta=1} q^{\alpha\beta} \left|\dot{\gamma}^{\beta}\right|, \text{ and} \\ \dot{\chi}^{\alpha} = A_{kin} \dot{\gamma}^{\alpha} - A_{dyn} \chi^{\alpha} \left|\dot{\gamma}^{\alpha}\right|. \end{cases} \tag{2.14}$$

Here $q^{\alpha\beta}$ is the latent hardening coefficient, H, A_{kin} and A_{dyn} are the isotropic hardening, kinematic hardening and dynamic recovery coefficients, respectively. These non-linear coupled differential equations are solved using UMAT [56].

2.5 *J*-integral Based Fracture Toughness Evaluation

In fracture mechanics, a number of representative approaches, such as the crack-tip opening displacement (CTOD), the crack-tip opening angle (CTOA) and *J*-integral, have been used to evaluate the material fracture toughness. Numerically, *J*-integral stands out as a more robust and practical measurement of the crack driving force. First of all, *J*-integral allows characterization of the crack tip area without directly focusing on the crack tip, although its value depends on the near tip stress and strain. The path-independent nature of *J*-integral allows an integration path to be sufficiently far from the crack tip. Besides, it can be applied to both elastic and elastic-plastic materials. Compared with the numerical determination of CTOD, the calculation of *J*-integral requires minimum mesh refinement and evaluation time [57, 58].

For brittle materials, crack propagation can be dynamic even under quasistatic loading [59, 60]. To account for inertia effects, a fully dynamic deformation formulation is used. Within this framework, the path-independent *J*-integral is [61-63]

$$J = \int_{\Gamma}\left[\left(\int_0^t \boldsymbol{\sigma} : \mathrm{d}\boldsymbol{\varepsilon} + \frac{1}{2}\rho\dot{\mathbf{u}}\cdot\dot{\mathbf{u}}\right)\mathrm{d}x_2 - \boldsymbol{t}\cdot\frac{\partial \mathbf{u}}{\partial x_1}\mathrm{d}s\right] + \int_A\left(\rho\ddot{\mathbf{u}}\cdot\frac{\partial \mathbf{u}}{\partial x_1} - \rho\dot{\mathbf{u}}\cdot\frac{\partial \dot{\mathbf{u}}}{\partial x_1}\right)\mathrm{d}A, \quad (2.15)$$

where $\boldsymbol{t}$ is the traction on a surface with normal **N**, **u** is the displacement, $\boldsymbol{\varepsilon}$ denotes the strain and ρ is the mass density.

In the 2D model, the TiB_2 and Al_2O_3 phases are assumed to be isotropic and linear elastic. For this type of material, the longitudinal, shear and Rayleigh wave speeds are [64]

$$C_l = \sqrt{\frac{\bar{E}(1-\bar{\nu})}{\bar{\rho}(1+\bar{\nu})(1-2\bar{\nu})}}, \quad C_s = \sqrt{\frac{\bar{E}}{2\bar{\rho}(1+\bar{\nu})}}, \quad C_r = C_s \frac{0.862+1.14\bar{\nu}}{1+\bar{\nu}}. \quad (2.16)$$

Here, $\bar{\rho} = 4200\,kg/m^3$ is taken as the homogenized material density. $\bar{E}$ and $\bar{\nu}$ are calculated according to Eqn. (2.7). Therefore, the longitudinal, shear and Rayleigh wave speeds are in the range of [9688, 10286] m/s, [5737, 6426] m/s and [5243, 5812] m/s, respectively. The *J*-integral is equivalent to the energy release rate *G* and can be related to the stress intensity factor *K* via [65]

$$K^2 = \frac{J}{A(\mathrm{V})}\frac{E}{1-\nu^2}, \quad (2.17)$$

where V is the crack speed and $\mathrm{A}(V) = \dfrac{V^2\beta_1}{(1-\nu)C_s^2 D}$ with $\beta_1 = \sqrt{1-(V/C_l)^2}$, $\beta_2 = \sqrt{1-(V/C_s)^2}$ and $D = 4\beta_1\beta_2 - \left(1+\beta_2^2\right)^2$. Note that as $V \to 0$, $\mathrm{A}(V) \to 1$.

For the model shown in Fig. 2.2, contours for *J* evaluation are solely within the homogenized part of the specimen where no cohesive elements are used. Due to the path-independent property of *J*-integral, the results extracted from different contours are very close to each other. In all the following calculations, the average value of *J* from four different contours will be used to best eliminate numerical error.

For steady state crack growth, the driving force represented by J balances out the fracture resistance, allowing the fracture resistance to be evaluated through Eqn. (2.17). To calculate J and in turn K, boundary velocities between 5×10^{-4} mm/s to 15 mm/s are applied. The results for a microstructure with circular reinforcement particles are

shown in Fig. 2.14. Fig. 2.14(a) shows $J/\mathrm{A}(V)$ as a function of crack length and Fig. 2.14(b) illustrates the corresponding histories of crack speed. Reflecting the wide range of boundary loading velocities, the crack speeds for the different cases span from approximately 28 m/s for $\mathrm{v} = 5\times10^{-4}$ mm/s, 392 m/s for $\mathrm{v} = 5\times10^{-3}$ mm/s, 1295 m/s for $\mathrm{v} = 5\times10^{-2}$ mm/s to approximately 3600 m/s for $\mathrm{v} > 0.5$ mm/s. The highest value is approximately 60% of the Rayleigh wave speed of the composite. Upon the arrival of the loading wave at the crack tip region, the $J/\mathrm{A}(V)$ starts to increase rapidly. When the value reaches point A, the crack begins to propagate slowly and steadily (crack speed below 25 m/s). At point B, both $J/\mathrm{A}(V)$ and the crack speed increase rapidly and quickly reach point C. Beyond point C, the crack speed oscillates around an average value as the crack encounters and passes reinforcement particles. Although the instantaneous crack speed is not steady over short distances, the average crack speed is quite steady over longer distances between points C and D. Also, at the lower crack speeds, the magnitudes of the oscillations in both the crack speed and $J/\mathrm{A}(V)$ are lower. At the lowest speed of approximately 28 m/s, the oscillation is the lowest and the propagation of the crack can be approximately regarded as quasistatic. The time it takes for stress waves to traverse the distance between the crack tip and the boundary of the specimen is approximately $0.2\,\mu\mathrm{s}$. In contrast, time interval for crack propagation is approximately $149.6\,\mu\mathrm{s}$. This specimen design allows the calculations to approximate conditions of quasi-static loading. It is important to note that $J/\mathrm{A}(V)$ for all the cases essentially coincide, even though the crack speed spans three orders of magnitude. This is expected as the brittle ceramic system considered here is rate-independent. This observation suggests that the fracture toughness values obtained may be regarded as both

quasistatic and dynamic, within the fully elastic material constitutive framework considered here. Since all loading velocities give consistent results, unless otherwise noted most calculations are carried out with $v = 5$ mm/s for computational efficiency.

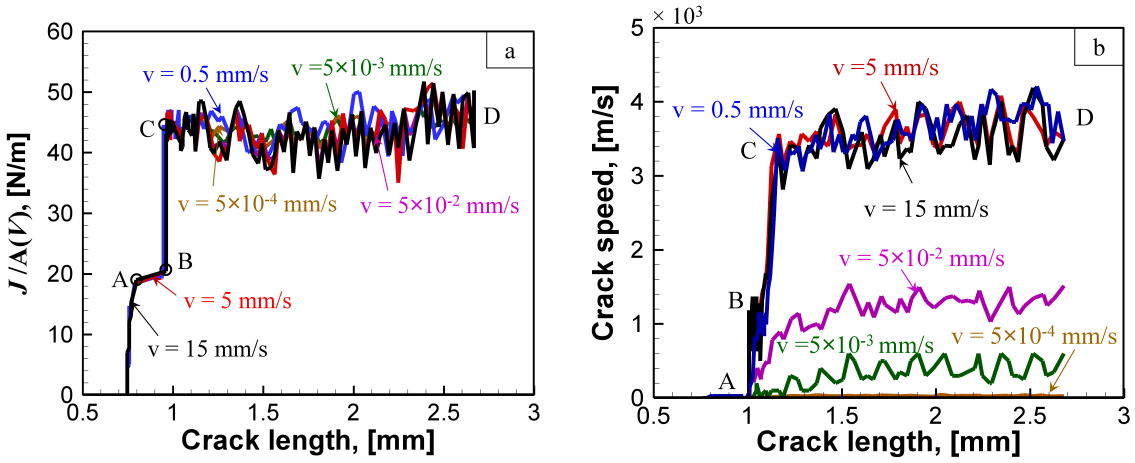

Fig. 2.14 (a) Comparison of J/A(V) under different loading rates, (b) Comparison of crack speed under different loading rates .

The fracture toughness of composites may not be sufficiently captured by a single parameter, as argued by Manoharan and Kamat [66]. The issue is even more pronounced for processes of crack initiation and propagation. Here, we measure both the initiation toughness K_{IC}^{i} and the propagation toughness K_{IC} from the evolution of J. The initiation toughness is measured at the critical point where the crack begins to propagate [point A, Fig. 2.14(a)]. The propagation toughness is obtained from the average J value over the distance the crack traverses a sufficiently representative part of the microstructure, between points C and D in Fig. 2.14(a).

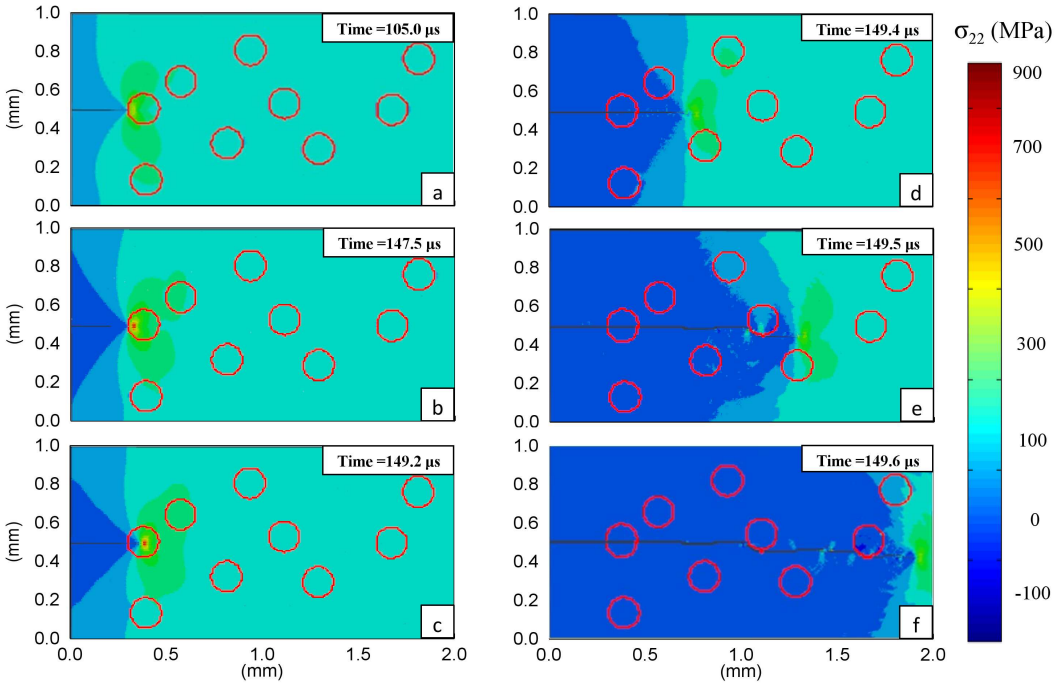

Fig. 2.15 Crack propagation in a microstructure with circular reinforcement.

To illustrate the fracture process studied, Fig. 2.15 shows six snap shots of the crack propagation process in a microstructure with circular TiB_2 reinforcement at a loading velocity of $v = 5$ mm/s . The corresponding histories of *J* and *K* are shown in

Fig. 2.16. Fracture initiates in the Al_2O_3 matrix at 105.0 μs [Fig. 2.15(a)], this event defines the initiation toughness K_{IC}^{i}. The crack is arrested by a TiB_2 particle and pauses at the Al_2O_3/TiB_2 interface for approximately 42.5 μs [Fig. 2.15(b)]. During the pause, *J* increases rapidly. At approximately 149.2 μs [Fig. 2.15(c)], as a result of the higher level of driving force *J*, the crack penetrates the TiB_2 particle. Subsequently, the crack propagates rapidly, causing *J* (and therefore *K*) to plateau for the remainder of the analysis. The average value of *K* during this period is taken as the propagation toughness K_{IC} .

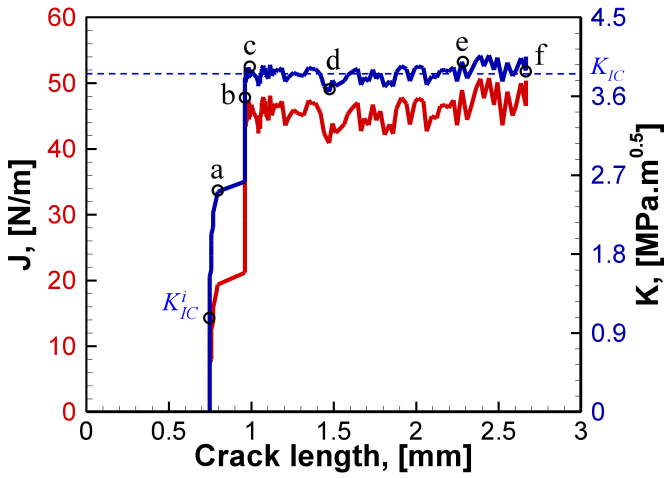

Fig. 2.16 Evolution of *J* and *K* during the crack propagation process in Fig. 2.15.

2.6 Summary

A cohesive finite element method (CFEM) based multiscale computational framework is developed for predicting fracture toughness of materials as function of microstructure. This framework provides a means for evaluating fracture toughness through explicit simulation of fracture processes in microstructures. The approach uses the *J*-integral, allowing fracture toughness to be calculated for microstructures with random heterogeneous phase distributions and fracture processes with arbitrary crack paths or micro-crack patterns. Both 2D and 3D frameworks are developed. Although this dissertation focuses on specific materials, the methodology developed can be applied to any material system in principle.

3 MICROSTRUCTURE CHARACTERIZATION AND GENERATION

3.1 Introduction

Microstructural attributes such as reinforcement/grain size, reinforcement volume fraction, reinforcement morphology, and distributions of the phases significantly influence the material behavior and are, therefore, of primary consideration in material design. To characterize the microstructures analyzed, the two-point correlation functions [67] are used. These functions allow attributes of microstructures such as the second-phase reinforcement size, volume fraction and spatial distribution to be readily extracted. The quantification is used to generate microstructural samples with independently varying characteristics so that the effect of each attribute on fracture toughness can be evaluated [68]. In addition, the two-point correlation functions provide a means to statistically parameterize the probability of crack interactions with these heterogeneities. This quantification lends itself to the establishment of relations between the statistical attributes of microstructure, fracture mechanism and the fracture toughness of the material. In addition to the two-point correlations functions which primarily characterize the distribution of phases and may be insensitive to the morphology of phases in a microstructure, our studies also reveal that additional descriptors or parameters quantifying the morphology of phases are needed to sufficiently quantify and distinguish between different microstructures with varying reinforcement sizes and shapes. The influence of such a parameter (i.e., the roundness of reinforcement particles) on the fracture toughness is also discussed.

The 2D microstructure sets are generated based on the two-point correlation functions and the proposed geometric descriptors. For 3D microstructures, an image based microstructure reconstruction approach is developed. This approach allows explicit control of geometric attributes of the microstructure, such as the volume fraction of each phase, average grain size as well as the grain size distribution. It also opens up the possibility to reconstruct 3D realistic microstructures from actual morphological features and crystallographic orientations, combining experimental investigations involving serial sectioning and electron backscatter diffraction (EBSD) with finite element modeling.

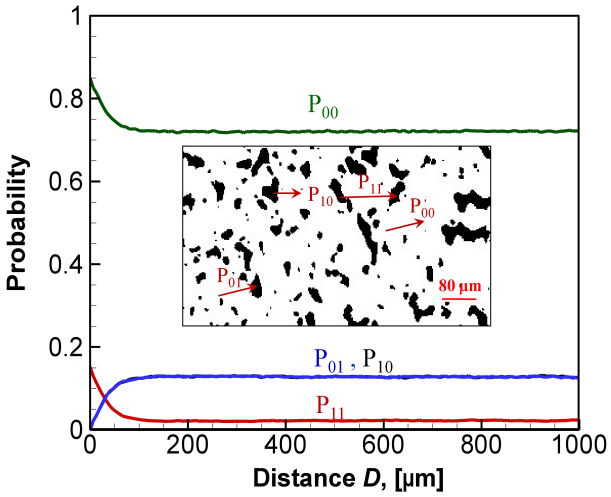

Fig. 3.1 Two-point correlation function for a two-phase microstructure.

3.2 Two-Point Correlation Functions

Two point correlation functions are widely used in materials science to characterize microstructures [68, 69]. The functions measure the probability of finding a given combination of phases over given distances. Specifically, in 2D microstructures with two phases such as the one shown in Fig. 3.1, the function P_{ij} denotes the

probability for randomly placed vectors of a given length to start in phase i ($i = 0$ or 1) and ends in phase j (0 or 1). It is noticed that only three of the four two-point correlation functions are independent since $P_{00} + P_{01} + P_{10} + P_{11} = 1$. Here, the matrix is defined as phase 0, and the reinforcement is defined as phase 1. f denotes the volume fraction of the reinforcement phase.

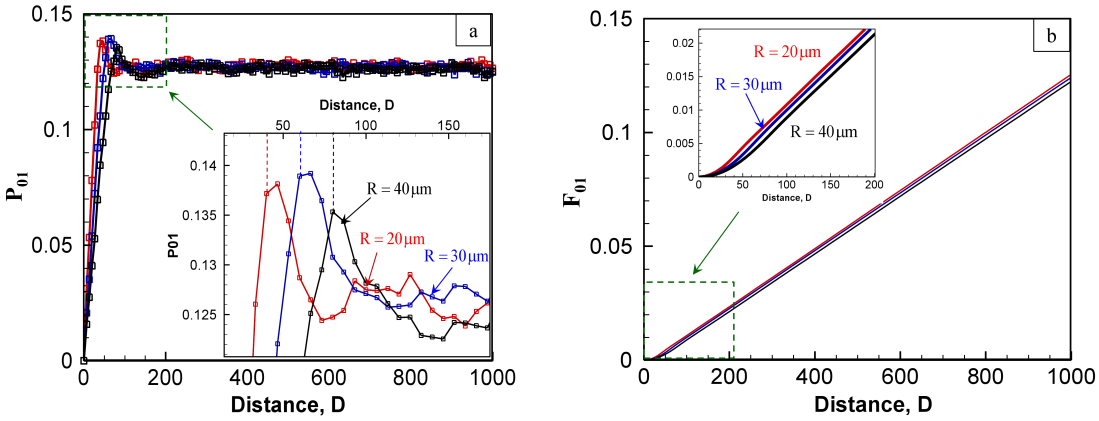

Fig. 3.2 (a) Interpretation of P_{01} and, (b) F_{01}.

Fig. 3.2(a) shows the two-point correlation representation (P_{01}) of a set of microstructures with randomly distributed uniform circular particles. The peak of each curve occurs at a distance equal to the particle diameter as shown in the inset. The two-point correlation functions can be quantified by the following functions

$$\begin{cases} P_{11} = \left(f - f^2\right)e^{-(D/s)} + f^2, \\ P_{00} = \left[\left(1-f\right) - \left(1-f\right)^2\right]e^{-(D/s)} + (1-f)^2, \text{ and} \\ P_{01} = P_{10} = \left(1 - P_{11} - P_{00}\right)/2. \end{cases} \tag{3.1}$$

Here, s is a parameter representing the characteristic size of the reinforcement. For microstructures with randomly distributed circular particles of the same diameter, s is equal to the diameter. P_{01} can be regarded as the geometric probability of encountering the reinforcement phase by a crack of a certain length that is propagating in the matrix. The area underneath the P_{01} curve, which is denoted as F_{01} in Fig. 3.2(b), can be taken as a measure for the cumulative interactions with the reinforcement phase by a straight crack over its course of propagation. Obviously, F_{01} becomes linear beyond a certain distance (D_{cha}) at which P_{01} reaches its long-distance limit of $\left[1-f^2-(1-f)^2\right]/2$. This distance ($D_{cha}$) is taken as a characteristic length for the microstructure. For crack lengths below D_{cha}, the probabilistic interactions of a crack with the reinforcement phase sensitively depends on not only the volume fraction of the reinforcement, but also the phase morphology and phase size scale. Beyond D_{cha}, the long-term geometric probability of a straight crack encountering the reinforcement phase depends only on the volume fraction of the reinforcement (since the values of P_{ij} beyond D_{cha} depends only on f), not phase morphology or size scale. Naturally, to sufficiently capture the fracture behavior of different macrostructures, crack propagations over distances longer than the characteristic lengths of the microstructures must be considered. In the analyses carried out here, the characteristics lengths of the microstructures are less than 100 μm and the total distances of crack propagation are 1.5-2 mm. To compare the propagation toughness of different microstructures, the F_{01} values at the same crack propagation distance of 800 μm are used.

3.3 Shape Descriptor

Although two-point correlations functions successfully characterize the distribution of phases, it is insensitive to the morphology of phases in a microstructure. Therefore, additional descriptors or parameters quantifying the morphology of phases are needed to sufficiently quantify and distinguish between different microstructures with varying reinforcement shapes.

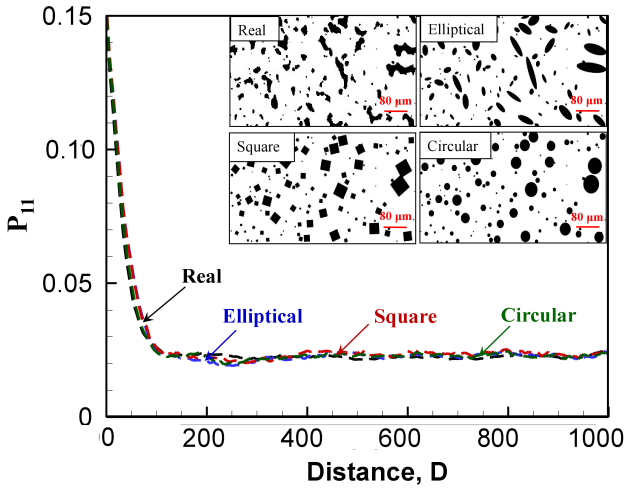

Fig. 3.3 Similarity between the two point correlation functions of microstructures with different reinforcement particle shapes.

A case in point is shown in Fig. 3.3. The microstructures with elliptical, square and circular shaped reinforcement particles are generated from the real microstructure as listed. All four microstructures have the same reinforcement volume fraction (15%), reinforcement orientation and size distribution. The nearly identical two-point correlation curves point to the need to quantify the effect of phase morphology or particle shape for particle-reinforced composites. Indeed, as we will discuss later, while the two-point correlation function measures the geometric probability for a crack to encounter the

reinforcement, the shape parameter measures how the crack interacts with the reinforcement particles. Naturally, both aspects are important. The mean reinforcement roundness $\bar{\rho}$ of a microstructure is defined as

$$\bar{\rho} = \frac{1}{n}\sum_{i=1}^{n}\rho^i = \frac{1}{n}\sum_{i=1}^{n}\frac{4A^i}{\pi\left(d^i_{\max}\right)^2} \tag{3.2}$$

to quantify the circularity and surface irregularities of reinforcements in a microstructure [70-72]. Here, A^i, $d^i_{\max}$ and ρ^i are the area, maximum distance and roundness of the *i*th reinforcement particle, respectively. *n* is the total number of particles.

3.4 2D Microstructure Generation

Microstructural sample set 1, as listed in Fig. 3.4, is generated based on the two point correlations functions. Note that this set has systematically varying particle radius ($R = s/2 = 20\,\mu m$, $30\,\mu m$ and $40\,\mu m$) and volume fraction ($f = 10\%, 15\%, 20\%, 25\%$ and 30%). For each combination of particle size and volume fraction, 20 randomly generated microstructural instantiations are used to obtain a statistical characterization of the stochastic nature of the failure processes at the microstructure level. The correlations between the two-point correlation parameter F_{01} and fracture toughness will be studied in detail in Section 4.2.

Microstructural sample set 2, as listed in Fig. 3.5, is generated based on the shape descriptor. The microstructures with elliptical, square and circular shaped reinforcement particles are generated from the real microstructure. In each group, all the four microstructures have the same reinforcement volume fraction (15%), reinforcement

orientation and size distribution. The only variation considered is the reinforcement shape. FigureFig. 3.6 compares the distributions of the particle roundness values of the four microstructures.

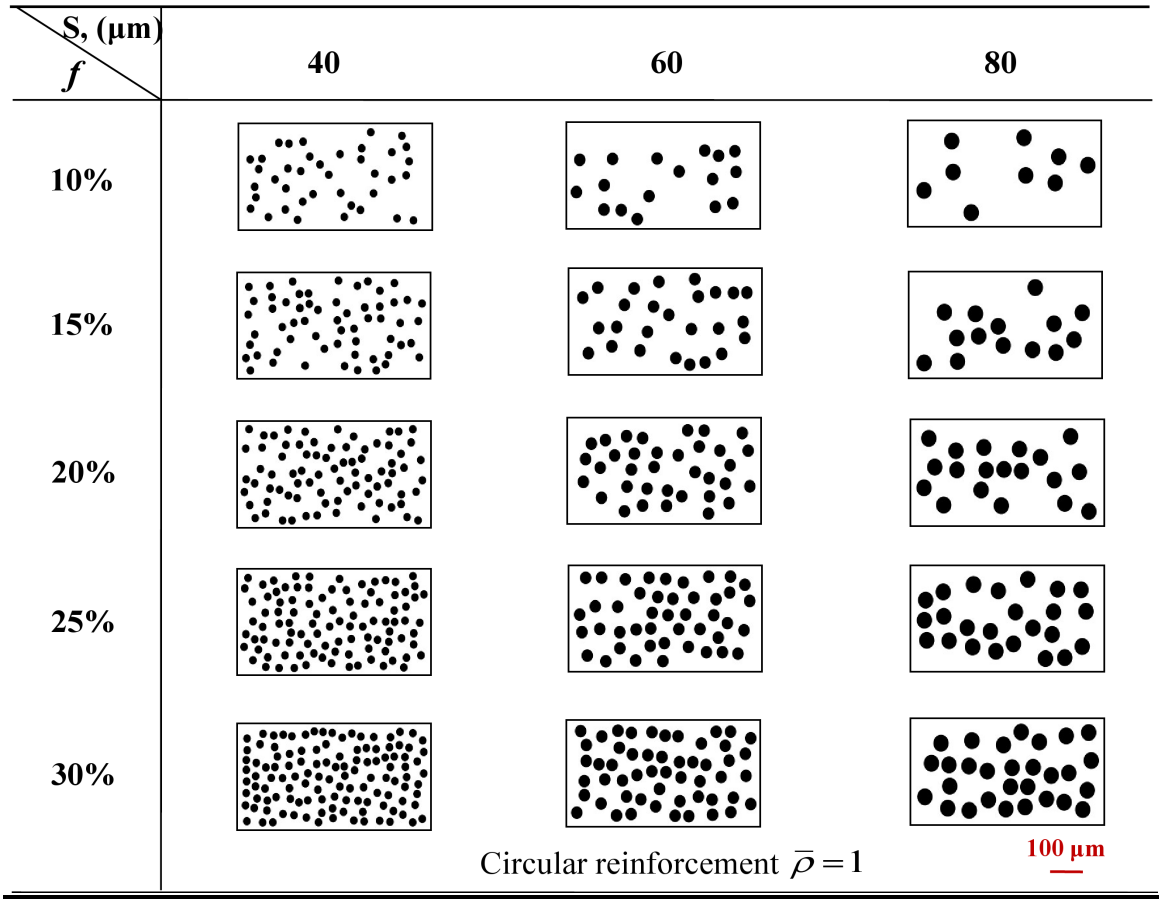

* f is the reinforcement volume fraction. s and $\bar{\rho}$ are characteristic reinforcement size and roundness, respectively, as defined in Section 3.2.

Fig. 3.4 Design space of microstructures with randomly distributed, non-overlapping circular reinforcements. Twenty random instantiations (samples) of each microstructure are used in the calculations to obtain a statistical characterization of the result for each case.

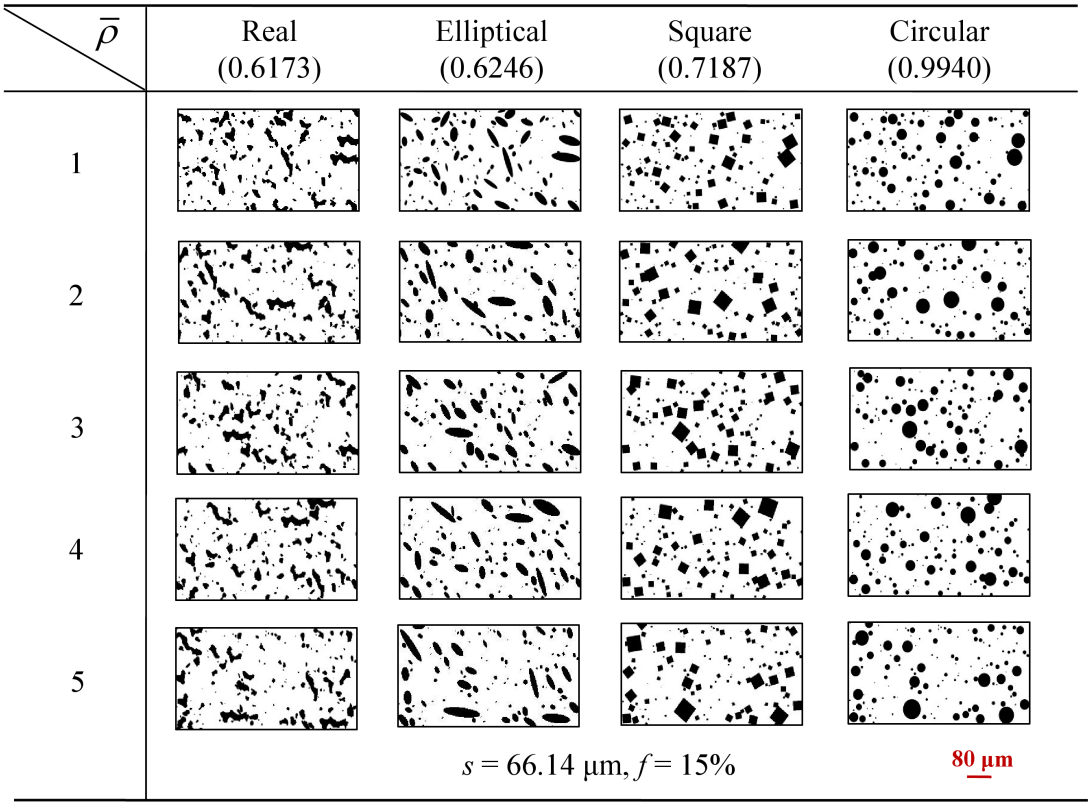

* f is the reinforcement volume fraction. s and $\bar{\rho}$ are characteristic reinforcement size and roundness, respectively, as defined in Section 3.3.

Fig. 3.5 Design space of microstructures with various reinforcement shapes. Twenty random instantiations (samples) of each microstructure are used in the calculations to obtain a statistical characterization of the result for each case.

3.5 3D Microstructure Reconstruction

Voronoi tessellation is a popular technique for generating polycrystalline microstructures due to its simplicity, space-filling nature and the availability of theoretical results for the topological properties [73, 74]. However, microstructures generated in this way are not always consistent with experimental results [75]. To

realistically capture the topological and statistical properties of microstructures, a method for instantiate 3D polycrystalline microstructures is employed.

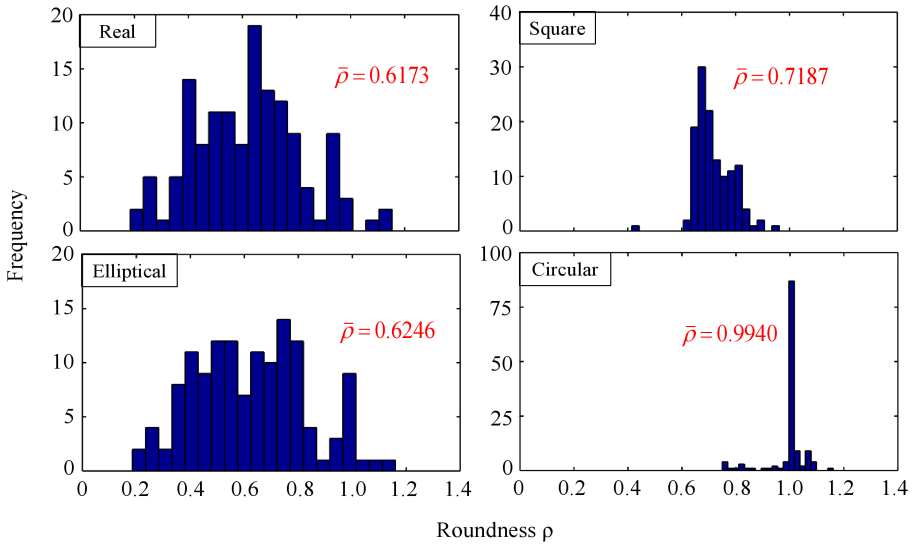

Fig. 3.6 Comparison of the roundness distributions for microstructures with different reinforcement shapes.

A set of ellipsoidal grains are generated based on predefined distributions of the ratios of the major ellipsoidal axis. These ellipsoids are placed into the space until no more non-overlapping ellipsoids can be placed. The random packing and placement of these ellipsoids follows the algorithm developed by Przybyla [76] and Tschopp [77]. Once every ellipsoidal grain has been randomly placed and oriented, the open space in between is filled by the process of grain growth. The grain growth algorithm starts with one grain and sequences through the rest of the grains, increasing their size in each direction by one pixel at a time. This process repeats itself until every grain reaches its nearest neighbor. After this point, the voxels on either side of the grain boundary no longer evolve in subsequent steps. Once all the free spaces are filled, the 3D

microstructure is fully instantiated and its morphological information is stored in a 3D matrix. The exported 2D images are essentially from the generated 3D microstructure. The 2D image series is employed as input for visualization and meshing as required by the open source code iso2mesh [50]. A 2D rendering of ellipsoidal grain packing and the grain structure morphology after grain growth are illustrated in Fig. 3.7.

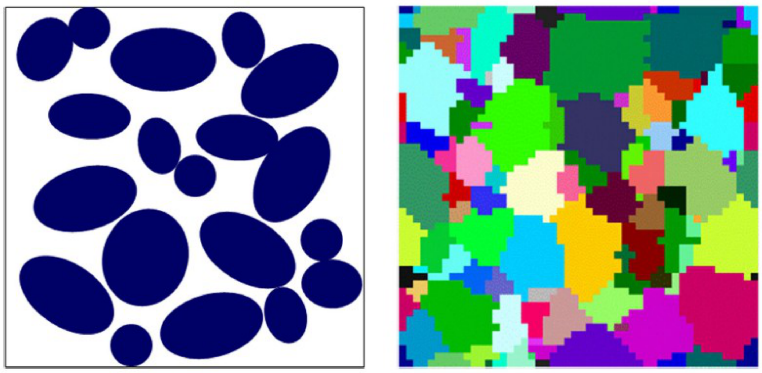

(a) (b)

Fig. 3.7 (a) 2D rendering of ellipsoidal packing algorithm upon initial placement of ellipsoids and (b) 2D rendering of grain structure based on ellipsoidal packing after grain growth.

Using grain equivalent ellipsoids instead of other space filling methods like Voronoi tessellation allows construction of more complex grain morphologies such as elongated grains that are common in rolled ductile metals [78]. A Ti-6Al-4V microstructure with bi-modal grain size distribution is generated using this method with a bi-modal grain size distribution. The grain size is determined by first calculating the new ellipsoid volumes to account for grain growth. The actual grain size cumulative distribution function (CDF) and target CDF for each phase are plotted in Fig. 3.8. This cumulative distribution function can be used to assess how well the final size distribution

fits to a log normal distribution function. This algorithm allows explicit control of geometric attributes of the microstructure, such as the volume fraction of each phase, average grain size as well as the grain size distribution. This algorithm allows explicit control of geometric attributes of the microstructure, such as the volume fraction of each phase, average grain size as well as the grain size distribution.

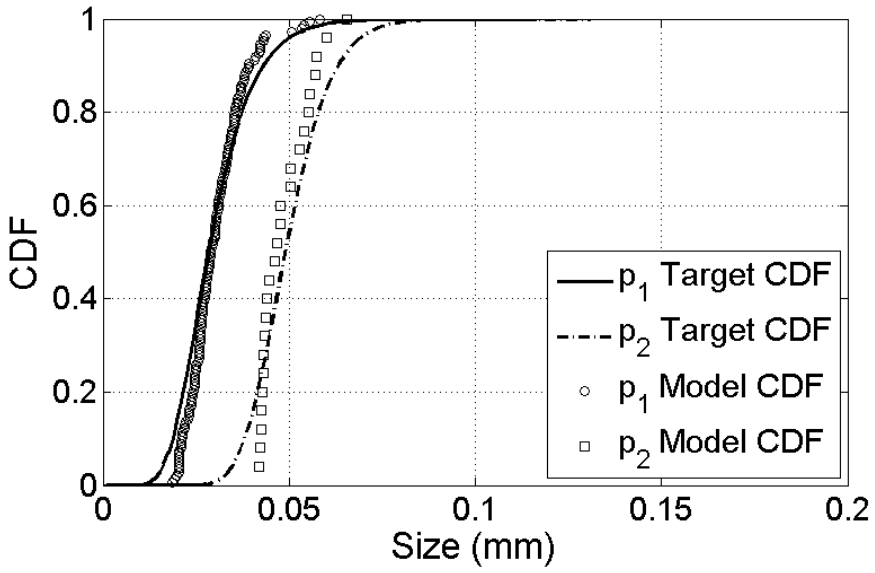

Fig. 3.8 Target log-normal and fit model distributions of the grain size for the primary α grains (p_1) and the α+β grains (p_2).

A series of 2D microstructure images generated from the above ellipsoidal packing algorithm are employed as the input for 3D microstructure visualization and meshing. These 2D image series can be experimental data such as serial sectioning with EBSD mapping. In order to obtain good delineation of grain boundaries and potential crack trajectories, unstructured tetrahedral meshes are generated by iso2mesh [50] as illustrated in Fig. 3.9. The output data, including the node coordinates for the generated

volumetric mesh and the tetrahedral element information, are used for the finite element implementation.

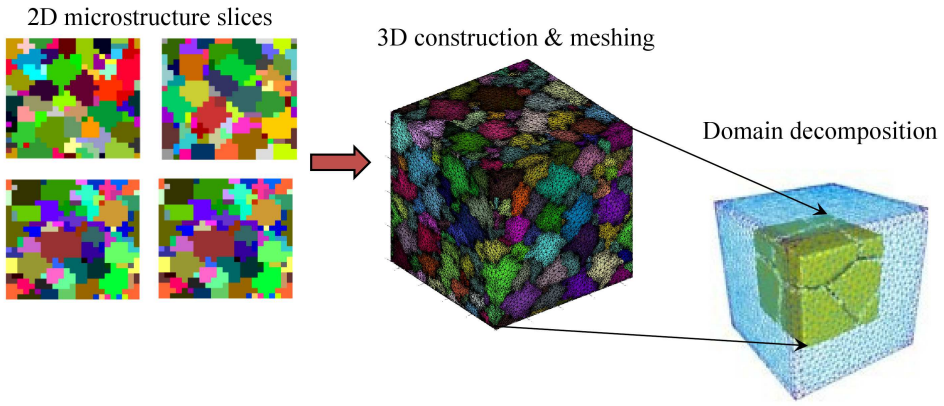

Fig. 3.9 3D microstructure reconstruction, meshing and domain decomposition.

3.6 Summary

A set of computational tools are developed to generate and characterize microstructures for 2D and 3D analysis. This study provides the prerequisite to quantitatively establish the structure-property relations across length scales. Specifically, microstructure generated using methods discussed in this chapter has many advantages over experimental approaches. First of all, microstructures generated using the two-point correlation functions and the ellipsoidal packing algorithm allow systematic variation of one microstructural characteristic while keeping other features as constant. The one-to-one correlation between the microstructure and material fracture toughness facilitates the design of high toughness materials by tailoring of microstructure. In contrast, experimental approaches have limited control of microstructure characteristics as the variation of one microstructural feature usually results the change in other parameters.

Besides, the computer generated microstructures can go beyond current available material configurations and contribute to the design of future materials. They are more cost effective than experimentally prepared samples.

4 EFFECT OF MICROSTRUCTURE ON FRACTURE TOUGHNESS OF CERAMIC COMPOSITES

4.1 Introduction

The design of the high toughness ceramic composites largely depends on the control of the microstructure and constituent properties. This task requires in-depth understanding of how microstructure attributes determine the overall fracture behavior through the activation of different fracture mechanisms. In Section 4.2, the overall fracture toughness of two-phase Al_2O_3/TiB_2 ceramics is evaluated as function of microstructural size scale, phase distribution, phase morphology, phase volume fractions, bulk constituent properties and interfacial bonding stiffness using cohesive finite element simulations and a *J*-integral based approach developed in Chapter 2. The prediction includes statistical representation of microstructure as discussed in Chapter 3. Because statistical measures are used, this approach developed applies to microstructures with random heterogeneous phase distributions and fracture processes with arbitrary crack paths or micro-crack patterns. In addition to the evaluation of fracture toughness, the CFEM calculations also allowed the trajectories and crack surface areas (crack lengths in 2D) associated with each fracture mechanism (matrix fracture, matrix/reinforcement interfacial debonding and crack penetration of reinforcement particles) during fracture processes to be quantified. Along with the fracture energy of each type of fracture site, the quantification of the crack surface areas makes it possible to calculate the total energy released and, consequently, the overall energy release rate. The information is used to develop a semi-analytical model in Section 4.3. The quantification of the fracture

toughness is achieved by an assessment of the contributions of different fracture mechanisms including matrix fracture, interfacial debonding and particle cracking to the overall energy release rate. In particular, this assessment involves a statistical characterization of the competition between crack deflection and crack penetration at matrix/reinforcement interfaces. Although the numerical quantification is specific to Al_2O_3/TiB_2 ceramic composites, the approach and the model developed apply to brittle particle-reinforced composites in general.

4.2 Numerical Simulations

Fracture in nature is a stochastic process. Arbitrary microstructural phase morphologies and material heterogeneities lead to the variations of local properties from specimen to specimen and in turn the scattering of facture toughness. The statistical quantification of fracture behavior of a material should be based on a proper consideration of the correlation among three elements: probability distributions characterizing the distribution of flaws and material properties, fracture mechanics and material microstructure. In this Section, two sets of microstructure set with stochastic distributions of phases are employed in the calculations, as shown in Fig. 3.4 and Fig. 3.5. The geometric effects of microstructure on fracture toughness will be discussed first followed by the effects of constituent properties.

4.2.1 Correlation between fracture toughness and microstructural attributes

Microstructural sample set 1, as listed in Fig. 3.4, is employed to study the correlations between the two-point correlation parameter F_{01} and fracture toughness. Note that this set has systematically varying particle radius ($R = s/2 = 20\,\mu m$, $30\,\mu m$ and $40\,\mu m$) and volume fraction ($f = 10\%, 15\%, 20\%, 25\%$ and 30%). For each combination of particle size and volume fraction, 20 randomly generated microstructural instantiations are used to obtain a statistical characterization of the stochastic nature of the failure processes at the microstructure level. For each microstructure setting (each combination of R and f), the probability of fracture initiation is measured in terms of K_{IC}^{i} and the probability of catastrophic fracture is measured by the propagation toughness K_{IC}. Both measurements are through the three-parameter Weibull distribution function [79] in the form of

$$X(K) = 1 - e^{-\Phi(K)}, \text{ where } \Phi(K) = \begin{cases} \left(\dfrac{K - K^L}{K^0} \right)^m, & K^L \le K < \infty; \\ 0, & 0 \le K \le K^L. \end{cases} \tag{4.1}$$

Here, X is the probability of fracture, K can be either the initiation toughness K_{IC}^{i} or propagation toughness K_{IC}, m quantifies the scatter of K, K^L is the lower bound fracture toughness and K^0 is the normalization factor. The parameters K^L, K^0 and m are obtained through a linear regression fit to the 20 data points for each microstructural setting which involves 20 different instantiations.

The Weibull distribution function has been widely used in reliability analysis due to its versatility and relative simplicity [80-82]. The shape (defined by m), size (defined

by K^0) and finite lower bound limit (at $W(K)=95\%$) of the curve make it a better representation of fracture toughness distribution than the normal distribution function whose symmetry about the mean can result in physically unrealistic predictions of the lower bound values [35].

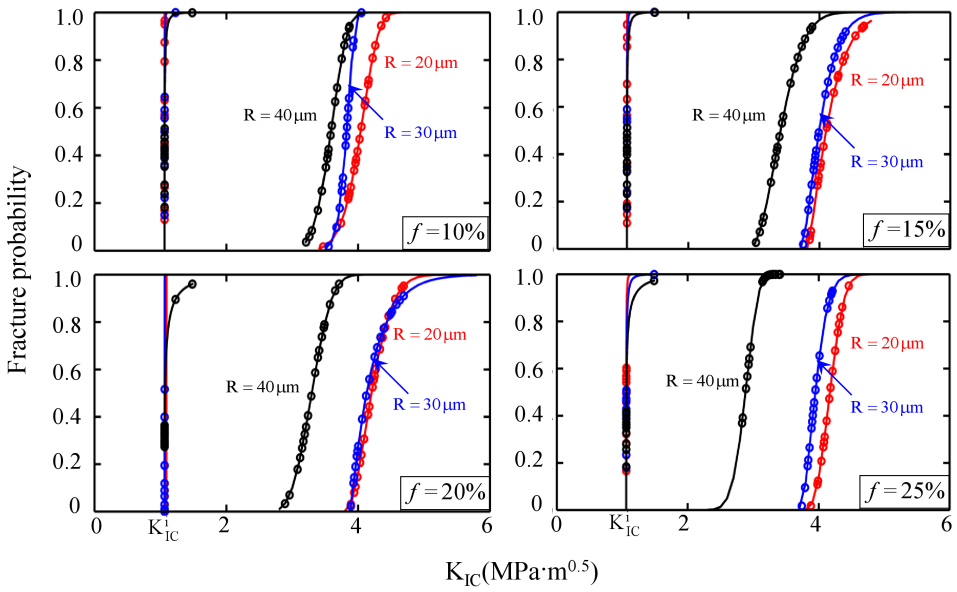

Fig. 4.1 Fracture probability distributions for microstructures with randomly distributed, non-overlapping circular reinforcement particles. The distributions are obtained from twenty random instantiations (samples) of each microstructure.

As shown in Fig. 4.1, microstructure affects K_{IC} much more than K_{IC}^i. The finest reinforcements give rise to the highest propagation toughness, but have the least influence on the initiation toughness. The opposite trends in influence have to do with how cracks interact with particles. If a large particle happens to be at the tip of the pre-crack, a higher level of stress is required to initiate the crack and, consequently, the initiation toughness is higher. Such events are less frequent, as shown in Fig. 4.1. On the

other hand, a propagating crack is more likely to penetrate a large particle, causing immediate catastrophic failure of the material and limited improvement of the propagation toughness.

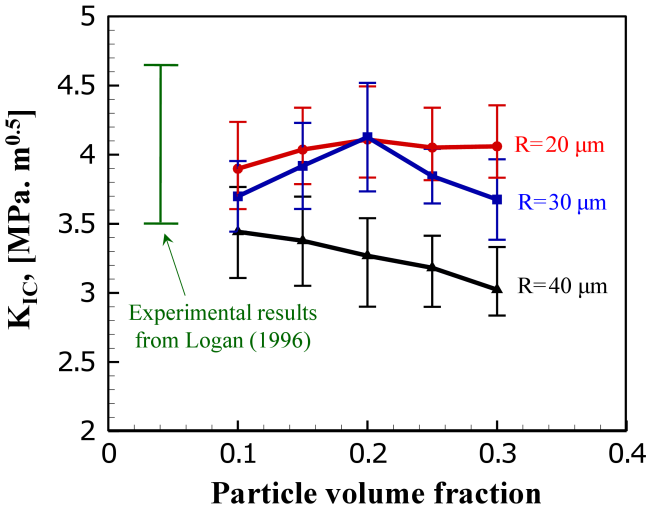

Fig. 4.2 Propagation toughness as a function of reinforcement size and volume fraction. The error bars indicate scatter of results obtained from twenty random instantiations (samples) of each microstructure.

It is worth noting in Fig. 4.2 that the K_{IC} range obtained from the CFEM framework is in good agreement with the experimental results reported by Logan [37] which are also shown. Increasing the reinforcement volume fraction f always enhances K_{IC}^{i}, but does not always enhance K_{IC}. As shown in Fig. 4.2, K_{IC} decreases as f increases when the particles are large ($R = 40\,\mu m$). At $R = 30\,\mu m$, K_{IC} is the highest for $f = 20\%$ and is lower at both $f = 10\%$ and $f = 30\%$. The effect of f becomes less pronounced when R is further decreased to $20\,\mu m$. The above trends are result from relative shifts in the three fracture mechanisms (matrix cracking, interface debonding and

particle cracking) as the microstructure changes. Specifically, it has been reported that particle cracking is more prevalent in composites with higher particle volume fractions [83]. The lower fracture toughness values at larger particle sizes are a result of an increased likelihood of particle cracking [84, 85]. Although crack penetration through a particle requires a higher instantaneous *K* value than crack growth through interfacial debonding, particle cracking usually signifies immediate catastrophic failure. Small particles, on the other hand, promote sustained crack deflections through interfacial debonding as illustrated in Fig. 4.3. Such processes increase the tortuosity of crack trajectory and in turn enhance the fracture resistance.

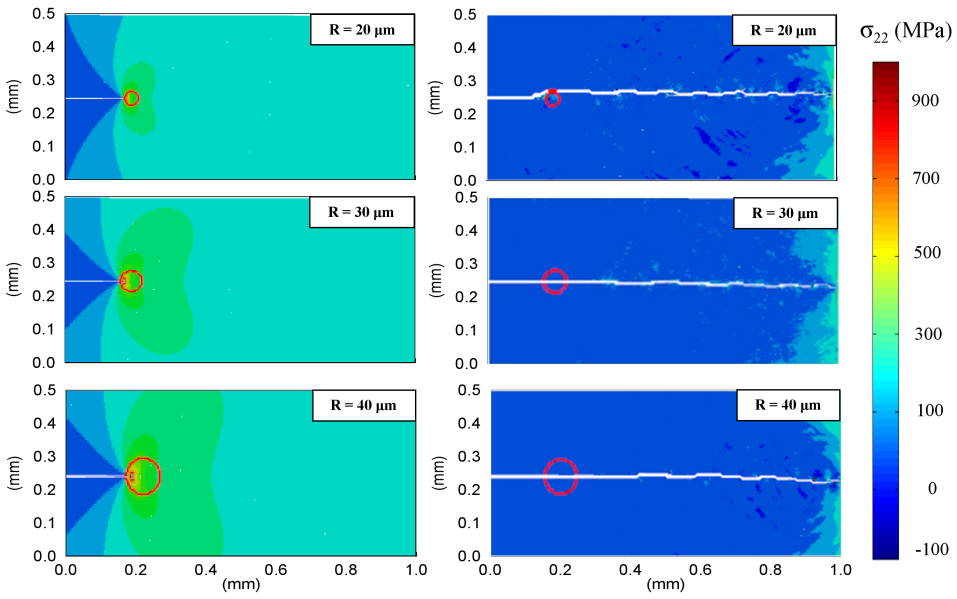

Fig. 4.3 The effect of reinforcement size on fracture mode.

As discussed above, the fracture toughness of a material is not a deterministic quantity even if the microstructure contains uniformly distributed reinforcement particles of the same radius [86]. Therefore, a probabilistic approach which accounts for microstructural morphology is needed. Figure Fig**. 4.4** shows the propagation toughness

K_{IC}^{i} as a function of the two-point correlation parameter F_{01} measured at a crack propagation distance of $D=800\mu m$. It can be seen that microstructures with finer reinforcements (higher values of F_{01}) have higher fracture toughness values due to their higher probability to cause crack arrest.

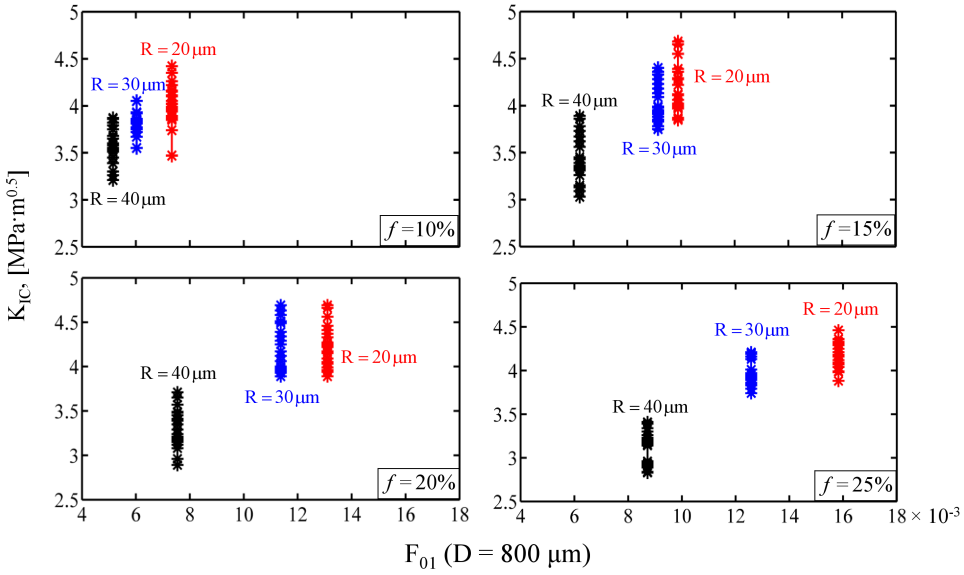

Fig. 4.4 Correlations between T_{max} and crack interaction parameter F_{01}. The scatter of results represents variations among twenty random instantiations (samples) of each microstructure.

Microstructural sample set 2, as shown in Fig. 3.5, is employed to study of the effect of reinforcement shape on fracture toughness. The microstructure with elliptical reinforcement best approximates the real microstructure in terms of two-point correlation (Fig. 3.3) and particle morphology (Fig. 3.6). As a result, this microstructure has very similar K_{IC} values, as shown in Fig. 4.5. In contrast, the microstructures containing reinforcements with higher roundness values (circles and squares) show slightly different

mean fracture toughness values. As we will see later, this is due to more extensive crack deflection associated with the higher-roundness microstructures.

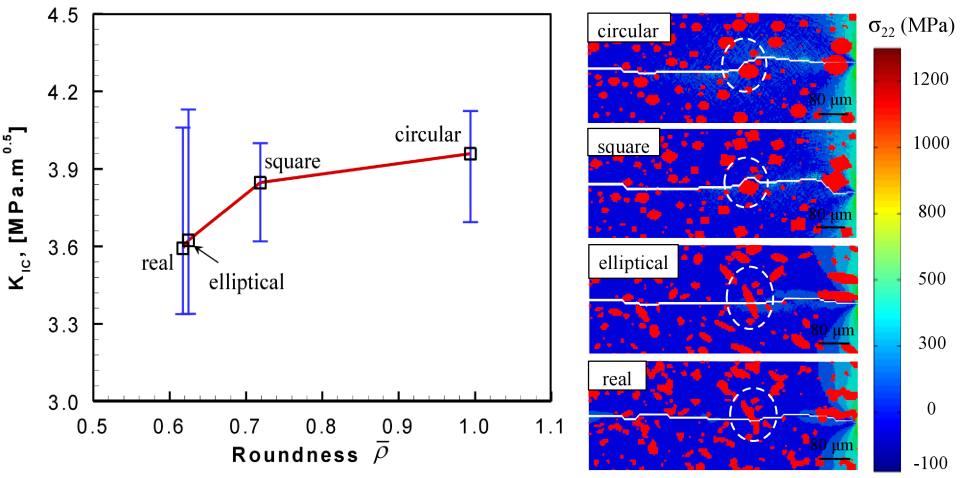

Fig. 4.5 Effect of mean roundness on K_{IC}. The error bars indicate scatter of results obtained from twenty random instantiations (samples) of each microstructure.

4.2.2 Effects of constituent attributes on fracture toughness

The forgoing analyses show in Section 4.2.1, from a morphological perspective, that particle cracking negatively influences fracture resistance, especially in the initial stage of crack-reinforcement interactions. It is equally important to identify the correlation between material attributes and the activation of fracture mechanisms. Here, the effects of reinforcement toughness and compliance of the interface between the reinforcement phase and the matrix on fracture toughness are studied.

Increasing the toughness of the reinforcement Φ_p has only a limited impact on the overall fracture toughness. It can be seen from Fig. 4.6(a) that the increase of fracture

resistance tends to saturate beyond the Φ_p value of $120\,J/m^2$. Specifically, a 200% increase in Φ_p from $300\,\mathrm{J/m^2}$ to $900\,\mathrm{J/m^2}$ only leads to a 16% increase in K_{IC} from $4.4\,MPa\cdot\sqrt{m}$ to $5.2\,MPa\cdot\sqrt{m}$. In contrast, a 200% increase in Φ_p from $40\,J/m^2$ to $120\,J/m^2$ leads to an increase in K_{IC} of 31% from $3.2\,MPa\cdot\sqrt{m}$ to $4.2\,MPa\cdot\sqrt{m}$. A look at crack paths provides insight into this. Figure Fig. 4.6(b) shows that particle cracking occurs even under unrealistically high Φ_p values, if the interfaces are well-bonded. Obviously, increasing Φ_p beyond a certain value has no significant impact on crack path, resulting in diminishing gains in K_{IC}.

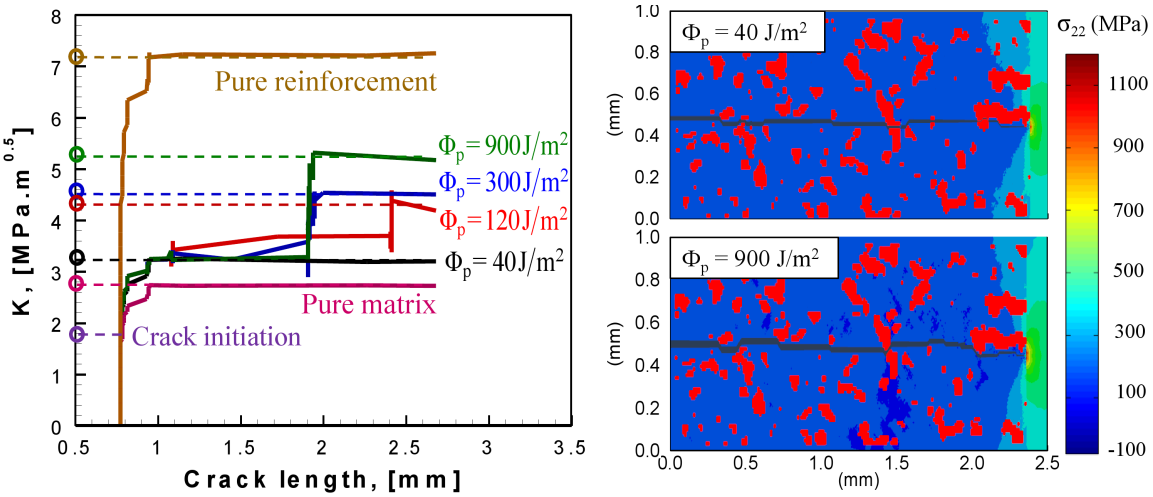

Fig. 4.6 Effect of reinforcement toughness on K_{IC}.

On the other hand, interfacial bonding can significantly influence the dominant fracture mechanism and, consequently, alter the material fracture resistance. It has been proposed in some early studies [84, 87] that under proper conditions, poor interface bonding could increase the fracture energy. A growing crack tends to meander along

weakly bonded interfaces, leading to a tortuous crack trajectory. One way to address the role of interfacial bonding strength is to keep the interfacial fracture energy constant at $\Phi_{in} = 78.5\, J/m^2$ and maintain the same slope of the initial linear portion of the cohesive relation (see Fig. 2.1) at 420 GPa. Under this condition, six different interfacial bonding strength levels ($T_{\max}^{in} = 6\times10^{-6},\ 6\times10^{-4},\ 6\times10^{-3},\ 6\times10^{-2}$, 0.6, and 6 GPa, corresponding to $Q_1 = T_{\max}^{in} / T_{\max}^{0} = 10^{-5}$, 10^{-3}, 10^{-2}, 10^{-1}, 1 and 10, respectively) are considered. Since the fracture energy is the same, the critical separations Δ_{tc} and Δ_{nc} are adjusted accordingly and the corresponding values are $\Delta_{tc} = \Delta_{nc} =$ 6800, 68, 6.8, 0.68, 0.068 and 0.0068 μm. These cases represent very compliant to very stiff interfaces. It should be noted that, as a rule of thumb, the interface is regarded as "well-bonded" if $T_{\max}^{in} \in \left[T_{\max}^{m}, T_{\max}^{p}\right] = [0.48,\ 0.7]$ GPa, where the K^0, $T_{\max}^{m}$ and $T_{\max}^{p}$ (Fig. 2.1) are the cohesive strengths of the interface, matrix and reinforcement, respectively, as listed in Table 1. Here for simplicity, we choose $T_{\max}^{0} = 0.6$ GPa as the baseline case representing the well-bonded case. This baseline is the level used for calculations up to this point. The variations are considered relative to this baseline case. In particular, the case with $Q_1 = T_{\max}^{in} / T_{\max}^{0} = 10^{-5}$ essentially approximates a porous ceramic as though the particles do not exist.

The CFEM results in Fig. 4.7 and Fig. 4.8 show that the stiff interface ($Q_1 = 10$) leads to extensive particle cracking and a 14.7% decrease in K_{IC} relative to the baseline case ($Q_1 = 1$). As the bonding strength decreases (or interfacial compliance increases), more crack deflection into the matrix/reinforcement interfaces occurs, causing K_{IC} to

increase initially, but ultimately decrease between $Q_1 = 10^{-3}$ and 10^{-5}. Particle cracking can be effectively avoided when the interfaces are quite compliant ($Q_1 < 1$). As Q_1 decreases, the interface becomes more ductile as interface debonding gradually outweighs matrix cracking and becomes the dominant fracture mode. It is noted that when $Q_1 = T_{max}^{in} / T_{max}^{0} = 10^{-5}$, the interfacial strength is negligibly small and the material essentially approximates porous ceramics as though the particles do not exist. This scenario is consistent with what has been reported for porous ceramics whose fracture toughness values are lower than two-phase or even single phase ceramics [88]. For $Q_1 = 10^{-3}$ the separation distance required for a complete decohesion of the cohesive elements along the interfaces can exceed the element size. This means that the interface may not fully debond and the damage at the interface cannot be considered as real cracks. However, the compliant interfaces serve as damage initiation sites. These damage sites contribute to energy dissipation and promote the formation of cracks in the matrix and the reinforcement. For complete debonding to occur at the interfaces, much larger microstructure samples than what is currently used and much longer load duration are needed. To simply put, the resulting energy released and fracture toughness value would be higher than what is shown in Fig. 4.8. With the understanding that the K_{IC} value for $Q_1 = 10^{-3}$ in Fig. 4.8 being a conservative underestimate of the actual value, the trend of fracture toughness shown is valid and very illustrative. Specifically, to significantly improve the fracture resistance, the interfacial bonding between the matrix and particles of ceramic composites should balance strength and compliance. Excessively strong/stiff and overly weak or compliant interfaces are both detrimental. The data in Fig. 4.8 also

show that increases of up to 50% in K_{IC} can be achieved by proper engineering of the interfacial bending strength/compliance, under the condition that the overall interfacial fracture energy is kept constant.

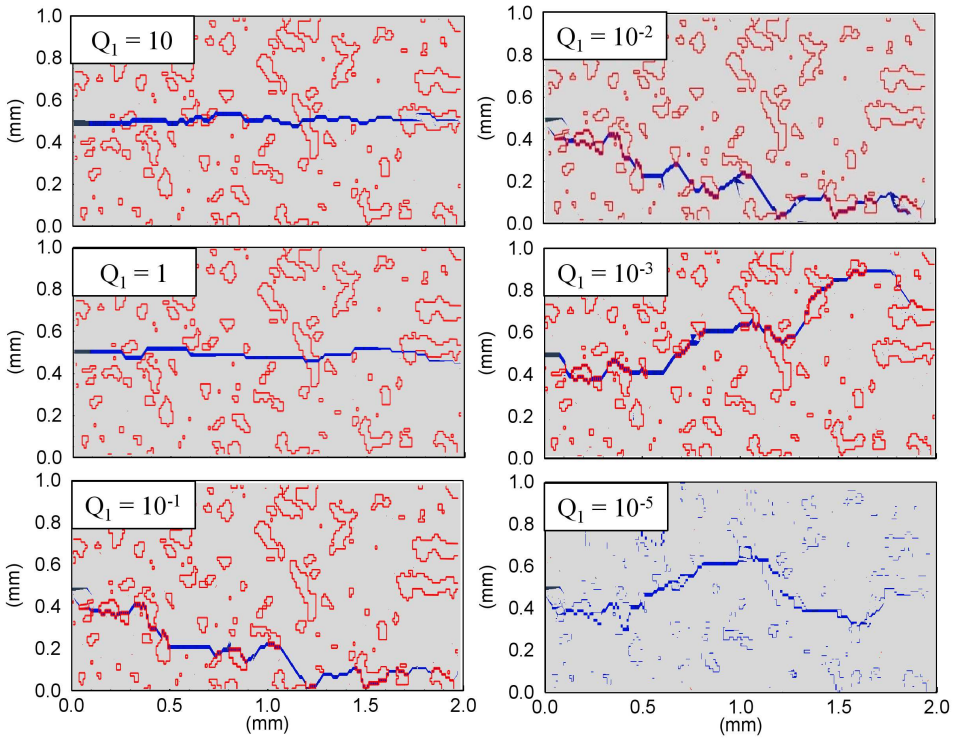

Fig. 4.7 Crack trajectories for different compliance or strength levels of the reinforcement-matrix interface as measured by the strength ratio Q_1.

To illustrate the effect of bonding strength alone on K_{IC}, another set of calculations are carried out, with constant separation $\Delta_{tc} = \Delta_{nc} = 0.068\,\mu m$ so as to keep the interfaces brittle and relatively non-compliant. Under this condition, six different interfacial bonding strength levels ($Q_2 = T^{in}_{max} / T^{0}_{max} = 10^{-5}$, 10^{-3}, 10^{-2}, 10^{-1}, 1 and 10, respectively, $T^{0}_{max} = 0.6$ GPa, the same as before) are considered. These parameters guarantee full interface debonding for all the calculations under the conditions analyzed.

Note that the cohesive energy changes for the six Q_2 levels while the initial slope of the cohesive relations remains constant at 420 GPa. As shown in Fig. 4.9, the trend of K_{IC} is similar to that in Fig. 4.8. However, the peak K_{IC} value occurs around $Q_2 \approx 10^{-1}$. Although lower Q_2 values promote crack deflection into the interface, the improvement in fracture toughness K_{IC} is very limited, as the fracture energy decreases dramatically when $Q_2 < 1$.

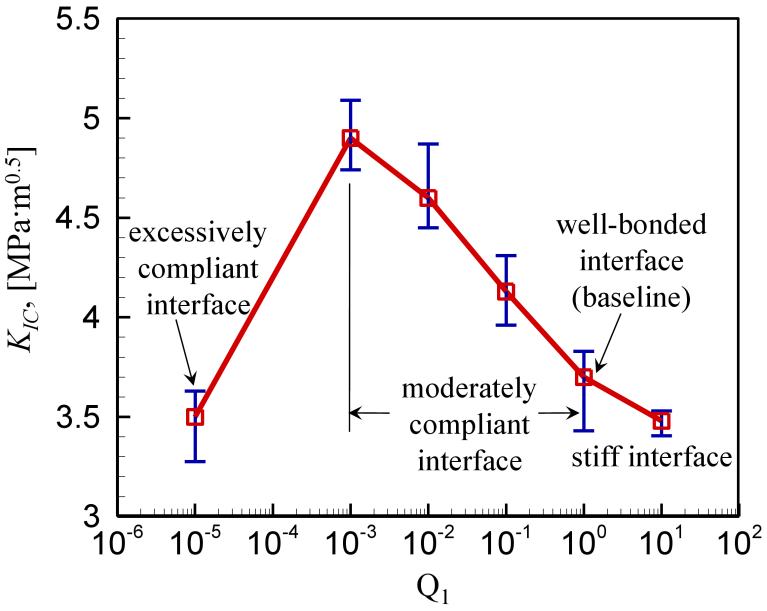

Fig. 4.8 Effect of compliance of the reinforcement-matrix interface as measured by the strength ratio Q_1 on K_{IC}. The error bars indicate scatter of results obtained from twenty random instantiations (samples) of each microstructure.

Noted that the K_{IC} value at $Q_2 = 10^{-5}$ is very close to the result in Fig. 4.8 when Q_1 is at the same value. This is due to the fact that interfacial bonding is essentially non-existent in both cases, effectively yielding a scenario in which the material is equivalent

to a porous ceramic. Similarly, when $Q_2 = 10$, even though the fracture energy of the interface is 10 times that of the baseline case, K_{IC} is very similar to that in Fig. 4.8, due to the fact that interface debonding is completely replaced by particle cracking.

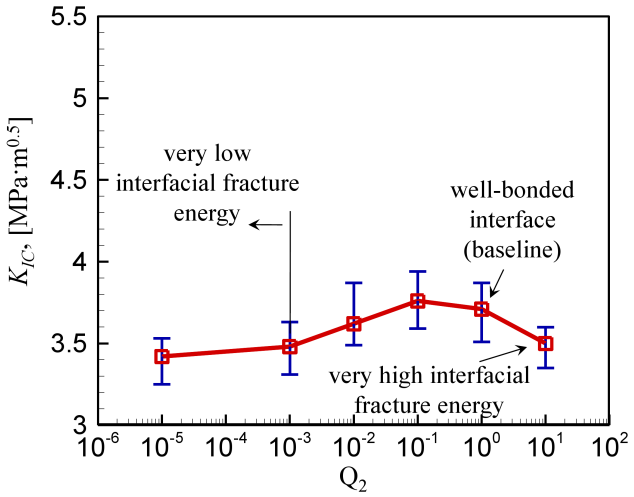

Fig. 4.9 Effect of bonding strength of the reinforcement-matrix interface as measured by the strength ratio Q_2 on K_{IC}. The error bars indicate scatter of results obtained from twenty random instantiations (samples) of each microstructure.

Obviously, the most effective way to improve fracture toughness is to create compliant (ductile) interfaces without sacrificing interfacial fracture energy. FigureFig. 4.8 shows that a properly balance must be maintained between interfacial bonding strength (or compliance) and the promotion of crack deflection. Excessively strong (or stiff) interfacial bonding increases penetration into particles and leads to catastrophic failure. Excessively weak (or compliant) bonding maximizes crack deflection but diminishes the toughening effect of the reinforcement. Both extremes result in lower fracture toughness values of the overall composite. CFEM calculations suggest $Q_1 = T^{in}_{max} / T^{0}_{max}$ values in the

range of 10^{-3} to 10^{-2} offer an appropriate balance to maximize the propagation toughness of the Al_2O_3/TiB_2 material system.

It should be pointed out that the above studies only consider a specific set of microstructures. The parametric studies carried out here does not include all the possible combinations of $T_{\max}^{in}$ and Φ_{in}. The second set of calculations could be expanded to account for different levels of Δ_{tc} with the same variation of $T_{\max}^{in}$ and Φ_{in}. Although the corresponding result might be different, the trend presented here is valid for general cases. The fundamental avenue for toughening is the activation of different fracture mechanisms through the interplays between microstructure attributes which are stochastic on nature. To take advantage of the mechanisms, which can only be influenced in a statistical sense through microstructure design, it is important to quantify the relations between statistical measures for microstructure characteristics and statistical measures for the fracture mechanisms. Such quantification can allow an analytical relation to be established between fracture toughness and microstructure. This will be the topic of the semi-analytical model in section 4.3.

4.3 Semi-Analytical Model

As discussed in Section 4.2, microstructure in terms of geometric distribution of phases, constituent properties and interfacial bonding attributes influences the deformation and failure behavior of heterogeneous materials through the activation of different underlying mechanisms. In particular, the fracture behavior and fracture toughness of materials are determined by the mechanisms through which cracks interact with constituents in microstructures. The toughening is through increases in energy

dissipation when cracks are forced to follow tortuous paths. Based on the results of numerical simulations, a semi-empirical model is developed to predict the fracture toughness of brittle two-phase ceramic composites as a function of statistically defined morphological attributes of microstructure, constituent properties and interfacial bonding characteristics. The quantification of the fracture toughness is achieved by an assessment of the contributions of different fracture mechanisms including matrix fracture, interfacial debonding and particle cracking to the overall energy release rate.

4.3.1 Fracture toughness and energy release rate

For brittle materials, the critical energy release rate J_{IC} is rated to the fracture toughness K_{IC} via

$$K_{IC}^2 = J_{IC}\frac{\overline{E}}{1-\overline{\nu}^2}, \tag{4.2}$$

where $\overline{E}$ and $\overline{\nu}$ are, respectively, the effective Young's modulus and effective Poisson's ratio of the heterogeneous material. For a tortuous crack path involving different types of fracture sites as illustrated in Fig. 4.10, the average energy release rate J can be stated as

$$\begin{aligned} J_{IC} &= \frac{\partial U_f}{\partial A} \approx \frac{\left(\Phi_{in}L_{in} + \Phi_m L_m + \Phi_p L_p\right)t_t}{Wt_t} \\ &= \frac{L}{W}\left(\Phi_{in}\frac{L_{in}}{L} + \Phi_m\frac{L_m}{L} + \Phi_p\frac{L_p}{L}\right) \\ &= \xi(\mathrm{Q}, s, f)\left(\Phi_{in}H_{in} + \Phi_m H_m + \Phi_p H_p\right), \end{aligned} \tag{4.3}$$

where U_f is the total energy released to crack surfaces over the projected crack length W, $A = Wt_t$ is the total projected crack surface area with t_t being the specimen thickness. It should be noted that W is the projection of the total curved crack length (arc length L in 2D) in the direction of crack propagation. Specifically, if L_{in}, L_m and L_p represent the crack arc lengths along the interface, within the matrix and through the reinforcement particles, respectively, $L = L_{in} + L_m + L_p$ represents the total crack arc length. Also in Eqn. (4.3), Φ_{in}, Φ_m and Φ_p are the fracture energies for interface debonding, matrix cracking and particle cracking, respectively. $\xi(\mathrm{Q}, s, f) = L/W$ can be regarded as the crack length multiplication factor (CLMF). It is a function that captures the influences of interfacial compliance as measured by strength ratio Q, reinforcement size scale s [see Section 4.2.2 and Eqn. (3.1) respectively], and the volume fraction f of the reinforcement phase. The specific form of this function is unknown. The value of ξ is determined empirically by fitting to CFEM data calculated in Section 4.2. H_{in}, H_m and H_p are the proportions of crack lengths associated with interface debonding, matrix cracking and particle cracking, respectively. Obviously, the evaluation of H_{in}, H_m and H_p is the primary task in order to predict K_{IC} through Eqns. (4.2) and (4.3). The specific form is

$$K_{IC} = \sqrt{\frac{\bar{E}}{1-\bar{\nu}^2} J_{IC}} = \sqrt{\frac{\bar{E}}{1-\bar{\nu}^2} \xi(\mathrm{Q}, s, f)\left(\Phi_{in} H_{in} + \Phi_m H_m + \Phi_p H_p\right)}. \quad (4.4)$$

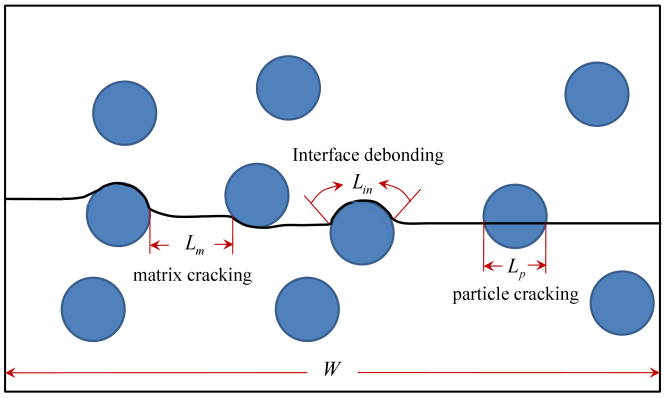

Fig. 4.10 A schematic illustration of crack trajectory in a two-phase composite and crack lengths associated with different fracture mechanisms.

It should be pointed out that the analysis embodied in Eqns. (4.2) through (4.4) applies only to quasistatic crack growth for which crack speed approaches zero. However, it is important to note that, for brittle materials considered here, the evaluation of J_{IC} (and therefore K_{IC}) can be achieved by properly accounting for the effect of crack speed through fully dynamic calculations, especially when the crack speed is low.

4.3.2 Criterion for activation of different fracture mode

The task of evaluating the right-hand side of Eqn. (4.4) constitutes the bulk of the development below. The interaction between the propagating crack and the reinforcement phase determines L_{in}, L_m and L_p and, consequently, H_{in}, H_m and H_p. There are two possible types of fracture path when a crack approaches a matrix/reinforcement interface in a ceramic composite consisting of a matrix phase and a reinforcement phase. The first fracture mode is interface debonding which is an important fracture mechanism for crack deflection and plays a critical role in material toughening. This mode of fracture is

promoted by weak interfacial cohesion, smaller particle size and higher particle roundness. The second fracture mode is particle cracking triggered by crack penetration. This mode of fracture usually signifies catastrophic failure [89, 90] and should be avoided as it leads to lower energy release rate because of straight (shorter) fracture paths, even though the fracture energy of the reinforcement phase is higher than those of the interfaces and the matrix phase. Clearly, it is of great importance to quantify the conditions under which the two competing fracture mechanisms are activated. Such a quantification can guide the design and manipulation of microstructures to enhance the fracture resistance of materials through synthesis.

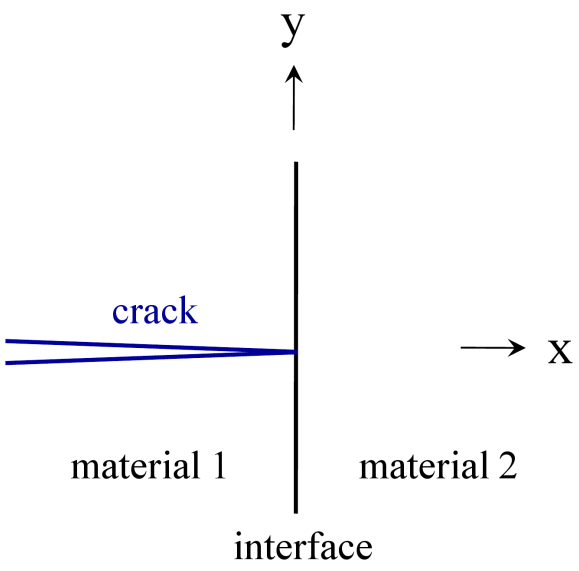

Fig. 4.11 He and Hutchinson's model of crack deflection/penetration at a bimaterial interface.

Currently, two approaches exist for determining the activation of the mechanisms. One involves stress-based criteria governed by local asymptotic stress fields at the matrix/particle interfaces [91, 92]. The other involves energy-based criteria accounting

for the differences in the works of fracture along possible alternative crack paths [93-95]. From the energy perspective, a crack would grow when the energy available in the stress field reaches the energy required to form new fracture surfaces along a certain path. The prediction of crack propagation requires the calculation of the energy release rate J as well as a knowledge about the fracture energy Φ. Here, J_d and J_p are used to denote the energy release rate for crack deflection and crack penetration, respectively. Similarly, Φ_{in} and Φ_p denote the fracture energy of the interface and reinforcement, respectively. For brittle materials, crack deflection at an interface requires $J_d \geq \Phi_d$. Crack penetration, on the other hand, requires $J_p \geq \Phi_p$. It is unclear which fracture mechanism would be activated if both conditions are satisfied simultaneously.

He and Hutchinson [93, 94] analyzed the behavior of a semi-infinite crack perpendicular to an infinite planar interface in a symmetrically loaded, isotropic bi-material, as illustrated in Fig. 4.11. They argued that crack deflection occurs when

$$J_d / J_p > \Phi_{in} / \Phi_p. \tag{4.5}$$

Gupta et al [91, 96] extended He and Hutchinson's work to anisotropic materials and developed a strength criterion for crack deflection and validated their analysis using laser spallation experiments. Subsequently, Martínez and Gupta [97] improved the criterion such that it does not require any assumption concerning crack extension ratio by using a quasi-static approximation and by assuming that deflection occurs under constant loading. They also showed that the energy criterion for deflection is sensitive to material anisotropy.

Although the above analyses concern the interaction between a single crack and an infinite, flat interface, they reveal some of the fundamental relations that govern the behavior of cracks as they approach interfaces. In the following Section 4.3.3, an empirical modification of He and Hutchinson's criterion is developed to allow consideration of the effects of finite reinforcement size, reinforcement shape and phase distribution in a two-phase microstructure. Because of the random nature of material heterogeneities at the microstructure level, the interaction of a propagating crack with the phases in a microstructure is rather random. However, over distances longer than the characteristic size scale of the microstructure, the cumulative effect of the random interactions determine the behavior measured at the macroscopic scale. To capture this cumulative effect in the setting of the two-phase ceramic composites consisting of a matrix and a population of reinforcement particles, a measure reflecting the cumulative probability for a crack to encounter the reinforcement phase is used in the modified criterion. This cumulative probability is obtained from the two-point correlation functions as discussed in Section 3.2. Based on these analyses, a relation between microstructure attributes and overall fracture toughness of the composites is established by assessing the proportion of each fracture mode associated with the crack propagation process.

4.3.3 Fracture mode selection

Characterization of the competition between crack deflection and crack penetration can allow the proportion of each fracture mode to be quantified. He and Hutchinson [93, 94] provided an analysis of crack deflection versus penetration at a symmetrically loaded, isotropic bi-material interface. The problem analyzed involves a

semi-infinite crack perpendicular to the planar bi-material interface as illustrated in Fig. 4.11. The solution of this problem depends on Dundurs parameters [98, 99] in the forms of

$$\begin{cases} \alpha = \left[\mu_1\left(1-\nu_0\right)-\mu_0\left(1-\nu_1\right)\right]/\left[\mu_1\left(1-\nu_0\right)+\mu_0\left(1-\nu_1\right)\right], \quad \text{and} \\ \beta = 0.5\cdot\left[\mu_1\left(1-2\nu_0\right)-\mu_0\left(1-2\nu_1\right)\right]/\left[\mu_1\left(1-\nu_0\right)+\mu_0\left(1-\nu_1\right)\right]. \end{cases} \tag{4.6}$$

Here, μ_i and ν_i are the shear modulus and Poisson's ratio respectively for matrix Al_2O_3 (i = 0) and reinforcement TiB_2 ($i=1$). Both α and β vanish when the matrix and reinforcement materials are identical.

The stress field ahead of the crack-tip is characterized by

$$\sigma_{xx} = k_I\left(2\pi y\right)^{-\lambda} \tag{4.7}$$

where k_I is the amplitude factor proportional to the applied load, λ is a function of α and β satisfying

$$\cos\lambda\pi = \frac{2\left(\beta-\alpha\right)}{1+\beta}\left(1-\lambda\right)^2 + \frac{\alpha+\beta^2}{1-\beta^2}, \tag{4.8}$$

as discussed by Zak and Williams [100].

Along the interface ahead of the crack-tip, the tractions are

$$\sigma_{yy} + i\sigma_{xy} = K\left(2\pi r\right)^{-0.5} r^{i\varepsilon}, \tag{4.9}$$

where r is the distance from the crack-tip, $i=\sqrt{-1}$ and

$$\varepsilon = \frac{1}{2\pi}\ln\left(\frac{1-\beta}{1+\beta}\right) \tag{4.10}$$

is the bi-elastic constant. It should be noted that $K = K_1 + iK_2$ in Eqn. (4.9) is the complex stress intensity factor. K_1 and K_2 are the mode I and mode II stress intensity factors, respectively [101].

It can be shown that the energy release rate for crack penetration is

$$J_p = \frac{1-\nu_1}{2\mu_1}K_1^2 = \frac{1-\nu_1}{2\mu_1}z^2 k_I^2 a_p^{1-2\lambda}, \tag{4.11}$$

where z is a dimensionless function of α and β [93], k_I is amplitude factor, and a_p is the crack extension length into the reinforcement.

Similarly, the energy release rate for crack deflection is

$$J_d = \left(\frac{1-\nu_1}{\mu_1} + \frac{1-\nu_2}{\mu_2}\right)\frac{\left(K_1^2 + K_2^2\right)}{4\cosh^2(\pi\varepsilon)}, \tag{4.12}$$

where

$$K_1^2 + K_2^2 = k_I^2 a_d^{1-2\lambda}\left[|c|^2 + |h|^2 + 2R_e(ch)\right], \tag{4.13}$$

with a_d being the crack extension length along the interface. *c* and *h* are functions of α and β whose expressions will be discussed later.

He and Hutchinson [93] assume that $a_d = a_p$ so that J_d / J_p is independent of the crack extension lengths. The analysis uses the parameter

$$U_0 = \frac{J_d}{J_p} - \frac{\Phi_{in}}{\Phi_p} = \frac{1-\beta^2}{(1-\alpha)z^2}\left[|c|^2 + |h|^2 + 2R_e(ch)\right] - \frac{\Phi_{in}}{\Phi_p} \tag{4.14}$$

to determine the activation of the fracture mechanisms. Crack deflection is predicted when $U_0 > 0$, otherwise, crack penetration into the reinforcement phase is expected. In the above relation, J_d , J_p, Φ_{in} and Φ_p are, respectively, the energy release rates of crack deflection and particle penetration and the surface energies of the interface and reinforcement. For the Al_2O_3/TiB_2 ceramic composite system considered here, Φ_{in} and Φ_p are taken as 78.5 J/m^2 and 102.2 J/m^2, respectively. The calculations of the values of *z*, *c* and *h* are discussed in considerable detail by He and Hutchinson [93].

To account for the effects of finite particle size, particle shape and microstructure phase distribution, we provide an empirical modification of U_0 in the form of

$$U = \frac{1-\beta^2}{a_0(1-\alpha)}\left[|c|^2 + |h|^2 + 2R_e(ch)\right]\bar{\rho}^{a_1} e^{\left(\frac{a_2}{s}\right)} - \frac{\Phi_{in}}{\Phi_p}, \tag{4.15}$$

where $\bar{\rho}$ is the roundness of the reinforcement particle, s represents the characteristic reinforcement size which is obtained by fitting the two-point correlation functions as shown in Eqn. (3.1). Here, P_{ij} denotes the probability for randomly placed vectors of a given length *D* to start in phase *i* (*i* = 0 or 1) and ends in phase *j* (*j* = 0 or 1). The matrix is defined as phase 0, while the reinforcement phase is defined as phase 1. More details

about the two-point correlation functions could be found at Section 3.2. For microstructures with randomly distributed circular particles of the same diameter, s is equal to the diameter. The values of s for the microstructures analyzed are given in Fig. 3.4. P_{01} can be regarded as the geometric probability of encountering the reinforcement phase by a crack of length D that is propagating in the matrix.

To facilitate parametric studies, the coefficient c and h are approximated as [102]

$$\begin{cases} c = \dfrac{1}{2}\sqrt{\dfrac{1-\beta}{1+\alpha}}\left(e^{-\frac{i\omega}{2}} + e^{-\frac{3i\omega}{2}}\right), & \text{and} \\ h = \dfrac{1}{4}\sqrt{\dfrac{1-\beta}{1-\alpha}}\left(e^{-\frac{i\omega}{2}} - e^{-\frac{3i\omega}{2}}\right), \end{cases} \tag{4.16}$$

respectively, over the crack incident angle range of $0 \le \omega \le \pi/2$ (see Fig. 4.12).

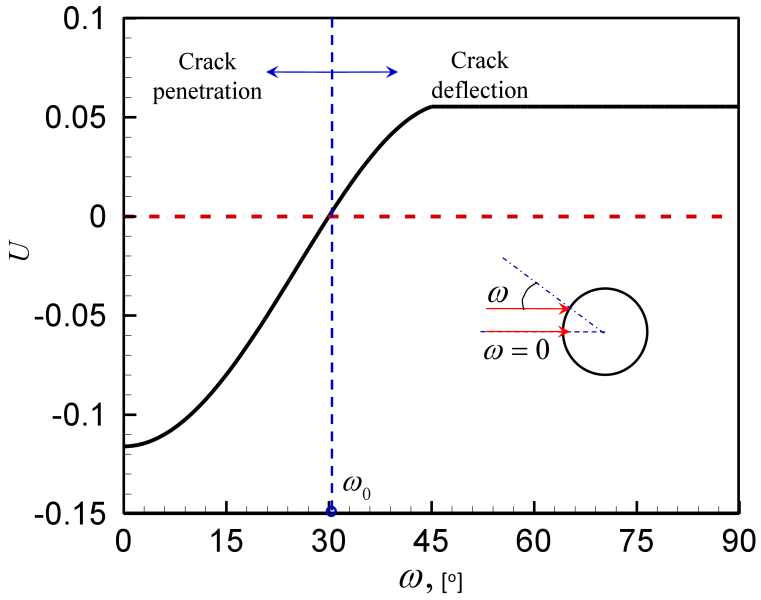

Fig. 4.12 Parameter U for the determination of crack penetration and crack deflection at a matrix/particle interface.

Implied in Eqn. (4.15) is the fact that smaller and more rounded (Fig. 4.1, Fig. 3.6 and Fig. 4.5, respectively) particles enhance fracture toughness by inducing crack deflection. It should be noted that U reduces to U_0 for a circular particle ($\bar{\rho}=1$) whose size approaches infinity, since $\lim_{s\to\infty}\bar{\rho}^{a_1}e^{\left(\frac{a_2}{s}\right)}\to 1$. To best describe the CFEM results, the values of the parameters are chosen as $a_0=1.3$, $a_1=0.185$ and $a_2=5.5$ through curve fitting.

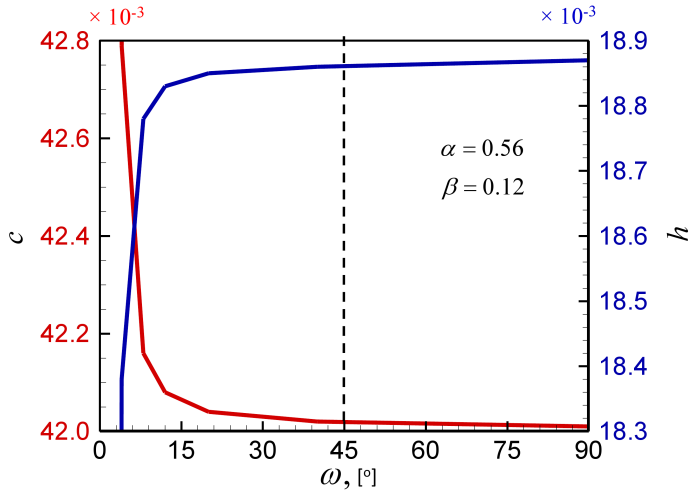

Fig. 4.13 Dependence of parameter c and h on the crack incident angle ω.

As shown in Fig. 4.12, the crack deflects at the interface when $U>0$, otherwise, it penetrates into the reinforcement and causes particle cracking. The effect of crack incident angle ω is through coefficients c and h in Eqn. (4.16). According to He and Hutchinson [93, 94], both c and h tend to saturate when $\omega>45^{\circ}$, as shown in Fig. 4.13.

Furthermore, Veljkovic [102] has demonstrated that the error associated with the form of c and h in Eqn. (4.16) is within 1% when $0^\circ < \omega < 45^\circ$. Therefore, it is quite reasonable to assume that $U(\omega) = U(45^\circ)$ i.e., crack deflects, when $\omega > 45^\circ$. The probability of crack deflection is, therefore,

$$p = \frac{\int_{\omega_0}^{\pi/2} U d\omega}{\int_0^{\pi/2} |U| d\omega}. \tag{4.17}$$

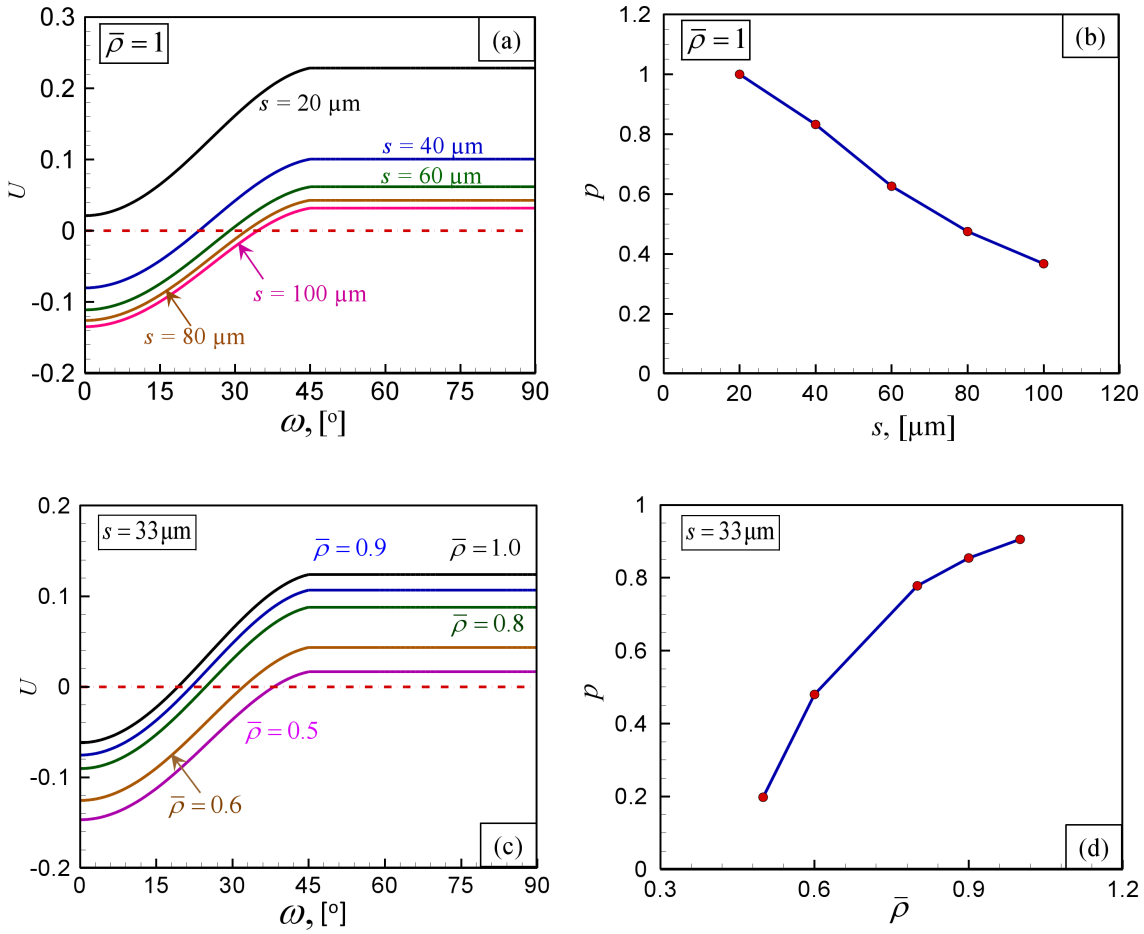

Fig. 4.14 (a) U as a function of crack incidence angle ω (Fig. 1) for different reinforcement sizes and a fixed mean roundness of 1, (b) effect of reinforcement size on

the probability of crack deflection, (c) U as a function of crack incidence angle ω for different reinforcement mean roundness values and a fixed reinforcement size of $s = 33\,\mu\text{m}$ and (d) effect of mean roundness on the probability of crack deflection.

Here, ω_0 denotes the critical crack angle beyond which crack deflection will occur. The likelihood of crack deflection increases as ω increases or as crack direction deviates from the direction normal to the interface, as illustrated in Fig. 4.12 and shown in Fig. 4.14. Obviously, $\omega = 0^\circ$ represents the least likely scenario for crack deflection.

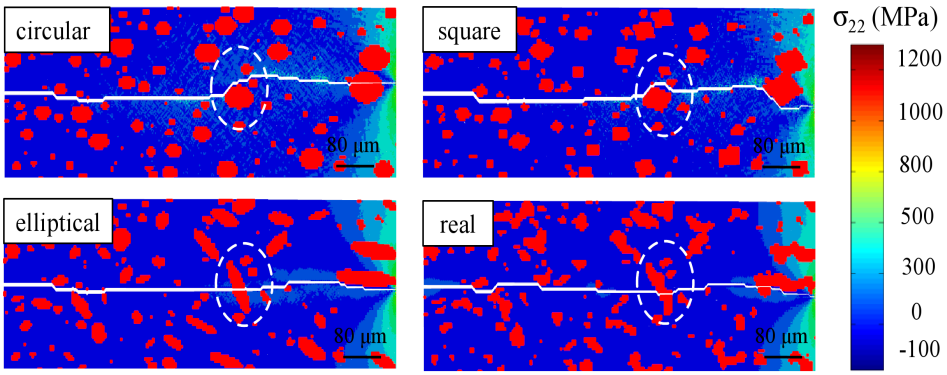

Fig. 4.15 CFEM results showing the effect of reinforcement roundness on fracture mode. All conditions except the particle shape are the same in the cases shown.

Reflecting the trend in the CFEM results, reinforcement size also has a significant impact. As shown in Fig. 4.14(a) which is generated using Eqn. (4.15), larger particles are more susceptible to crack penetration. The critical size scale for avoiding penetration under the conditions considered is approximately $s = 20\,\mu\text{m}$ for the materials and conditions of the CFEM calculations on which the analysis here is based. This trend is confirmed by the CFEM results shown in Fig. 4.3. The calculations are carried out under identical conditions, except the size of the particle in front of the crack. As the size of the

particle ($\bar{\rho}=1$) increases beyond $s=20\mu m$, a fracture mode transition from crack deflection to crack penetration is clearly observed. Under a fixed s, Fig. 4.14(b, d) shows that higher $\bar{\rho}$ values favor crack deflection and, therefore, enhance K_{IC}. This trend is also confirmed by the CFEM results shown in Fig. 4.15. Note that the average roundness $\bar{\rho}$ for the circular, square, elliptical and real reinforcements is 1.0, 0.72, 0.62, and 0.62, respectively. As $\bar{\rho}$ decreases from 1 to 0.62, a fracture mode transition from deflection to crack penetration is observed, leading to decreased propagation fracture toughness K_{IC} as illustrated in Fig. 3.6 and Fig. 4.5.

4.3.4 Influences of different mechanism on fracture toughness

To predict K_{IC}, it is important to quantify the probability of occurrence (also referred to as the proportion from here on) for each fracture mechanism over a given crack propagation distance. Here, we take interfacial debonding as an example. The proportion of interfacial debonding over a distance *D* is the product of (i) the cumulative probability of the crack encountering the reinforcement phase over *D* and (ii) the probability of crack deflection *p*. It should be noted that crack deflection can occur through either matrix cracking or interfacial debonding. Therefore, account must be taken of the interfacial bonding strength and the fracture energies of the interfaces and the matrix. The relation that accounts for the above factors (fracture mechanism, fracture toughness and microstructure characteristics) can be empirically described as

$$\begin{cases} H_{in}(D) = \dfrac{\int_0^D \mathrm{P}_{01}(D)\,dx}{D}\, p\left(\dfrac{\Phi_{in}}{\Phi_m}\right)^{-a\ln(\mathrm{Q})}, \\ H_p(D) = \left(\dfrac{\int_0^D \mathrm{P}_{01}(D)\,dx}{D}(1-p) + \dfrac{\int_0^D \mathrm{P}_{11}(D)\,dx}{D}\right)\left(\dfrac{\Phi_{in}}{\Phi_m}\right)^{-b\ln(\mathrm{Q})}, \text{ and} \\ H_m(D) = 1 - H_{in}(D) - H_p(D). \end{cases} \quad (4.18)$$

Here, H_m, H_{in} and H_p denote the proportions of matrix cracking, interface debonding and particle cracking, respectively. Φ_{in}, Φ_m and Φ_p are the fracture energies of the interface, matrix and reinforcement, respectively. Their values are taken as 78.5 J/m^2, 21.5 J/m^2, and 102.2 J/m^2, respectively. a and b are dimensionless parameters determined by fitting the relations to the CFEM results. P_{01} and P_{11} are two-point correlation functions. $\mathrm{Q}_1 = \mathrm{T}^{in}_{\max} / \mathrm{T}^{0}_{\max}$ is the interfacial bonding strength ratio, with $\mathrm{T}^{in}_{\max}$ being the interfacial cohesive strength and $\mathrm{T}^{0}_{\max}$ being a baseline reference strength of 0.6 GPa. This reference value is the average value of the cohesive strengths of the matrix and reinforcement. $\mathrm{T}^{in}_{\max}$ affects the interfacial cohesive energy Φ and has a significant impact on fracture behavior.

In the analysis carried out here, two scenarios are considered. In the first set of calculations, the interfacial cohesive energy Φ is kept constant while $\mathrm{T}^{in}_{\max}$ and the critical separations (Δ_{tc} and Δ_{nc}) are varied accordingly. The specific range of bounding strength considered here is $10^{-5} \le \mathrm{Q}_1 = \mathrm{T}^{in}_{\max} / \mathrm{T}^{0}_{\max} \le 10$. These cases represent very ductile (small Q_1 values) to very brittle interfaces with $\mathrm{Q}_1 = 1$ being the well-bonded case. They

can also be regarded as representing very weakly and very strongly bonded interfaces. In the second set of calculations, the critical separation is kept constant at $\Delta_{tc} = \Delta_{nc} = 0.068\,\mu m$ while T_{max}^{in} and, therefore, the interfacial cohesive energy Φ are varied accordingly. The range of cohesive strength ratio considered in this case is also $10^{-5} \le Q_2 = T_{max}^{in} / T_{max}^{0} \le 10$. The only difference compared with the first scenario is that the interfaces remain brittle for all the Q_2 cases. It should be noted that the separation needed to achieve full debonding is Δ_c = 6800 μm for $Q_1 = 10^{-5}$, while the interfacial fracture energy is $\Phi = 10^{-5}\Phi_{in}$ for $Q_2 = 10^{-5}$ (Φ_{in} being cohesive energy of the interface for the baseline case of $Q_2 = 1$). Both situations effectively yield a scenario in which there is essentially no bonding between the two phases. Under these conditions, the calculations represent the behavior of a porous ceramic with the particles being pores. When $Q_1 = Q_2 = 10$, there is negligible differences between the two scenarios since the crack barely goes through the interfaces. The largest discrepancy comes from the range $10^{-3} \le Q_1(Q_2) \le 10^{-1}$. In order to capture the two scenarios, $a = 0.4$ and $b = 2$ are chosen for the cases with Q_1, while $a = 0.63$ and $b = 1.54$ are used for cases with Q_2.

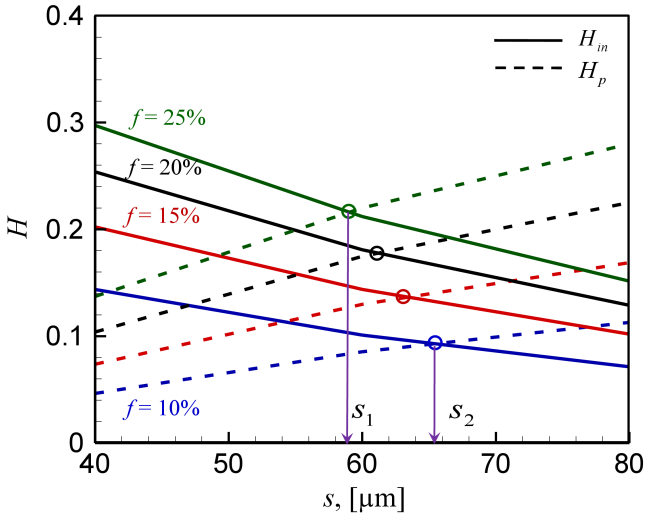

Fig. 4.16 Proportions of interfacial debonding and particle cracking H_{in} and H_p for different values of s and f.

To quantify the relative effects, Fig. 4.16 shows H_{in} and H_p as functions of reinforcement size s and reinforcement volume fraction f. The circular symbols signify the transition in the dominant fracture mechanism under a specific f. On the left side of each transition point (smaller s), interface debonding dominates as H_{in} is always above H_p. On the right hand side (larger s), particle cracking dominates. To maintain the dominance of interface debonding for $10\% \le f \le 25\%$, $s < s_1$ is preferred. When s is within the range of $[s_1, s_2]$, a shift of dominant fracture mode is observed. For example, when $s = 65\,\mu\text{m}$, particle cracking clearly dominates for $f > 20\%$. This explains the peaking of K_{IC} for $R = 30\,\mu\text{m}$ ($s \approx 2R$) in the CFEM results in Fig. 4.17. A comparison of the analytical results in Fig. 4.16 and the CFEM results in Fig. 4.17 shows that f has

little effect on K_{IC} when interfacial debonding is dominant. In contrast, increasing f has a negative effect on K_{IC} when particle cracking is dominant [90].

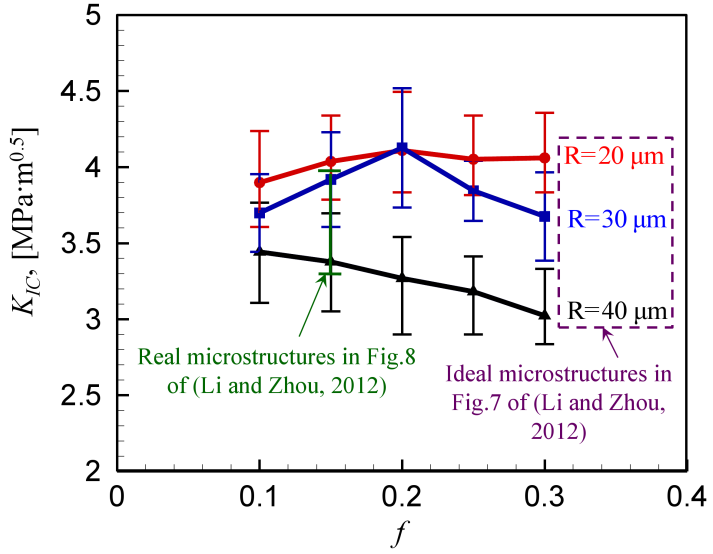

Fig. 4.17 Effect of reinforcement size and volume fraction on K_{IC}. K_{IC} values are calculated from CFEM simulations at different particle volume fractions and particle sizes.

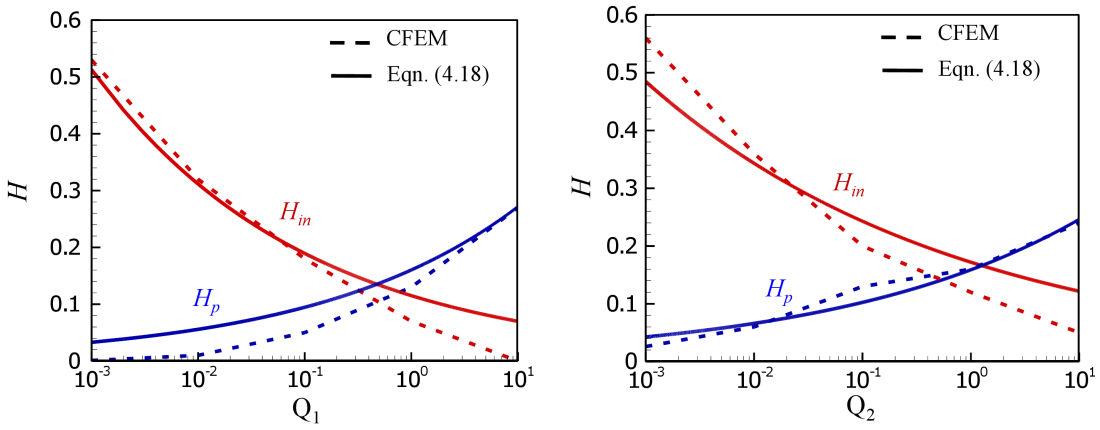

Fig. 4.18 Comparison of crack proportions H_{in} and H_p as calculated from CFEM simulations and predicted by Eqn. (4.18).

It is well established that the fracture toughness material can be significantly enhanced through the introduction of compliant interfaces between the matrix and reinforcement [103, 104]. Our CFEM results demonstrate that crack deflection can always be induced if $Q_1(Q_2) < 1$, regardless of the level of interface fracture energy Φ_{in} [105]. More extensive crack deflection tends to occur at lower $Q_1(Q_2)$ values which leaves the reinforcement intact. The effect of $Q_1(Q_2)$ on fracture mechanisms is systematically captured by Eqn.(4.18). As shown in both plots in Fig. 4.18, particle cracking can be avoided when $Q_1(Q_2) < 1$. As $Q_1(Q_2)$ decreases, interface debonding gradually outweighs matrix cracking and becomes the dominant fracture mode. It should be noted that the best toughening results can only be achieved without sacrificing the interfacial fracture energy. As demonstrated in Fig. 4.19, the improvement in fracture toughness K_{IC} is minor for cases among Q_2 as discussed above, although there is a greater amount of interface debonding compared with the cases with Q_1. This is due to the fact that the interfacial fracture energy drops drastically as Q_2 decreases. Therefore, a proper balance between interfacial compliance and the activation of interface debonding must be maintained to best improve K_{IC}.

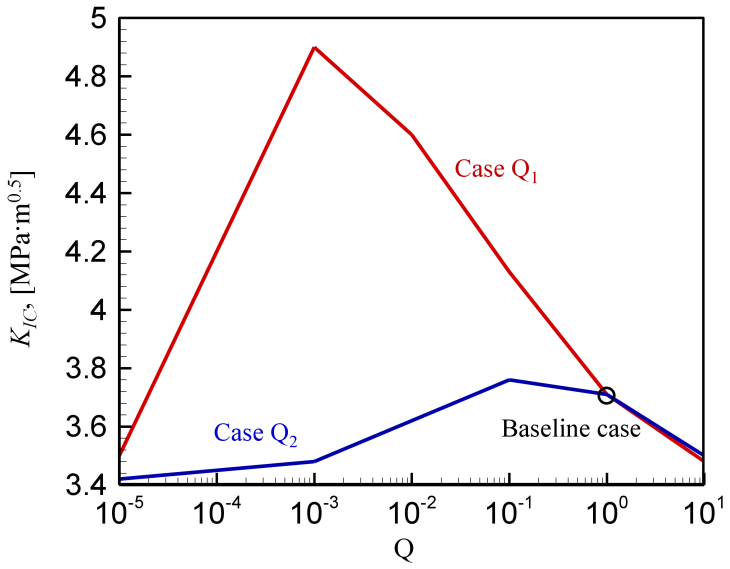

Fig. 4.19 CFEM results showing the effect of interfacial bonding strength on K_{IC}.

The model engendered by Eqn. (4.18) accounts for the effects of both the geometric attributes (characteristic reinforcement size , volume fraction , roundness) and the material attributes (interfacial bonding strength ratio of the interface between the reinforcement and the matrix phase) of the microstructure on the proportion of each fracture mechanism. For the material system analyzed, development of microstructure-fracture toughness relations entails quantitatively correlating the fracture mechanisms with the fracture toughness. To illustrate the point, the values of the microstructures in Fig. 3.4 and Fig. 3.5 are employed. The predicted proportions of interfacial debonding and particle cracking from the CFEM results and the analytical model are compared in Fig. 4.20. Both the model and the CFEM data show that if the interfacial fracture energy is kept constant as $\Phi_{in} = 78.5\, J/m^2$ while the interfacial bonding strength ratio Q_1 varies, the propagation fracture toughness K_{IC} can be improved by 37.2% as the proportion of interfacial debonding increases from approximately 5% to 50%. Moreover,

an increase in the fraction of particle cracking by the same magnitude has the opposite effect on K_{IC}.

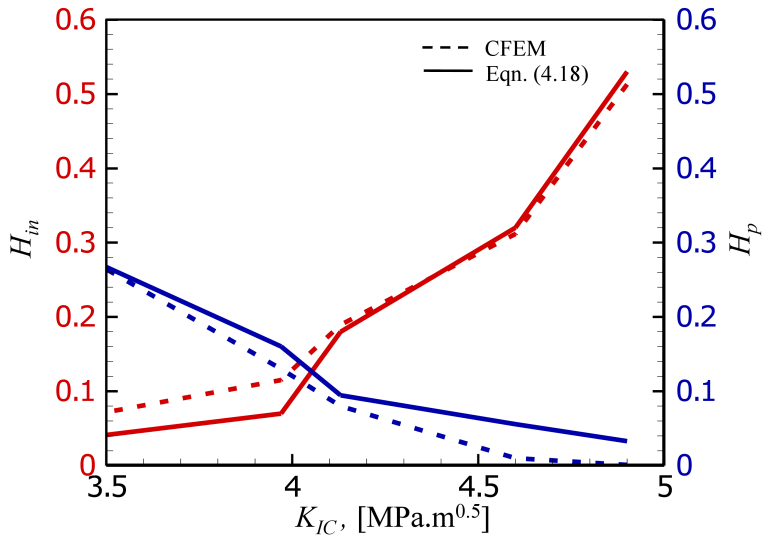

Fig. 4.20 Effect of interfacial debonding and particle cracking on K_{IC}.

4.3.5 Physical implications of Crack Length Multiplication Factor (CLMF)

As discussed previously, the prediction of fracture toughness K_{IC} through Eqn. (4.4) requires the evaluation of $\xi(\mathrm{Q}, s, f)$, which is defined as L/W or the crack length multiplication factor (CLMF). Here, L and W are the real arc length and projected crack length, respectively. Since the model we proposed here only considers quasi-static crack propagation, ξ only depends on heterogeneity-induced crack trajectory variation. In this sense, the crack length multiplication factor $\xi \geq 1$ for all cases. The minimum value of ξ is obtained at $f = 0$ and $f = 1$ when the whole microstructure is pure matrix

or reinforcement, respectively. In both cases, no heterogeneity-induced crack deflection exists and the propagating crack follows the straight trajectory. $\xi(\mathrm{Q}, s, f)$ accounts for the influences of interfacial bonding strength, reinforcement size and volume fraction on total crack length. The functional of $\xi(\mathrm{Q}, s, f)$ is fitted to the CFEM data using the empirical form

$$\xi(\mathrm{Q}, s, f) = \tilde{\xi}(s, f)\tilde{\xi}(\mathrm{Q}). \tag{4.19}$$

Specifically, $\tilde{\xi}(\mathrm{Q})$ is fitted at $s = 66.14\,\mu\mathrm{m}$ and $f = 15\%$. To account for both the Q_1 and Q_2 cases, $\tilde{\xi}(\mathrm{Q})$ takes the form

$$\tilde{\xi}(\mathrm{Q}) = \begin{cases} n_1 \mathrm{Q}_1^{n_2}, \\ n_3 \mathrm{Q}_2^{n_4}. \end{cases} \tag{4.20}$$

Similarly, $\tilde{\xi}(s, f)$ is fitted at $\mathrm{Q} = 1$, when $\tilde{\xi}(\mathrm{Q} = 1)$ is taken as a constant. To best represent the CFEM data, $\tilde{\xi}(s, f)$ takes the form of

$$\tilde{\xi}(s, f) = \frac{1 - e^{D_2}}{e^{D_1} - e^{D_2}} e^{D_1 f} + \frac{e^{D_1} - 1}{e^{D_1} - e^{D_2}} e^{D_2 f} \tag{4.21}$$

where $D_1 = m_1 s + m_2$ and $D_2 = m_3 s^{m_4} + m_5$.

The parameters $n_1 = 1.191$, $n_2 = -0.044$, $n_3 = 1.167$, $n_4 = -0.047$, $m_1 = 0.0175$, $m_2 = -1.483$, $m_3 = -4.7 \times 10^{-12}$, $m_4 = 6.695$ are chosen such that the best fit to the data is achieved.

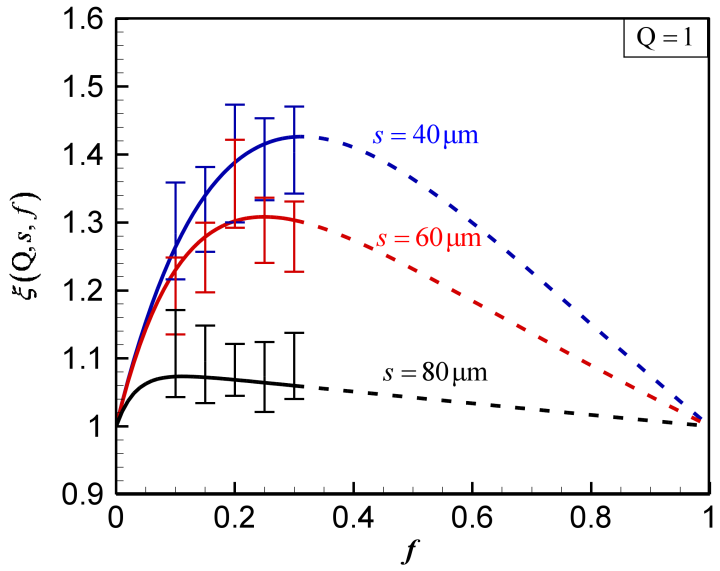

Fig. 4.21 Effect of reinforcement size s on crack length multiplication factor $\xi(\mathrm{Q}, s, f)$.

$\xi(\mathrm{Q}, s, f)$ can be used to quantitatively explain the counterintuitive phenomenon that microstructures with larger and higher volume fractions of tougher reinforcement particles have lower fracture toughness K_{IC} values (Fig. 4.17) even though the fracture energy of the particles is 4.75 and 1.3 times thoset of the matrix and interface, respectively. The physical implication of ξ is demonstrated in Fig. 4.21. The boundary constraints of ξ are well satisfied since $\xi = 1$ resides at $f = 0$ and $f = 1$, as expected. It should be noted that the CFEM data are only available within the solid portion of curves as represented by the error bars. The dashed parts, which are extrapolated according to Eqn. (4.19), also make physical sense. First of all, the increase of reinforcement size s tends to decrease ξ across the whole range of volume fraction f. This is in good agreement with the criterion in Eqn. (4.15) as well as the CFEM results in Fig. 4.17, since small reinforcements promote crack deflection and in turn the tortuosity of the crack path. It can be argued that there exists an upper bound of reinforcement size beyond which ξ approaches 1 (i.e., particle penetration essentially always occurs). As shown in Fig. 4.22, $s_{\max} \approx 85\,\mu\mathrm{m}$ is predicted as the upper bound of the reinforcement size. As s approaches $s_{\max}$, volume fraction f becomes less important as ξ quickly saturates to 1

due to diminishing crack deflection. Although decreasing s can effectively increase ξ, the lower bound of s cannot be ignored. At $s = 0$, the material is essentially the pure matrix with $f = 0$. This means decreasing the reinforcement size beyond the lower bound $s_{\min}$ adversely influences ξ. Currently, our CFEM model cannot precisely predict the value of $s_{\min}$ since the allowed minimum mesh size is $7\ \mu m$. However, for most engineering cases, the predicted trend is still valid.

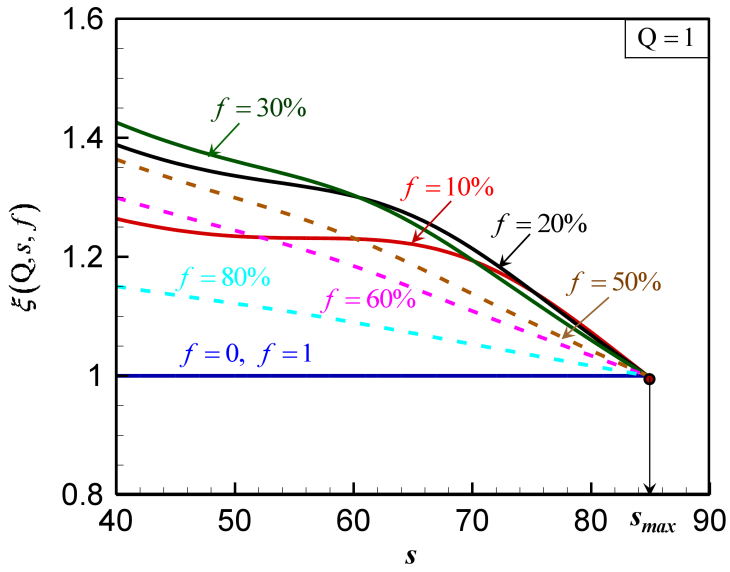

Fig. 4.22 Effect of reinforcement volume fraction f on crack length multiplication factor $\xi(Q, s, f)$.

It can be seen from Fig. 4.21 that the peaks of the curves gradually shift toward the right as s decreases. Specifically, the maximum value of ξ at $s = 40\,\mu m$, $60\,\mu m$ and $80\,\mu m$ are 1.4263, 1.3083 and 1.0735, for $f = 31\%$, 23% and 11%, respectively. The data indicate that particle cracking tends to dominate over interface debonding as f goes beyond each individual thresholds. This again explains the trend in Fig. 4.17 that at $s = 60\,\mu m$, K_{IC} increases with f initially but follows the opposite trend as f goes

beyond 20%, which is very close to 23% as predicted above. Besides, the predicted f thresholds at $s = 40\,\mu\text{m}$ and $80\,\mu\text{m}$ also explain the fact that K_{IC} either increases or decreases monotonically with f, since the lower and upper bounds of f considered in our CFEM calculations are 10% and 30%, respectively. The dashed lines in Fig. 4.22 represent cases that are not considered in the CFEM calculations. It is shown that ξ continuously decreases with f and eventually overlaps with the case at $f = 0$ when f increases to 100%. This is consistent with the above discussions and the trend demonstrated in Fig. 4.21.

In addition to reinforcement size s and volume fraction f, the interfacial bonding strength Q also has a significant influence on ξ. The cases considered in Fig. 4.23 have the same reinforcement size $s = 66.14\,\mu\text{m}$ and volume fraction $f = 15\%$. It is noted from Fig. 4.23(a) and Fig. 4.23(b) that ξ follows a very similar trend for both Q_1 and Q_2. ξ tends to reach 1 as crack deflection is gradually eliminated by the increasing interfacial bonding strength. On the other hand, the maximum value of ξ is around 2, suggesting that the largest possible crack length magnificantion is about two times the projected crack length.

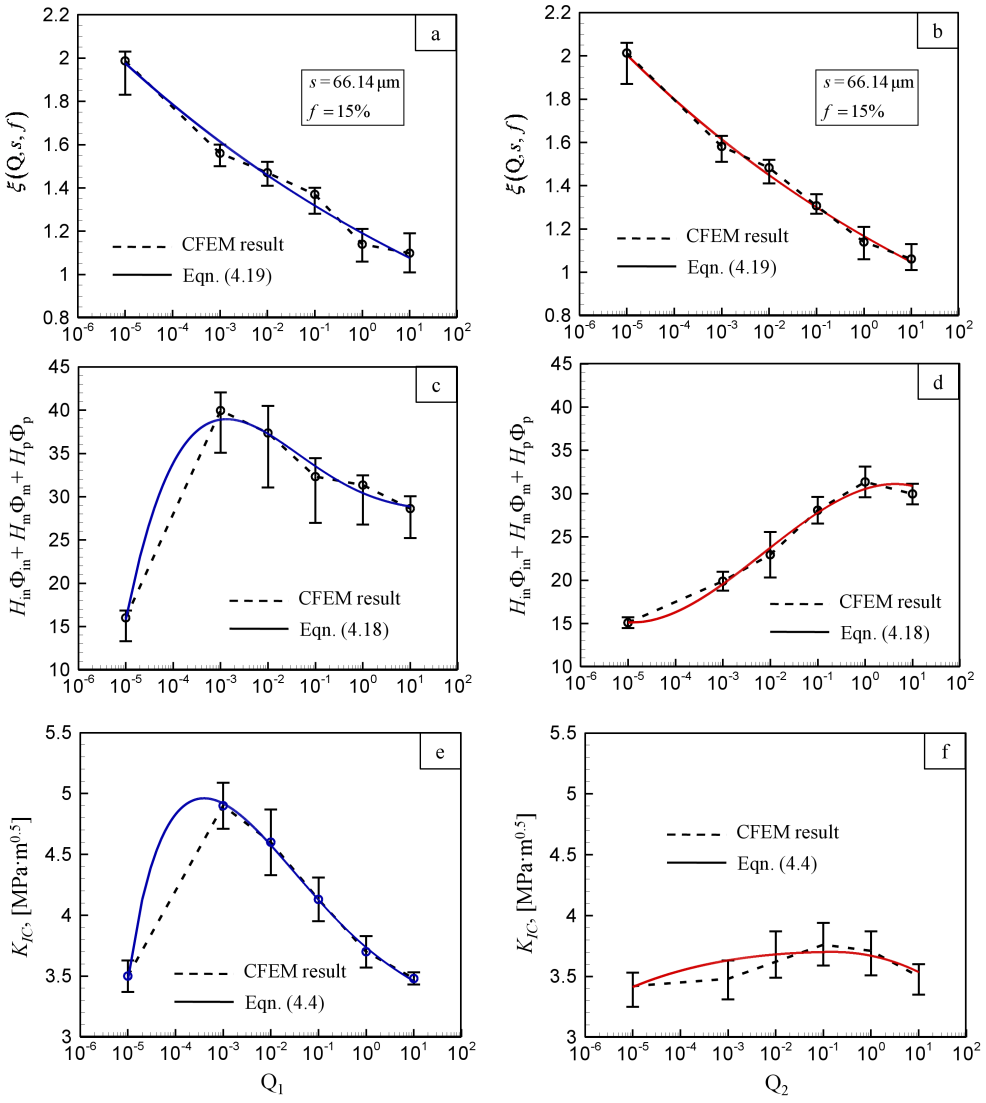

Fig. 4.23 Effect of interfacial bonding strength ratios, (a). Q_1 on ξ at constant interface fracture energy, (b). Q_2 on ξ at constant critical cohesive separation distance, (c). fracture energy releases per unit crack length for case (a), (d). fracture energy released per unit crack length for case (b), (e). corresponding K_{IC} values for case (a), and (f). corresponding K_{IC} values for case (b).

On the other hand, $H_{in}\Phi_{in}+H_m\Phi_m+H_p\Phi_p$ is the equivalent dissipated energy per unit projected crack length. The competition between this term and ξ determines the level of K_{IC}. Fig. 4.23(c) and (d) show that the value of $H_{in}\Phi_{in}+H_m\Phi_m+H_p\Phi_p$ is lowest when both Q_1 and Q_2 are extremely small, leading to diminishing improvement in K_{IC} even though the corresponding ξ tends to the highest possible value. The diametrically opposite effect but the same outcome is observed for extremely large Q_1 and Q_2 values, when the CLMF ξ is the lowest and moderately high or high $H_{in}\Phi_{in}+H_m\Phi_m+H_p\Phi_p$ values are seen.

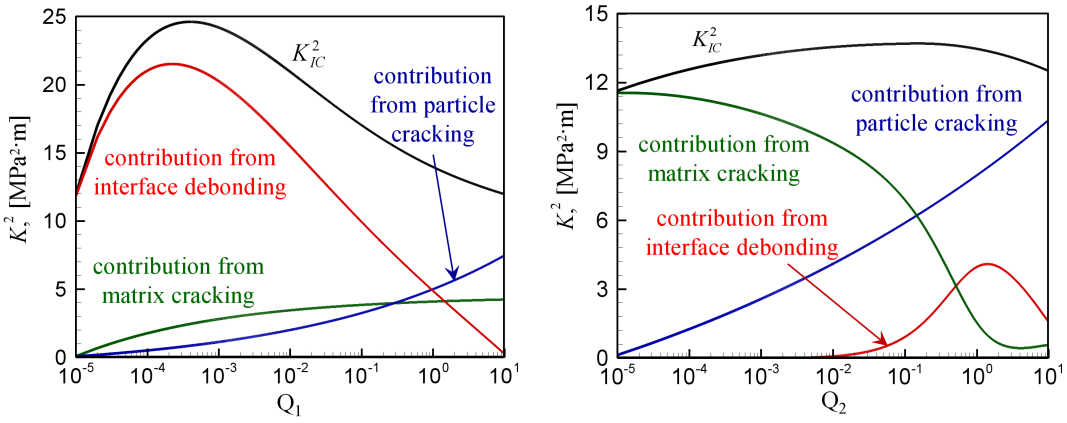

* contribution from interface debonding : $\bar{E}\xi(Q, s, f)\Phi_{in}H_{in}/(1-\bar{\nu}^2)$;

contribution from particle cracking : $\bar{E}\xi(Q, s, f)\Phi_p H_p/(1-\bar{\nu}^2)$;

contribution from matrix cracking : $\bar{E}\xi(Q, s, f)\Phi_m H_m/(1-\bar{\nu}^2)$.

Fig. 4.24 Contributions of individual fracture mechanism to the overall fracture toughness.

Noted that, for both the Q_1 and Q_2 cases, the maximum value of K_{IC} is obtained when ξ and $H_{in}\Phi_{in}+H_p\Phi_p+H_m\Phi_m$ are balanced. Specially, the best improvement of K_{IC} is achieved when the increase in ξ is not at the expense of decreasing $H_{in}\Phi_{in}+H_p\Phi_p+H_m\Phi_m$. To better understand this issue, the individual contributions from different fracture mechanisms to K_{IC} are shown in Fig. 4.24. For this purpose, note that the contribution to K_{IC}^2 from interface debonding is $\bar{E}\xi(Q, s, f)\Phi_{in}H_{in}/(1-\bar{\nu}^2)$, from particle cracking is $\bar{E}\xi(Q, s, f)\Phi_pH_p/(1-\bar{\nu}^2)$, and from matrix cracking is $\bar{E}\xi(Q, s, f)\Phi_mH_m/(1-\bar{\nu}^2)$. Clearly in Fig. 4.24(a), K_{IC} is dominated by the effects of interface debonding when the matrix/reinforcement interface is compliant or relatively weak, i.e., $Q_1\in[10^{-5},0.5]$. In contrast, interface debonding makes the least contribution to K_{IC} when $Q_2\in[10^{-5},0.5]$, as illustrated in Fig. 4.24(b). This is due to the rapid decay of Φ_{in} when $Q_2<1$. On the other hand, the contribution from particle cracking is the largest in both sets of data when Q_1 or $Q_2=10$.

Most importantly, Fig. 4.24(a) shows that the maximum contribution from particle cracking (which occurs at Q_1=10) is less than half of the maximum contribution from interface debonding (which occurs near $Q_1\approx10^{-3}$) even though $\Phi_p=1.3\Phi_{in}$ (baseline case). The fundamental reason is that it is more energetically favorable for cracks to propagate along the path that requires the lowest fracture energy. Crack deflection into the matrix/reinforcement interface causes the crack trajectory to become more tortuous, leading to higher ξ. This significantly increases the crack surface area

and compensates for the relatively lower fracture energy of the interface. Indeed, as shown in Fig. 4.18(a), the value of H_{in} can be 16 times the value of H_p (note that the maximum value of the ratio between the two quantities occurs at the left end of the curves), making interface debonding by far the dominant mechanism for altering energy dissipation. Since Φ_{in} does not change with Q_1 for this case, the best strategy to improve K_{IC} is to maximize H_{in} by promoting crack deflection through the optimization of Q_1 rather than to increase the fracture energy of reinforcement Φ_p or the particle volume fraction f. The latter two measures can help, but their effects are very limited as shown in Fig. 4.25 and Fig. 4.22. When the cases with varying Q_2 values are considered, maximizing H_{in} through the optimization of Q_2 can still improve K_{IC}. However, the effect becomes less pronounced as the contribution of H_{in} to the increase of ξ is much less significant in light of the decrease in Φ_{in}.

4.4 Summary

A cohesive finite element method (CFEM) based multiscale framework for analyzing the effects of microstructural heterogeneity, phase morphology, phase size, constituent behavior, and interfacial bonding strength on the fracture toughness of materials is developed. The computational framework allows the fracture initiation toughness and propagation toughness to be predicted as functions of microstructural attributes and constituent behavior. The method uses the *J*-integral and the linear elastic relation between *J* and *K*. The evaluation applies to steady-state crack propagation for which the driving force for fracture and fracture resistance of the material are in balance.

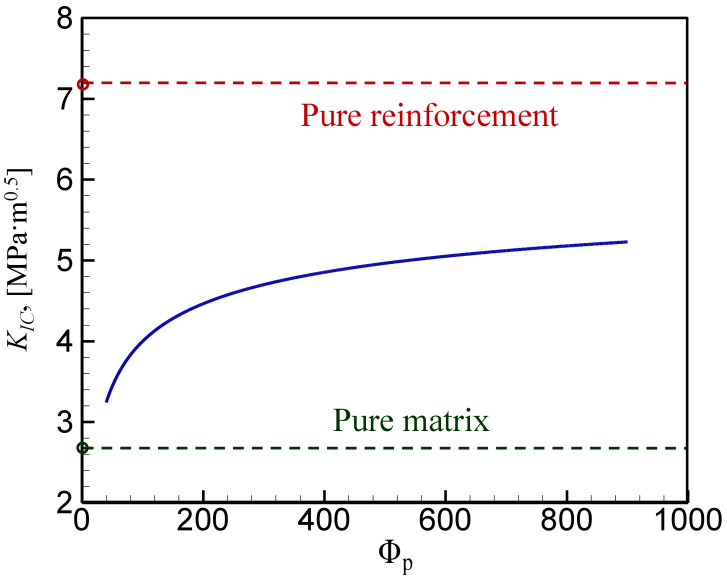

Fig. 4.25 Effect of reinforcement toughness on K_{IC}.

Calculations carried out concern Al_2O_3/TiB_2 two-phase ceramic composites and focus on the fundamental fracture mechanisms during crack initiation and propagation. Results of CFEM calculations show that both microstructure and constituent properties can significantly influence fracture behavior and combine to determine the overall fracture toughness through the activation of different fracture mechanisms. Interface debonding is the most beneficial fracture mechanism and is primarily promoted by small reinforcement size, rounded particle shapes and appropriately bonded and compliant reinforcement-matrix interfaces. In contrast, particle cracking, which triggers catastrophic material failure, usually occurs in microstructure with large reinforcement particles, lower particle roundness and over-bonded/stiff interfaces. Important constituent parameters are the fracture toughness of the matrix phase and the toughness of the interface between the matrix and the reinforcement phases. In contrast, increasing the toughness of the reinforcement phase beyond a certain level has only diminishing

influence. CFEM calculations suggest a properly balanced level of interfacial bonding can maximize the fracture toughness of the materials if the interfacial fracture energy is kept constant as Φ_{in}. In the setting of this paper, $Q_1 = T_{max}^{in} / T_{max}^{0}$ values in the range of 10^{-3} to 10^{-2} offer an appropriate balance to maximize the propagation toughness of the Al_2O_3/TiB_2 material system.

The forging analyses point out that the fundamental avenue for toughening is the activation of different fracture mechanisms through the interplays between microstructure attributes which are stochastic on nature. To take advantage of the mechanisms, which can only be influenced in a statistical sense through microstructure design, it is important to quantify the relations between statistical measures for microstructure characteristics and statistical measures for the fracture mechanisms. An energy-based semi-empirical model is developed to quantify the results of CFEM predictions of fracture toughness of two-phase ceramic composites and to provide an analytical relation between the fracture toughness and microstructure. This semi-empirical model is based on the analytical model of Hu and Hutchinson for the behavior of a crack approaching a planar bi-material interface and accounts for the effects of statistical attributes of microstructures (two-point correlation function, particle size, particle volume fraction, particle shape and phase distribution) and material properties (constituent properties and interfacial bonding strength) by quantifying the probability for the activation of different fracture mechanisms (crack deflection and crack penetration of reinforcement).

For ceramic composites systems like the Al_2O_3/TiB_2 composites analyzed here, the competition between crack deflection and reinforcement penetration plays the most

important role in determining the dominant fracture mode and in turn the fracture toughness. Results of CFEM calculations and predictions of the semi-empirical model show that both microstructure and constituent properties can significantly influence the fracture behavior and combine to determine the overall fracture toughness through the activation of different fracture mechanisms. The analytical model provides deeper insights into the fracture process as it quantitatively predicts the proportion of each fracture mechanism in the heterogeneous microstructure. To enhance the propagation fracture toughness, fine microstructure size scale, rounded reinforcement morphology and appropriately weak bonding strength should be introduced to promote interface debonding and discourage particle cracking. There is an optimal level of interfacial stiffness that maximizes the fracture toughness. These conclusions can be used in the selection of materials and the design of new materials with tailored properties.

5 EFFECT OF MICROSTRUCTURE ON FRACTURE TOUGHNESS OF METAL ALLOYS

5.1 Introduction

In brittle materials, such as ceramic composites discussed in Chapter 4, the total energy released is equivalent to the material surface energy. Therefore, the most effective way to improve the fracture toughness of brittle material is to increase crack tortuosity by introducing refined second-phase reinforcements, appropriately balanced interphase bonding strength and grain bridging, etc [23, 24, 84, 106, 107]. For ductile materials, the fracture resistance becomes a sum of energy contributions from both surface energy and plastic deformation. In polycrystalline metals, intergranular fracture usually leads to tortuous crack path by promoting crack propagation along grain boundaries. However, it discourages the energy dissipation through plastic deformation and does not always lead to high fracture toughness. Transgranular fracture, on the other hand, forms smaller areas of fracture surfaces but allows more significant plastic energy dissipation and more ductile response [108]. Therefore, the design of polycrystalline metals with improved fracture toughness requires in-depth understanding of two levels of competitions:

1. The competition between material deformation and crack formation;
2. The competition between transgranular fracture and intergranular fracture.

Experimentally and numerically, a number of representative approaches, such as the crack-tip opening displacement (CTOD) testing, the crack-tip opening angle (CTOA) testing and *J*-integral measurement, have been used to evaluate the fracture toughness of

ductile materials [109, 110]. However, these approaches do not provide physical insights in quantifying the above competitions. The overall energy dissipation in terms of bulk plasticity and surface creation cannot be separated and quantified. Besides, microstructure characteristics are not considered.

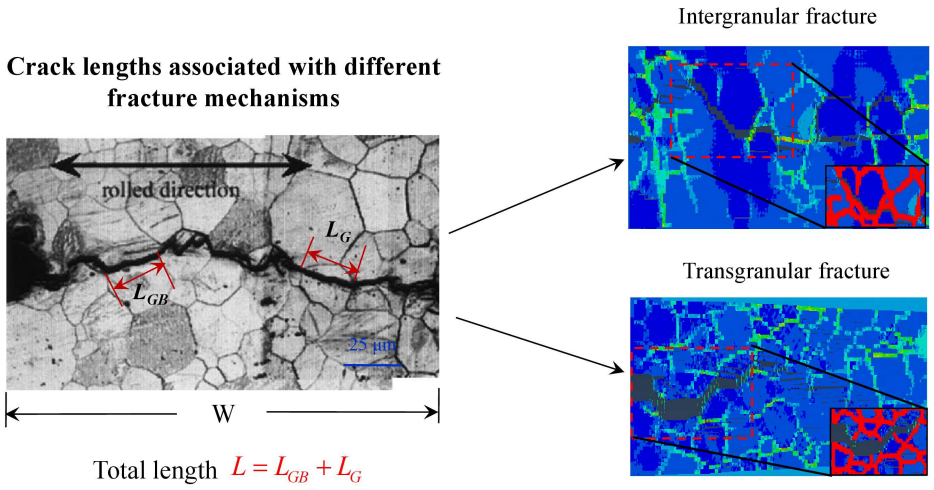

Fig. 5.1 A schematic illustration of crack trajectory in AZ31 Mg alloy and crack lengths associated with different fracture mechanisms. Left picture reproduced from Ref [111].

The 2D CFEM based framework as discussed in Section 2.3 is employed to quantify the two levels of competition by considering the microstructure. The global energy release rate and the fracture toughness of ductile materials are predicted by calculating the *J*-integral in the homogenized region. The fracture surface energy for individual failure mechanism is evaluated through explicit simulation of crack propagation in the microstructure region. The calculations carried out here concern AZ31 Mg alloy and primarily focus on the two levels of competitions. A preliminary study of Ti-6Al-4V alloy using the 3D framework will be presented as well.

5.2 Competing Mechanisms in 2D Polycrystalline Metals

A typical crack path in AZ31 Mg alloy includes both transgranular and intergranular fracture as shown from the experimental work by Somekawa and Mukai [111] in Fig. 5.1. The energy release rate J can be stated as

$$\begin{aligned} J = \frac{\partial U_f}{\partial A} = J_s + J_p &\approx \frac{\left(\Phi_G L_G + \Phi_{GB} L_{GB}\right) t_t}{W t_t} + \frac{\int_0^t \left(\int_V \boldsymbol{\sigma} : \dot{\boldsymbol{\varepsilon}}^{pl} dV \right) dt}{W t_t} \\ &= \xi_s \left(\frac{\mathrm{T}_{\max}\big|_G}{\sigma_y}, \frac{\mathrm{T}_{\max}\big|_{GB}}{\sigma_y} \right) \left(\Phi_G H_G + \Phi_{GB} H_{GB} \right) + \frac{\int_0^t \left(\int_V \sigma : \dot{\varepsilon}^{pl} dV \right) dt}{W t_t}, \end{aligned} \tag{5.1}$$

where J_p and J_s denotes the energy release rate in terms of plastic dissipation and surface formation, respectively. U_f is the total energy released over the projected crack length W. $A = W t_t$ is the total projected crack surface area with t_t being the specimen thickness. It should be noted that W is the projection of the total curved crack length (arc length L in 2D) in the direction of crack propagation. Specifically, $L = L_G + L_{GB}$ with L_G and L_{GB} represent the crack arc lengths within the grains and along the grain boundaries, respectively. Accordingly, H_G and H_{GB} are denoted as the proportions of crack lengths associated with transgranular and intergranular fracture. H_G and H_{GB} can be explicitly extracted from the CFEM simulations. Φ_G and Φ_{GB} are the fracture energies within the grains and along the grain boundaries as defined in Eqn.(2.1). $\xi(\mathrm{Q}, s, f) = L / W$ is again defined as the crack length multiplication factor (CLMF) as discussed in Section 4.3. It is a function that captures the influences of microstructural

attributes on the crack tortuosity. $T_{max}\big|_g$ and $T_{max}\big|_{gb}$ are the cohesive bonding strength within the grains and along the grain boundaries.

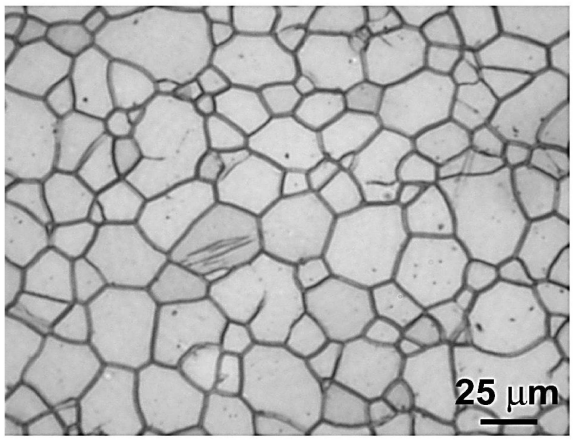

Fig. 5.2 Real microstructure of AZ31 Mg alloy [112].

The key advantage of this semi-analytical model is that it circumvents the difficulty of calculating J_p. As indicated in Eqn.(5.1), the integration of $\boldsymbol{\sigma}:\dot{\boldsymbol{\varepsilon}}^{pl}$ over the entire microstructure region is not trivial. This proposed method allows J_p to be quantified as $J - J_s$ during the course of crack initiation and propagation.

Three sets of calculations are conducted to systematically analyze the effect of yield stress and cohesive strength of the grains/grain boundaries on the activation of failure mechanisms and the influence on the overall fracture toughness. A realistic AZ31 Mg microstructure in Fig. 5.2 is employed in the following studies.

5.2.1 Effect of yield stress

In the first set of calculations, the cohesive elements in the grains and along the grain boundaries follow the same traction-separation law as $\Phi_g = \Phi_{gb} = 7.5\,\mathrm{KJ/m^2}$ and $\mathrm{T_{max}}\big|_g = \mathrm{T_{max}}\big|_{gb} = 350\ \mathrm{MPa}$. This indicates that transgranular and intergranular fracture are equally likely to occur on one account. The only variation considered here is the yield stress of the grains. It is assumed that all the grains share the same yield stress. The microstructure is considered as isotropic. In the following calculations $\sigma_y = [100, 575]\,\mathrm{MPa}$ with an interval of 25 MPa are employed.

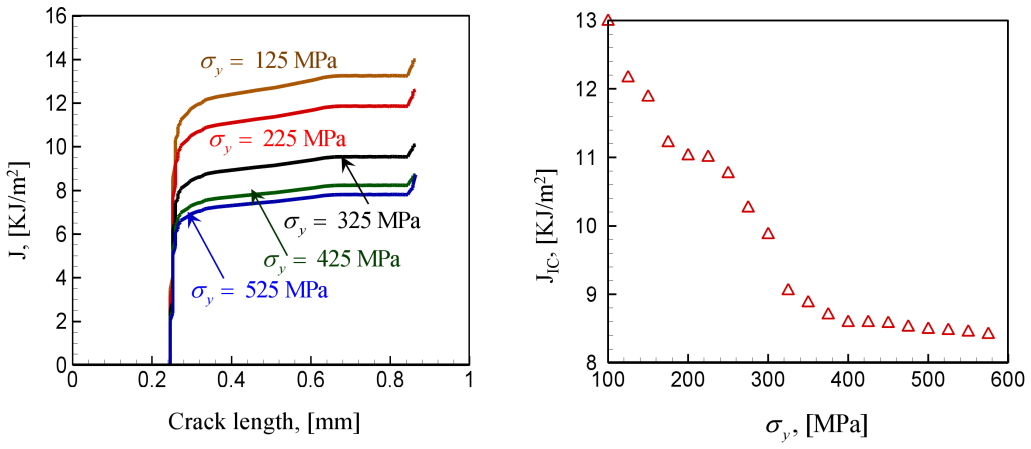

Fig. 5.3 (a) Evolution of *J* during the crack propagation, and (b) J_{IC} predicted under different σ_y.

It is noted from Fig. 5.3(b) that increasing the yield stress of grains leads to decreased fracture toughness. For steady state crack growth, the driving force represented by *J* balances out the material fracture resistance. As shown in Fig. 5.3(a), each *J*-a curve eventually reaches a plateau when the applied driving force reaches the material's maximum capacity to resist the propagating crack. Therefore, the average values of *J*

along each plateau are defined as the corresponding J_{IC}. For elastic-plastic materials under small scale yielding, the propagation fracture toughness K_{IC} is calculated according to

$$K_{IC} = \sqrt{\frac{J\bar{\bar{E}}}{1-\bar{\nu}^2}}. \tag{5.2}$$

More details regarding extraction of J_{IC} and K_{IC} can be found in Section 2.5.

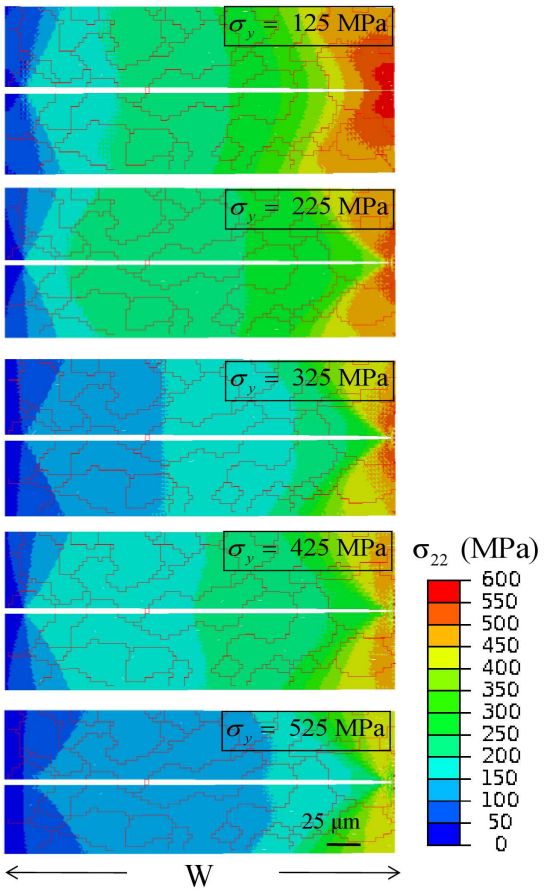

Fig. 5.4 Crack propagation in an isotropic microstructure under differ yield stresses.

Although the grains and grain boundaries have the same possibility to fracture, the crack tends to go through the grains instead of following the grain boundaries. As illustrated in Fig. 5.4, transgranular fracture is the only failure mode observed. The change of grain yield stress has a negligible effect on the crack path as the total crack length L is approximately equivalent to the projected length W. Therefore, the crack length multiplication factor ξ is taken as 1 for all the cases. Eqn. (5.1) can be further simplified as

$$J = \frac{\partial U_f}{\partial A} = J_s + J_p \approx \Phi_G H_G + J_p. \tag{5.3}$$

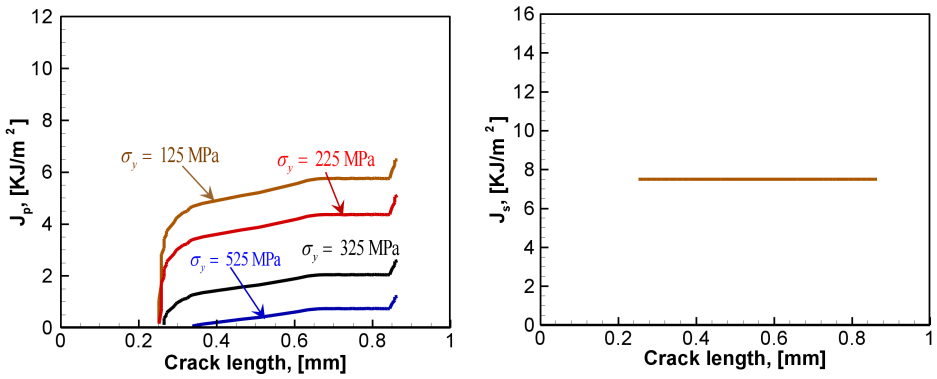

(a) (b)

Fig. 5.5 Separation of J in Fig. 5.3(a) into energy release rate in terms of (a) plastic dissipation and (b) surface formation.

It is obvious that the material response is more ductile under lower yield stress. As shown in Fig. 5.5(a), there is more pronounced plastic energy dissipation as yield stress decreases. The time required for the crack to reach the total projected length W is much longer. It is noted from Fig. 5.5(b) that all the J_s curves eventually saturate at the

same level. Its value indicates the maximum attainable surface energy release rate for this type of microstructure configuration under identical grain and grain boundary properties. The contributions of J_p and J_s on the evolution of *J* are visualized in Fig. 5.6 under four representative yield stress levels. It is worth noting that J_p constitutes most of the *J* at the early state of crack propagation. As the yield stress decreases from 525 MPa to 125 MPa, the initial slope of J_p becomes increasingly steeper and the peak of J_p is reached at an earlier stage of crack propagation. Besides, lower level of yield stress leads to more intensive plastic dissipation since much larger plastic zone is developed ahead of the crack tip. The plastic zone size r_p is reversely correlated with the yield stress σ_y as

$$r_p = \frac{1}{3\pi}\left(\frac{K_I}{\sigma_y}\right)^2, \tag{5.4}$$

where K_I is the mode I stress intensity factor. As the crack continues to grow, the crack tip becomes less sharp than it at the stage of crack initiation, leading to reduced level of stresses in the surrounding materials. As shown in Fig. 5.6, the plateau of *J* is reached at the peak of r_p and the increase of *J* value afterwards is not as prominent as before. It is noted that the material response becomes more brittle when yield stress increases as a lower value of J_{in} is observed. When the yield stress is at 525 MPa, the predicted J_{in} is slightly less than the theoretical value of J_s. This discrepancy might either come from the numerical error in calculation of J or the heterogeneous deformation at the microstructure level. This issue will be further addressed and investigated in the future

studies. It can be inferred that J_p plays a more important role in the toughening of material since the improvement of J_s is quite limited.

5.2.2 Effect of cohesive strength of grains $T_{max}|_G$

In this set of calculations, all the grains share the same yield stress with $\sigma_y =$ 150 MPa . $\Phi_G = \Phi_{GB} = 7.5\,\mathrm{KJ/m^2}$ is employed for cohesive elements in the grains and along the grain boundaries. The maximum cohesive strength along the grain boundaries is fixed as $T_{max}|_{GB} = 350$ MPa , while the grain cohesive strength $T_{max}|_G$ is systematically varies from 100 MPa to 575 MPa with an interval of 25 MPa.

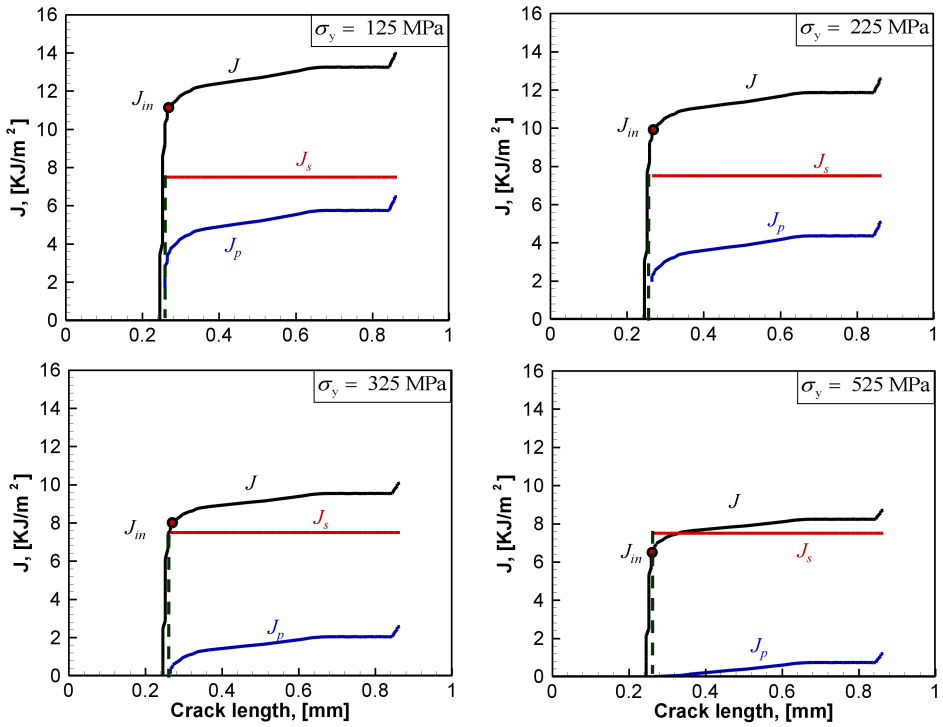

Fig. 5.6 Separation of J_p and J_s under four different yield stress levels.

The CFEM result in Fig. 5.7(a) shows that the increase of $T_{max}\big|_G$ leads to a more torturous crack path as the failure mode gradually changes from pure transgranular fracture to intergranular dominated fracture. Here, L_G/W and L_{GB}/W are defined as the proportion of transgranular fracture and intergranular fracture, respectively. The crack length multiplication factor $\xi = L/W$ is the sum of L_G/W and L_{GB}/W. To visualize the competition between the two failure mechanisms, L_G/W, L_{GB}/W and L/W are plotted against $T_{max}\big|_G$ in Fig. 5.8. The intersection of L_G/W and L_{GB}/W is defined as the threshold for failure mode transition which corresponds to $T_{max}\big|_G \approx 385$ MPa. On the left side of the threshold, transgranular fracture is the dominant failure mode since the red L_G/W curve is always above the blue L_{GB}/W curve. Intergranular fracture becomes the dominant failure mode when $T_{max}\big|_G$ increases beyond the threshold. It is noted from Fig. 5.8 that the value of $T_{max}\big|_G$ yielding maximum J_{IC} is not at the threshold but related to the peak of L/W when $T_{max}\big|_G \approx 425$ MPa. The peak of L/W is achieved with a balanced contribution from L_G/W and L_{GB}/W, leading to the maximized J_s. It is worth noting that the maximization of J_{IC} should also consider the contribution from J_p. J_p continues to decrease as $T_{max}\big|_G$ increases. This is due to the fact that the plastic deformation of the grains is suppressed as more cracks go into the grain boundaries. Although J_p maintains a higher level when $T_{max}\big|_G < 300$ MPa, it is at the cost of J_s as the predominated transgranular fracture keeps L/W at the lowest level as indicated in Fig. 5.8. The best material toughening is achieved at $T_{max}\big|_G \approx 425$ MPa when both transgranular and intergranular fracture are activated.

5.2.3 Effect of cohesive strength of grain boundaries $T_{max}|_{GB}$

The conclusions from the above discussions indicate that the competition between transgranular and intergranular fracture highly depends on the choice of $T_{max}|_{G}$ when $T_{max}|_{GB}$ is fixed. It can be inferred that the determination of the failure mechanism not also depend on the ratio between $T_{max}|_{G}$ and $T_{max}|_{GB}$. In this set of calculations, $T_{max}|_{G} = 425\,\text{MPa}$, which leads to the maximized J_{IC} in Section 5.2.2, is employed as a constant. $T_{max}|_{GB}$ is systematically varies from 100 MPa to 575 MPa with an interval of 25 MPa. Therefore, $T_{max}|_{GB} / T_{max}|_{G}$ considered here spans from 0.24 to 1.4.

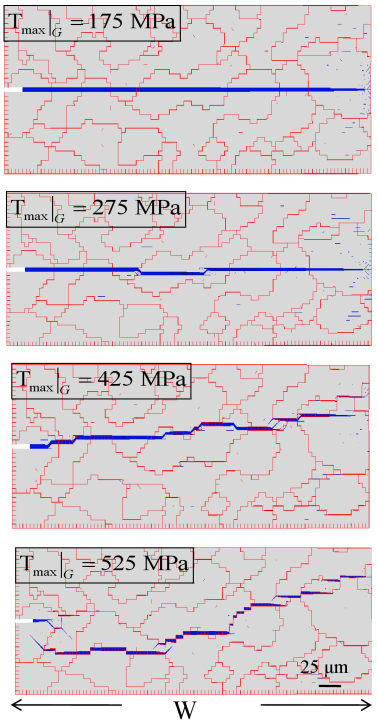

(a)

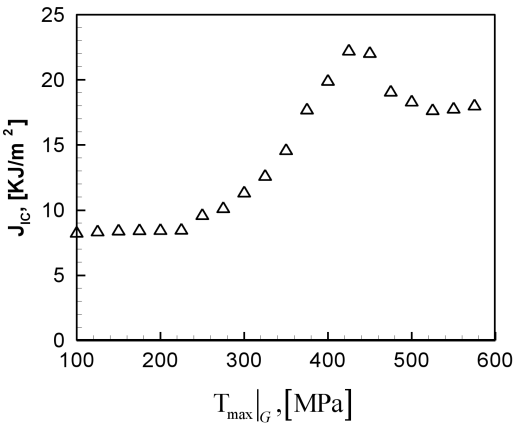

(b)

Fig. 5.7 (a) Crack trajectories and (b) predicted fracture toughness values under different grain cohesive strength $T_{max}\big|_G$.

The transition from intergranular fracture to transgranular fracture is observed as $T_{max}\big|_{GB}$ increases in Fig. 5.(a). Specifically, when $T_{max}\big|_{GB} / T_{max}\big|_G < 0.5$, the crack primarily grows along the grain boundaries. As shown in Fig. 5., L_G/W is negligible compared with L_{GB}/W. Crack surfaces are created with relatively low level of plastic dissipation. When $0.5 < T_{max}\big|_{GB} / T_{max}\big|_G < 1$, both transgranular and intergranular fracture modes are observed. Although the damage prefers to initiate along the grain boundaries, more microcracks formed there start to propagate to the neighboring grains leading to more significant bulk plastic deformation. As shown in Fig. 5., the value of $T_{max}\big|_{GB}$ that corresponds to the threshold of the failure mode is around 425 MPa, which is exactly the prescribed $T_{max}\big|_G$. Further increase of $T_{max}\big|_{GB} / T_{max}\big|_G > 1$ directs the crack to go through grains with a more straight path.

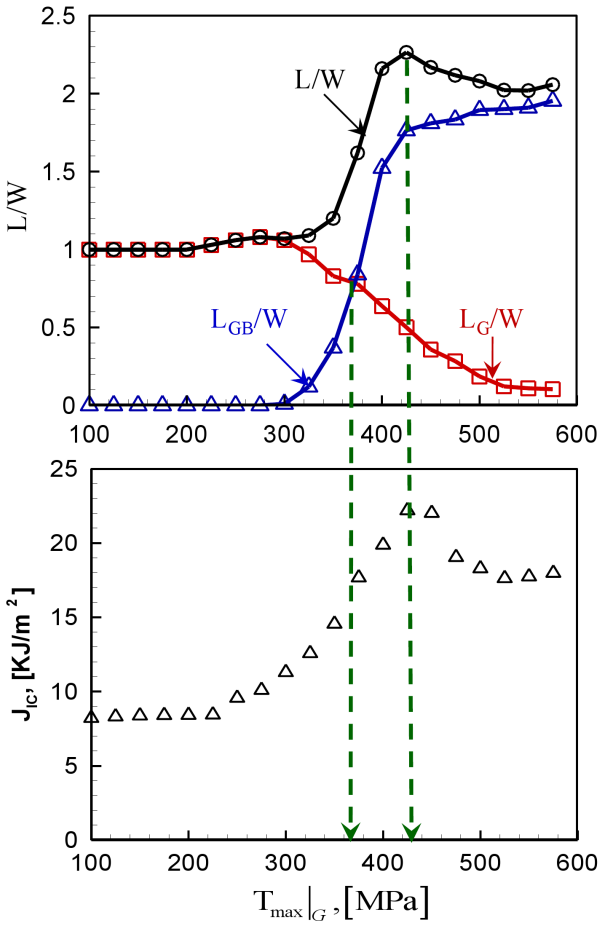

Fig. 5.8 Illustration of the competition between transgranular fracture and intergranular fracture and the influence on the fracture toughness.

It is noted in Fig. 5.(b) that $T_{max}|_{GB} \approx 400$ MPa corresponds to both the peak of L/W and J_{IC}. This trend is in consistence with the result shown in Fig. 5.8. Although the best toughening is achieved at the maximized J_s, it does not mean that the creation of more crack surface areas can always lead to higher fracture resistance. In fact, the maximization of J_s requires the crack to propagates to both the grains and grain boundaries, allowing J_p to be optimized at the same time. The plastic dissipation is more pronounced under the mixed transgranular and intergranular fracture mode. When

intergranular fracture is the predominant ($T_{max}|_{GB} = 175$ MPa), the blunting and propagation of the precrack is suppressed as the damage preferably initiates at the grain boundaries and develops into microcracks. These microcracks quickly coalesce with each other with little plastic deformation. The calculated J_p is at the lowest level compared with the other three cases. On the other hand, when transgranular fracture is the only failure mode ($T_{max}|_{GB} = 575$ MPa), the plastic deformation primarily occurs near the crack tip region due to crack blunting. Therefore, the localized plastic energy dissipation results in lower J_p compared with the mixed fracture mode case ($T_{max}|_{GB} = 250$ and 400 MPa).When mixed failure mode is activated, microcracks from the grain boundaries tend to propagate into the neighboring grains, causing more dispersed stress concentrations and larger amount of plastic dissipation. The increase of $T_{max}|_{GB}$ from 250 MPa to 400 MPa promotes more microcracks to grow into the grains, leading to increased crack surfaces and plastic dissipation at the same time. This explains why the maximum J_{IC} is reached at $T_{max}|_{GB} \approx 400$ MPa with $T_{max}|_{GB} / T_{max}|_{G} \approx 0.94$.

5.3 Competing Mechanisms in 3D Polycrystalline Metals

A preliminary study of the competition between transgranular and intergranular fracture is conducted using the 3D crystal plasticity based CFEM framework as discussed in Section 2.4. The analyze focuses on Ti-6Al-4V alloy using the microstructure generated from Section 3.5. To simplify the analysis, all grains are assumed to share the same mechanical properties except initial orientations which are randomly assigned.

Besides, the cohesive elements in the grains and grain boundaries follow the same traction-separation law, so that they are equally likely to fracture on one account.

Under conditions of small-scale yielding, the fracture energy Φ of Ti-6Al-4V is $\Phi = J = \left(1-\nu^2\right) K_{IC}^2 / E = 9.58\,\text{KJ/m}^2$, with the Young's modulus $E = 114.62\,\text{GPa}$, Poisson's ratio $\nu = 0.322$, and the fracture toughness $K_{IC} = 35\,\text{MPa}\sqrt{\text{m}}$. The maximum traction $T_{\max}$ is obtained from $T_{\max} = \dfrac{2\Phi}{\Delta_{nc}} = \dfrac{2\Phi}{\alpha\Delta_{tc}}$, where α is defined as $\Delta_{nc} / \Delta_{tc}$ and is assumed to be 1. In order for the cohesive surfaces to achieve complete debonding, both the normal and shear separations should not exceed the element size. Otherwise, the cohesive surfaces would not fully debond and the damage cannot be considered true crack formation. In our model, $\Delta_{nc} = \Delta_{tc} \in (1,10)\ \mu\text{m}$ is a reasonable range for the separation. The corresponding range of $T_{\max}$ calculated from the above relations is $1.916 - 19.16\,\text{GPa}$. For the specific case considered, $T_{\max} = 16\,\text{GPa}$ is employed for all three directions.

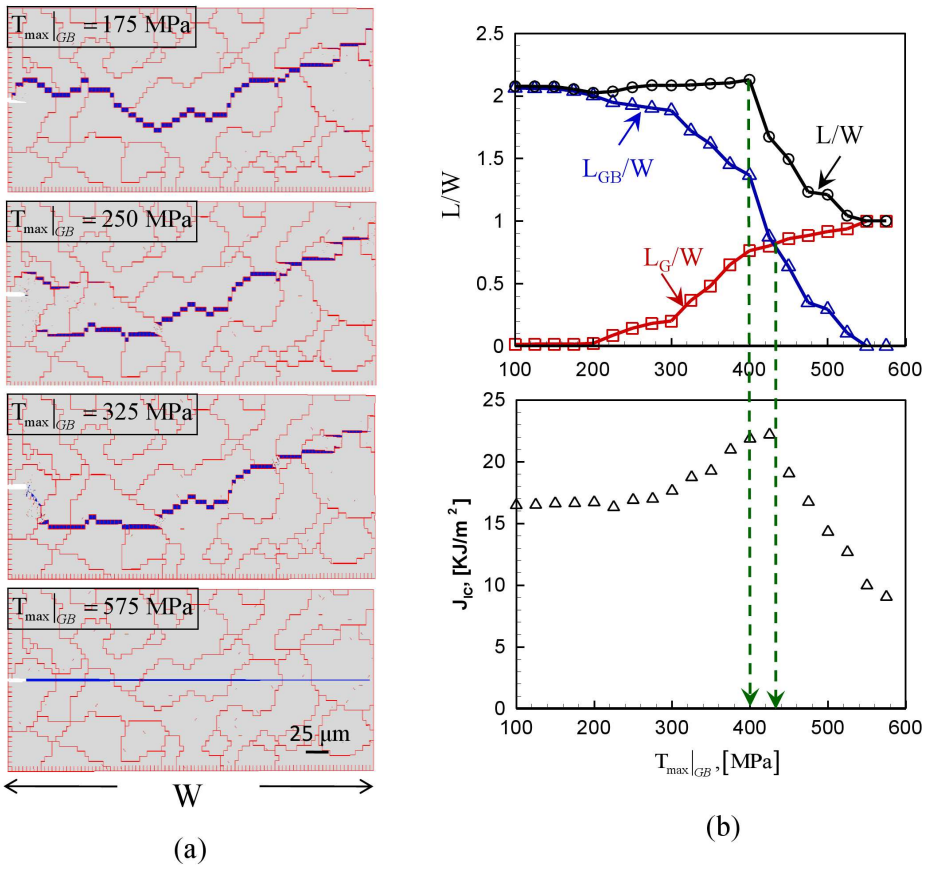

Fig. 5.9 Illustration of (a) crack trajectory under various $T_{max}|_{GB}$ when $T_{max}|_{G}$ is fixed as 415 MPa and their (b) influence on the competition between failure mechanisms and fracture toughness.

It is noted from Fig. 5.9(a) that multiple cracks are observed in the microstructure region. When mapping the deformed nodal coordinates to the grain arrangement illustrated in Fig. 5.9(b), we notice that transgranular fracture is the dominant failure mode. Even though the grains and grain boundaries are equally likely to fracture (as the chosen condition for the analysis carried out here), the cracks tend to go through the grains instead of following the grain boundaries. Besides, most of the cracks do not follow the plane of the pre-crack and instead initiate away from it. To shed light on this

issue, a calculation is carried out without the pre-crack and the cohesive elements in the microstructure. The result is shown in Fig. 5.9(c). Again, cracks tend to nucleate and propagate in grains with lower levels of plastic deformation. The excessive strain energy which cannot be dissipated through plastic deformation has to be released through surface creation. The propagation of the pre-crack is temporarily restrained due to the significant plastic deformation in front of the crack-tip as illustrated in Fig. 5.9(c). Instead, microcracks nucleate and propagate into grains with less plastic deformation. This example well explains the competition between material deformation and crack formation.

Compared with the 2D work, the 3D CFEM model experiences more numerical challenges in terms of computational complexity and convergence. First of all, fracture analysis in polycrystalline metals is a nonlinear problem. Part of the nonlinearity comes from the softening portion of the cohesive law, which results in a decrease in the stiffness of the structure and difficulty in convergence. This issue becomes more pronounced when cohesive elements are embedded everywhere in the microstructure region. Besides, the cohesive forces along the crack depend on the actual stress in the bulk material. The solution of a nonlinear problem when both fracture and plastic deformation are present requires a smaller time increments and larger number of iterations using the Newton-Raphson (N-R) scheme. In addition, the mesh tie constraints also add complexity of the model.

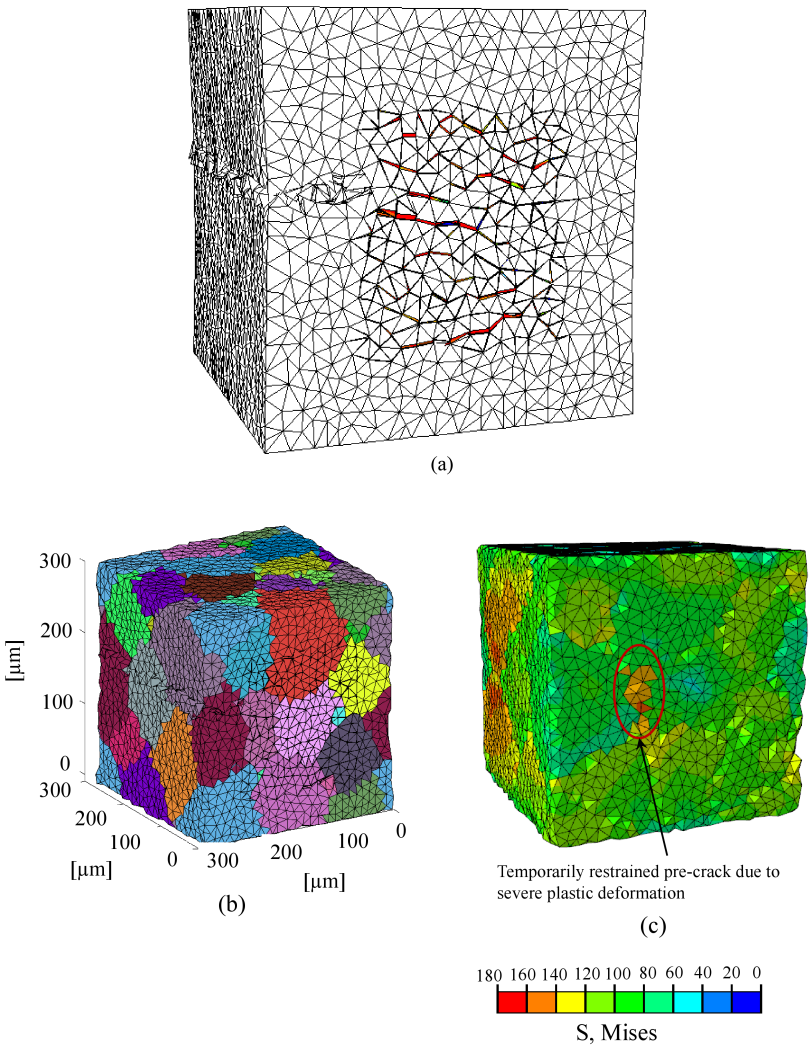

Fig. 5.9 (a) Illustration of crack propagation in the microstructure (b) Mapping of deformed configuration in the microstructure (c) Anisotropic deformation in the microstructure region without pre-crack and cohesive elements.

A common technique to overcome some of these convergence difficulties is the use of viscous regularization of the constitutive equations [113, 114]. The traction-separation laws can be regularized using viscosity by permitting stresses to be outside the limits set by the traction-separation law, which causes the tangent stiffness matrix of the softening material to be positive for sufficiently small time increments [115].

The regularization process involves the use of a viscous stiffness degradation variable, D_v , which is defined by the evolution equation

$$\dot{D}_v = \frac{1}{\mu}\left(D - D_v\right) \tag{5.5}$$

where μ is the viscosity parameter representing the relaxation time of the viscous system and *D* is the degradation variable evaluated in the current cohesive model.

The current viscous stiffness degradation variable is calculated through

$$D_v\left(t+dt\right) = \frac{\left[D_v\left(t\right) + \frac{dt}{\mu} D\left(t+dt\right)\right]}{1+\frac{dt}{\mu}}. \tag{5.6}$$

with $D \in [0,1]$, $D_v \in [0,1]$ and $D_v < D$.

Using viscous regularization with a small value of the viscosity parameter (small compared to the characteristic time increment) helps improve the rate of convergence of the model in the softening regime, without compromising results [115]. In current calculations value of the viscosity parameter $\mu = 10^{-6}$ is employed as part of the section controls definition.

The subsequent work in future publications will focus on establishing the quantitative correlation between fracture toughness, grain orientation and grain size.

1. Both initiation and propagation fracture toughness will be predicted for grains with systematically varied orientations. The objective is to find out whether

grain oriented for easy slip or hard slip will help improve the fracture toughness. The competition between crack initiation/propagation and plastic deformation under different grain orientations will be systematically studied.

2. The grain size effect on fracture toughness will be considered in the above study using microstructures generated in Section 3.5.
3. Based on the study 1 and 2, a criterion which determines the activation of either transgranular fracture or intergranular fracture when the crack is interacting with the grain boundary will be developed. Microstructural attributes, such as grain size, orientation and two-point correlation parameters regarding the microstructure will be included in the criterion. The ultimate goal is to develop a 3D semi-analytical model which allows prediction of fracture toughness from the microstructure attributes.

5.4 Summary

Fracture resistance in ductile materials is the combined effect of the plastic dissipation and the energy spent in creating new surfaces. The separation of the two energy dissipations plays a key role in understanding the competition between different failure mechanisms and their influence on the fracture toughness. A Cohesive Finite Element Method (CFEM) based multiscale framework is introduced to analyze the two energy contributions separately. The global energy release rate and the fracture toughness of ductile materials are predicted by calculating the *J*-integral in the homogenized region. The fracture surface energy for different type of failure mechanism is evaluated through explicit simulation of crack propagation in the microstructure region. The calculations carried out here primarily concern AZ31 Mg alloy and focus on the competition between

deformation and crack formation as well as competition between transgranular and intergranuar fracture. Results indicate that the mixed transgranular and intergranular failure can lead to enhanced fracture toughness.

To simplify the model, the above calculation in Ti-6Al-4V does not distinguish the grains and grain boundaries since identical cohesive laws are employed for both places. It should be inferred from the previous studies that intergranular fracture will be more pronounced if lower cohesive strength and fracture energy are employed in the grain boundary. Transgranular fracture will be prevalent vice versa. To accurately describe the fracture behavior in Ti-6Al-4V, different bulk and cohesive properties should be employed in α and β regions. These issues will be addressed in the future studies.

The framework developed here can be used to account for the effect of precipitates in metal alloys without the need to explicitly resolve the geometry in the FEM model. Their effect could be included in the bulk and cohesive parameters as function of precipitate size, volume fraction, and shape, etc.

6 SUMMARY AND CONCLUSIONS

6.1 Significance of Contribution

The evaluation of macroscopic material parameters such as fracture toughness as functions of microstructural attributes is a fundamental issue in material science. The task requires the quantification of both microstructure and material response. Currently, no systematic approach other than experiments exists for establishing microstructure-fracture toughness relations for materials. A cohesive finite element method (CFEM) based multiscale framework is developed to predict fracture toughness of materials as a function of microstructure. This framework provides a means for evaluating fracture toughness through explicit simulation of fracture processes in microstructures. The approach uses the *J*-integral, allowing fracture toughness to be calculated for microstructures with random heterogeneous phase distributions and fracture processes with arbitrary crack paths or micro-crack patterns. This framework can be applied to both 2D and 3D problems for any material system.

Results show that microstructure and constituent properties can significantly influence fracture behavior and combine to determine the overall fracture toughness through the activation of different fracture mechanisms. For brittle materials, such as Al_2O_3/TiB_2 composite considered in the study, the toughening is achieved through increases in energy dissipation when cracks are forced to follow tortuous paths. The competition between crack deflection and reinforcement penetration plays the most important role in determining the dominant fracture mode and in turn the fracture toughness. CFEM results show that a combination of fine microstructure size scale,

rounded reinforcement morphology, appropriately balanced interphase bonding strength and compliance can best promote desirable crack-reinforcement interactions and lead to enhanced fracture toughness. A semi-analytical model, which is developed based on the CFEM results, provides deeper insights into the fracture process as it quantitatively predicts the proportion of each fracture mechanism in the heterogeneous microstructure.

The CFEM framework is also employed to analyze the microstructure-fracture toughness relations in polycrystalline metals. In contrast with the brittle materials, fracture resistance in ductile materials is the combined effect of the plastic dissipation and the energy spent in creating new surfaces. The calculation of *J*-integral alone could not separate the two energy contributions. Therefore, it impedes understanding of the competing mechanisms between deformation and fracture as well as the competition between transgranular and intergranular fracture. The CFEM framework allows explicit tracking of transgranular and intergranular fracture in the microstructure by embedding cohesive surfaces along all the edges of bulk element as an intrinsic part of material characterization. Therefore, the energy dissipation rate in terms of surface formation can be evaluated directly by measuring the corresponding crack length. The plastic energy dissipation rate can be obtained as the difference between the *J* value and the surface energy dissipation rate. Results indicate that the mixed transgranular and intergranular failure can lead to enhanced fracture toughness. Microstructures with refined grain size and grain boundary bonding strength can best promote the favorable failure mechanisms.

The entire design process for both material systems have been encapsulate into a software. The software allows the user to choose the best microstructure which leads to improved fracture toughness with optimized combination of constitutive behavior, phase

morphology, phase distribution, phase size, and interphase bonding. This innovation has been documented through invention disclosures at Georgia Tech [116, 117].

6.2 Future Directions

There are a number of avenues to extend this research in the areas of mechanics of materials and advanced manufacturing.

The research work in this thesis could be used as the starting point for a probabilistic multiscale approach that incorporates the effects of microstructure, time-dependent inhomogeneous plastic deformation and micro-damage mechanisms in reliability design. Although the current framework can predict material fracture toughness from a specific microstructure configuration, it does not have the capability to predict the fracture toughness scattering based on microstructural information, such as the phase size, volume fraction and interfacial properties, etc. A systematic study which correlating the key microstructure attributes with weibull distribution parameters would lead to a more reliable microstructure sensitive design. Besides, the study in ductile materials could be extended to consider more physically based plastic deformation mechanism. For example, the plastic deformation can originate from slip-mediated dislocation, deformation twinning, grain boundary sliding and phase transformation, etc. The quantification of the contribution from each source can help us better understand the competition between plastic deformation and crack surface formation.

Although the current 3D analysis employs idealized polycrystalline microstructures, the method developed allows actual morphological features and crystallographic orientations to be incorporated through experimental investigations

involving serial sectioning and electron backscatter diffraction (EBSD). The reconstructed 3D digital microstructure will be directly implemented in finite element models for further analyses. In addition to structural materials, this methodology can be applied to bio-materials and geo-materials through constitutive modeling and parameter calibration.

There are good research connections between the 3D CFEM framework and the advanced manufacturing techniques, such as 3D printing and the emerging 4D printing. The 3D microstructures in this research are reconstructed from 2D images. Therefore, the 2D morphological microstructure information could be used as input for the 3D printing which essentially fabricates materials layer by layer. It will be an innovative way for visualization and functional prototype testing. This method could be used as a valuable tool for evaluating the material designs from computational models. Conversely, the computational tools can help exploring the current issues in 3D printing, such as limited material selection, limited quality of printed objects, and safety of the materials processing. This research will have the most impact on products that are made in small volumes, require high customization, and are more cost-effective.

REFERENCES

[1] T. L. Anderson, *Fracture Mechanics: Fundamentals and Applications, Third Edition*: Taylor & Francis, 2005.

[2] Y. Nishiyama, K. Onizawa, and M. Suzuki, "Phosphorus segregation and intergranular embrittlement in thermally aged and neutron irradiated reactor pressure vessel steels," *Journal of ASTM International,* vol. 4, 2007.

[3] D. A. Curry and J. F. Knott, "The relationship between fracture toughness and microstructure in the cleavage fracture of mild steel," *Met. Sci.*, vol. 10, pp. 1-6, 1976.

[4] D. Casellas, M. M. Nagl, L. Llanes, and M. Anglada, "Fracture toughness of alumina and ZTA ceramics: microstructural coarsening effects," *J. Mater. Process. Tech.*, vol. 143-144, pp. 148-152, 2003.

[5] J. N. Hall, J. W. Jones, and A. K. Sachdev, "Particle-Size, Volume Fraction and Matrix Strength Effects on Fatigue Behavior and Particle Fracture in 2124 Aluminum-Sicp Composites," *Mater. Sci. Eng., A,* vol. 183, pp. 69-80, Jun 15 1994.

[6] T. I. Zohdi and P. Wriggers, *An Introduction to Computational Micromechanics*: Springer, 2008.

[7] J. Leszczynski and M. Shukla, *Practical Aspects of Computational Chemistry: Methods, Concepts and Applications*: Springer, 2009.

[8] M. F. Horstemeyer, "Multiscale Modeling: A Review," *Practical Aspects of Computational Chemistry, ed. J. Leszczynski and M.K. Shukla, Springer Science+Business Media,* pp. 87-135, 2009.

[9] M. F. Horstemeyer and D. J. Bammann, "Historical review of internal state variable theory for inelasticity," *International Journal of Plasticity*, vol. 26, pp. 1310-1334, Sep 2010.

[10] R. Talreja, "Continuum Modeling of Damage in Ceramic Matrix Composites," *Mechanics of Materials*, vol. 12, pp. 165-180, Oct 1991.

[11] B. A. Gailly and H. D. Espinosa, "Modelling of failure mode transition in ballistic penetration with a continuum model describing microcracking and flow of pulverized media," *International Journal for Numerical Methods in Engineering*, vol. 54, pp. 365-398, 2002.

[12] C. Yoon and D. H. Allen, "Damage dependent constitutive behavior and energy release rate for a cohesive zone in a thermoviscoelastic solid," *International Journal of Fracture*, vol. 96, pp. 55-74, 1999.

[13] X. H. Chen, "Coupled hygro-thermo-viscoelastic fracture theory," *International Journal of Fracture*, vol. 148, pp. 47-55, Nov 2007.

[14] D. X. Leng, L. Y. Sun, D. Y. Hu, and Y. Lin, "A Bottom-up Simulation for Impact Fracture Behavior of Nanoparticle-Reinforced Composites," *Environmental Biotechnology and Materials Engineering, Pts 1-3*, vol. 183-185, pp. 2308-2312, 2011.

[15] A. Rinaldi, "Bottom-up modeling of damage in heterogeneous quasi-brittle solids," *Continuum Mechanics and Thermodynamics*, vol. 25, pp. 359-373, 2013/03/01 2013.

[16] P. Gumbsch, "An atomistic study of brittle fracture: Toward explicit failure criteria from atomistic modeling," *Journal of Materials Research,* vol. 10, pp. 2897-2907, 1995.

[17] R. E. Rudd and J. Q. Broughton, "Coarse-grained molecular dynamics and the atomic limit of finite elements," *Physical Review B,* vol. 58, pp. R5893-R5896, Sep 1 1998.

[18] R. E. Rudd and J. Q. Broughton, "Coarse-grained molecular dynamics: Nonlinear finite elements and finite temperature," *Physical Review B,* vol. 72, Oct 2005.

[19] R. E. Miller and E. B. Tadmor, "The quasicontinuum method: Overview, applications and current directions," *Journal of Computer-Aided Materials Design,* vol. 9, pp. 203-239, 2002.

[20] J. Q. Broughton, F. F. Abraham, N. Bernstein, and E. Kaxiras, "Concurrent coupling of length scales: Methodology and application," *Physical Review B,* vol. 60, pp. 2391-2403, Jul 15 1999.

[21] Z. P. Bazant, "Can Multiscale-Multiphysics Methods Predict Softening Damage and Structural Failure?," vol. 8, pp. 61-67, 2009-09-22 2010.

[22] J. Zhai, V. Tomar, and M. Zhou, "Micromechanical Simulation of Dynamic Fracture Using the Cohesive Finite Element Method," *J. Eng. Mater. Technol.,* vol. 126, pp. 179-191, 2004.

[23] Y. Li and M. Zhou, "Prediction of fracture toughness of ceramic composites as function of microstructure: I. Numerical simulations," *Journal of the Mechanics and Physics of Solids,* vol. 61, pp. 472-488, Feb 2013.

[24] Y. Li and M. Zhou, "Prediction of fracturess toughness of ceramic composites as function of microstructure: II. analytical model," *Journal of the Mechanics and Physics of Solids,* vol. 61, pp. 489-503, Feb 2013.

[25] C. Yu, "Three-Dimensional Cohesive Modeling of Impact Damage of Composites," Ph.D. Thesis, Caltech,Pasadena,CA, 2001.

[26] A. Pandolfi and M. Ortiz, "An Efficient Adaptive Procedure for Three-Dimensional Fragmentation Simulations," *Eng. Comput,* vol. 18, pp. 148-159, 2002.

[27] A. Needleman, "An Analysis of Tensile Decohesion Along an Interface," *Journal of the Mechanics and Physics of Solids,* vol. 38, pp. 289-324, 1990.

[28] X. P. Yu and A. Needleman, "Numerical simulations of dynamic interfacial crack growth allowing for crack growth away from the bond line," *International Journal of Fracture,* vol. 74, pp. 253-275, 1996.

[29] X. P. Xu and A. Needleman, "Numerical simulations of dynamic interfacial crack growth allowing for crack growth away from the bond line," *International Journal of Fracture,* vol. 74, pp. 253-275, 1985/08/01 1985.

[30] J. Zhai, V. Tomar, and M. Zhou, "Micromechanical simulation of dynamic fracture using the cohesive finite element method," *Journal of engineering materials and technology,* vol. 126, pp. 179-191, 2004.

[31] V. Tomar, J. Zhai, and M. Zhou, "Bounds for element size in a variable stiffness cohesive finite element model," *Int. J. Numer. Meth. Eng.,* vol. 61, pp. 1894-1920, Nov 21 2004.

[32] G. T. Camacho and M. Ortiz, "Computational modelling of impact damage in brittle materials," *Int. J. Solids. Struct.,* vol. 33, pp. 2899-2938, Aug 1996.

[33] M. Ortiz and A. Pandolfi, "Finite-deformation irreversible cohesive elements for three-dimensional crack-propagation analysis," *Int. J. Numer. Meth. Eng.,* vol. 44, pp. 1267-1282, Mar 30 1999.

[34] H. D. Espinosa, S. Dwivedi, and H. C. Lu, "Modeling impact induced delamination of woven fiber reinforced composites with contact/cohesive laws," *Comput. Method. Appl. M.,* vol. 183, pp. 259-290, 2000.

[35] K. Wallin, "The Scatter in KIC-Results," *Eng. Fract. Mech.,* vol. 19, pp. 1085-1093, 1984.

[36] X. P. Xu and A. Needleman, "Numerical Simulations of Fast Crack-Growth in Brittle Solids," *J. Mech. Phys. Solids,* vol. 42, p. 1397, Sep 1994.

[37] K. V. Logan, "Composite Ceramics, Final Tehnical Report, final technical report," ed: USSTACOM DAAEO7-95-C-R040, 1996.

[38] S. M. Wiederhorn, "Brittle-Fracture and Toughening Mechanisms in Ceramics," *Annu. Rev. Mater. Sci.,* vol. 14, pp. 373-403, 1984.

[39] J. R. Mayeur, D. L. McDowell, and R. W. Neu, "Crystal plasticity simulations of fretting of Ti-6Al-4V in partial slip regime considering effects of texture," *Computational Materials Science,* vol. 41, pp. 356-365, 2008.

[40] J. D. Clayton and D. L. McDowell, "Homogenized finite elastoplasticity and damage: theory and computations," *Mechanics of Materials,* vol. 36, pp. 799-824, Sep 2004.

[41] S. Y. Li, P. Van Houtte, and S. R. Kalidindi, "A quantitative evaluation of the deformation texture predictions for aluminium alloys from crystal plasticity finite element method," *Modelling and Simulation in Materials Science and Engineering,* vol. 12, pp. 845-870, Sep 2004.

[42] A. Siddiq and S. Rahimi, "A multiscale constitutive model for intergranular stress corrosion cracking in type 304 austenitic stainless steel," *International Symposium on Dynamic Deformation and Fracture of Advanced Materials (D2fam 2013),* vol. 451, 2013.

[43] P. Zhang, M. Karimpour, D. Balint, and J. Lin, "Cohesive zone representation and junction partitioning for crystal plasticity analyses," *International Journal for Numerical Methods in Engineering,* vol. 92, pp. 715-733, Nov 23 2012.

[44] A. Siddiq and S. Schmauder, "Multiscale Simulation of Metal/Ceramic Interface Fracture," *Iutam Symposium on Multi-Functional Material Structures and Systems,* vol. 19, pp. 343-355, 2010.

[45] M. Grujicic, G. Cao, and S. Batchu, "Crystal plasticity-based finite element analysis of deformation and fracture of polycrystalline lamellar gamma-Tial + alpha(2)-Ti(3)al alloys," *Journal of Materials Science,* vol. 38, pp. 307-322, Jan 15 2003.

[46] Q. Q. Fang and D. A. Boas, "Tetrahedral Mesh Generation from Volumetric Binary and Gray-Scale Images," *2009 Ieee International Symposium on Biomedical Imaging: From Nano to Macro, Vols 1 and 2,* pp. 1142-1145, 2009.

[47] "ABAQUS integration with CATIA V5," *Aircraft Engineering and Aerospace Technology,* vol. 74, pp. 574-575, 2002.

[48] J. R. Mayeur and D. L. McDowell, "A three-dimensional crystal plasticity model for duplex Ti-6Al-4V," *International Journal of Plasticity,* vol. 23, pp. 1457-1485, 2007.

[49] P. Sisodia and M. P. Verma, "Polycrystalline Elastic-Moduli of Some Hexagonal and Tetragonal Materials," *Physica Status Solidi a-Applied Research,* vol. 122, pp. 525-534, Dec 16 1990.

[50] F. Qianqian and D. A. Boas, "Tetrahedral mesh generation from volumetric binary and grayscale images," in *Biomedical Imaging: From Nano to Macro, 2009. ISBI '09. IEEE International Symposium on*, 2009, pp. 1142-1145.

[51] G. I. Taylor, "Plastic strain in metals.," *Journal of the Institute of Metals,* vol. 62, pp. 307-324, 1938.

[52] R. Hill and J. R. Rice, "Constitutive analysis of elastic-plastic crystals at arbitrary strain," *Journal of the Mechanics and Physics of Solids,* vol. 20, pp. 401-413, 1972.

[53] R. J. Asaro and J. R. Rice, "Strain Localization in Ductile Single-Crystals," *Journal of the Mechanics and Physics of Solids,* vol. 25, pp. 309-338, 1977.

[54] D. Peirce, R. J. Asaro, and A. Needleman, "An Analysis of Nonuniform and Localized Deformation in Ductile Single-Crystals," *Acta Metallurgica,* vol. 30, pp. 1087-1119, 1982.

[55] R. D. McGinty and D. L. McDowell, "Application of multiscale crystal plasticity models to forming limit diagrams," *Journal of Engineering Materials and Technology-Transactions of the Asme,* vol. 126, pp. 285-291, Jul 2004.

[56] C. P. Przybyla and D. L. McDowell, "Simulated microstructure-sensitive extreme value probabilities for high cycle fatigue of duplex Ti-6Al-4V," *International Journal of Plasticity,* vol. 27, pp. 1871-1895, Dec 2011.

[57] W. Schmitt and T. Hollstein, "Numerical Evaluation of Crack Tip Opening Displacements: 2D and 3D Applications," in *The Crack Tip Opening Displacement in Elastic-Plastic Fracture Mechanics*, K. H. Schwalbe, Ed., ed: Springer Berlin Heidelberg, 1986, pp. 3-20.

[58] W. Brocks, A. Cornec, and I. Scheider, "Computational aspects of nonlinear fracture mechanics," *GKSS FORSCHUNGSZENTRUM GEESTHACHT GMBH-PUBLICATIONS-GKSS,* 2003.

[59] J. Duffy, S. Suresh, K. Cho, and E. R. Bopp, "A Method for Dynamic Fracture Initiation Testing of Ceramics," *J. Eng. Mater. Technol.*, vol. 110, pp. 325-331, Oct 1988.

[60] K. Toshiro, M. Kenji, I. Hideki, and M. Kenya, "Evaluation of static and dynamic fracture toughness in ceramics," *Eng. Fract. Mech.*, vol. 31, pp. 873-885, 1988.

[61] B. Moran and C. F. Shih, "A General Treatment of Crack Tip Contour Integrals," *Int. J. Fracture.,* vol. 35, pp. 295-310, Dec 1987.

[62] T. Nakamura, C. F. Shih, and L. B. Freund, "Computational Methods Based on an Energy Integral in Dynamic Fracture," *Int. J. Fracture.*, vol. 27, pp. 229-243, 1985.

[63] C. Y. Lo and T. Nakamura, "Computational analysis of dynamically propagating cracks in axisymmetric solids," *Int. J. Fracture*, vol. 70, pp. 217-235, 1993.

[64] L. B. Freund, *Dynamic fracture mechanics*: Cambridge University Press, 1998.

[65] T. L. Anderson, *Fracture mechanics: fundamentals and applications*: CRC Press, 1995.

[66] M. Manoharan and S. V. Kamat, "A micro-mechanical model for crack growth resistance of particulate-reinforced metal-matrix composites," *J. Mater. Sci.*, vol. 28, pp. 5218-5222, 1993.

[67] J. G. Berryman and S. C. Blair, "Use of digital image analysis to estimate fluid permeability of porous materials: Application of two-point correlation functions," *J.Appl.Phys.*, vol. 60, p. 1930, 1986.

[68] A. Tewari, A. M. Gokhale, J. E. Spowart, and D. B. Miracle, "Quantitative characterization of spatial clustering in three-dimensional microstructures using two-point correlation functions," *Acta Metall.Mater.* , vol. 52, pp. 307-319, Jan 19 2004.

[69] S. Torquato, Author, H. W. Haslach, Jr, and Reviewer, "Random Heterogeneous Materials: Microstructure and Macroscopic Properties," *Appl. Mech. Rev.*, vol. 55, pp. B62-B63, 2002.

[70] J. C. Russ, *The image processing handbook*: CRC Press, 2007.

[71] O. G. L. S. M. J. Seul M, *Practical Algorithms for Image Analysis: Description, Examples, and Code*: Cambridge University Press: Cambridge, MA, 2000.

[72] D. M. Valiveti and S. Ghosh, "Morphology based domain partitioning of multi-phase materials: A preprocessor for multi-scale modelling," *Int. J. Numer. Meth. Eng.*, vol. 69, pp. 1717-1754, Feb 19 2007.

[73] A. Leonardi, P. Scardi, and M. Leoni, "Realistic nano-polycrystalline microstructures: beyond the classical Voronoi tessellation," *Philosophical Magazine,* vol. 92, pp. 986-1005, 2012/03/11 2012.

[74] T. Luther and C. Könke, "Polycrystal models for the analysis of intergranular crack growth in metallic materials," *Engineering Fracture Mechanics,* vol. 76, pp. 2332-2343, 2009.

[75] T. Xu and M. Li, "Topological and statistical properties of a constrained Voronoi tessellation," *Philosophical Magazine,* vol. 89, pp. 349-374, 2009/02/01 2009.

[76] C. P. Przybyla and D. L. McDowell, "Simulation-based extreme value marked correlations in fatigue of advanced engineering alloys," *Procedia Engineering,* vol. 2, pp. 1045-1056, 2010.

[77] M. Tschopp, "Personal Communication," 2009.

[78] C. P. Przybyla and D. L. McDowell, "Simulated microstructure-sensitive extreme value probabilities for high cycle fatigue of duplex Ti–6Al–4V," *International Journal of Plasticity,* vol. 27, pp. 1871-1895, 2011.

[79] W. Weibull, "A statistical theory of the strength of materials," *Ing. Vetenskaps Akad. Handl.151.,* pp. 1-45, 1939.

[80] K. Wallin, "Macroscopic nature of brittle fracture," *J Phys IV, Colloque C7, Supplément au J Phys III 3 (IV)* pp. 575–584, 1993.

[81] K. Wallin, K. Törrönen, R. Ahlstrand, B. Timofeev, V. Rybin, V. Nikolaev, and A. Morozov, "Theory based statistical interpretation of brittle fracture toughness

of reactor pressure vessel steel 15X2MφA and its welds," *Nuclear Engineering and Design,* vol. 135, pp. 239-246, 1992.

[82] P. Doig, "Evaluation of Lower Bound Fracture-Toughness Values Using Weibull Analysis of Single Specimen Data," *Eng. Fract. Mech.,* vol. 21, pp. 963-967, 1985.

[83] S. Kumai, J. E. King, and J. F. Knott, "Fatigue in Sic-Particulate-Reinforced Aluminum-Alloy Composites," *Mater. Sci. Eng., A,* vol. 146, pp. 317-326, Oct 25 1991.

[84] A. G. Evans, "Perspective on the Development of High-Toughness Ceramics," *J. Am. Ceram. Soc.,* vol. 73, pp. 187-206, 1990.

[85] T. Lin, A. G. Evans, and R. O. Ritchie, "Statistical analysis of cleavage fracture ahead of sharp cracks and rounded notches," *Acta Metall.Mater,* vol. 34, pp. 2205-2216, 1986.

[86] A. S. Kobayashi, M. Ramulu, M. S. Dadkhah, K. H. Yang, and B. S. J. Kang, "Dynamic fracture toughness," *Int. J. Fracture.,* vol. 30, pp. 275-285, 1986.

[87] J. F. M. G. B. Mandell and F. J. McGarry, "Interlaminar Strength and Toughness of Fiberglass Laminates," *The Society of the Plastics Industry, Inc., Washington, D.C.,* pp. 13-C, 1974.

[88] S. Samborski and T. Sadowski, "Dynamic Fracture Toughness of Porous Ceramics Rapid Communications of the American Ceramic Society," *J. Am. Ceram. Soc.,* vol. 93, pp. 3607-3609, 2010.

[89] A. Hauert, A. Rossoll, and A. Mortensen, "Particle fracture in high-volume-fraction ceramic-reinforced metals: Governing parameters and implications for composite failure," *J. Mech. Physics. Solids,* vol. 57, pp. 1781-1800, 2009.

[90] A. Miserez, R. Müller, A. Rossoll, L. Weber, and A. Mortensen, "Particle reinforced metals of high ceramic content," *Mater. Sci. Eng., A,* vol. 387-389, pp. 822-831 2004.

[91] V. Gupta, J. Yuan, and D. Martinez, "Calculation, Measurement, and Control of Interface Strength in Composites," *J. Am. Ceram. Soc.,* vol. 76, pp. 305-315, 1993.

[92] S. G. Warrier, B. S. Majumdar, and D. B. Miracle, "Interface effects on crack deflection and bridging during fatigue crack growth of titanium matrix composites," *Acta Mater.,* vol. 45, pp. 4969-4980, 1997.

[93] M.-Y. He and J. W. Hutchinson, "Crack deflection at an interface between dissimilar elastic materials," *Int. J. Solids. Struct.,* vol. 25, pp. 1053-1067, 1989.

[94] M.-Y. He and J. W. Hutchinson, "Kinking of a Crack Out of an Interface," *J. Appl. Mech.,* vol. 56, pp. 270-278 1989.

[95] E. Martin, D. Leguillon, and C. Lacroix, "A revisited criterion for crack deflection at an interface in a brittle bimaterial," *Compos. Sci. Technol.,* vol. 61, pp. 1671-1679, 2001.

[96] V. Gupta, A. S. Argon, and Z. Suo, "Crack Deflection at an Interface Between Two Orthotopic Media," *J. Appl. Mech.,* vol. 59, pp. S79-S87, 1992.

[97] D. Martínez and V. Gupta, "Energy criterion for crack deflection at an interface between two orthotropic media," *J. Mech. Physics. Solids.,* vol. 42, pp. 1247-1271, 1994.

[98] J. Dundurs, "Edge-Bonded Dissimilar Orthogonal Elastic Wedges Under Normal and Shear Loading," *J. Appl. Mech.,* vol. 36, pp. 650-652 1969.

[99] D. B. Bogy, "Elastostatic solutions on bonded half planes of dissimilar materials," *J. Appl. Mech.,* vol. 37, p. 220, 1970.

[100] A. R. Zak and M. L. Williams, "Crack Point Stress Singularities at a Bi-Material Interface," *J. Appl. Mech.,* vol. 30, pp. 142-143, 1963.

[101] J. R. Rice, "Elastic Fracture Mechanics Concepts for Interfacial Cracks," *J. Appl. Mech.,* vol. 55, pp. 98-103, 1988.

[102] J. Veljkovic, "The crack kinking out of an interface," *Theoret. Appl. Mech.,* vol. 32, pp. 209-221. , 2005.

[103] Evans, F. Zok, and J. Davis, "The role of interfaces in fiber-reinforced brittle matrix composites," *Compos. Sci. Technol.,* vol. 42, pp. 3-24, 1991.

[104] N. Roger R, "The design of the fibre-matrix interfacial zone in ceramic matrix composites," *Composites Part A,* vol. 29, pp. 1145-1155, 1998.

[105] J. P. Parmigiani and M. D. Thouless, "The roles of toughness and cohesive strength on crack deflection at interfaces," *J. Mech. Physics. Solids.,* vol. 54, pp. 266-287, 2006.

[106] J. W. Foulk, G. C. Johnson, P. A. Klein, and R. O. Ritchie, "On the toughening of brittle materials by grain bridging: Promoting intergranular fracture through

grain angle, strength, and toughness," *Journal of the Mechanics and Physics of Solids,* vol. 56, pp. 2381-2400, Jun 2008.

[107] L. S. Sigl, "Microcrack toughening in brittle materials containing weak and strong interfaces," *Acta Materialia,* vol. 44, pp. 3599-3609, 1996.

[108] G. M. Ludtka and D. E. Laughlin, "The Influence of Microstructure and Strength on the Fracture Mode and Toughness of 7xxx Series Aluminum-Alloys," *Metallurgical Transactions a-Physical Metallurgy and Materials Science,* vol. 13, pp. 411-425, 1982.

[109] N. K. Simha, F. D. Fischer, G. X. Shan, C. R. Chen, and O. Kolednik, "J-integral and crack driving force in elastic–plastic materials," *Journal of the Mechanics and Physics of Solids,* vol. 56, pp. 2876-2895, 2008.

[110] X.-K. Zhu and J. A. Joyce, "Review of fracture toughness (G, K, J, CTOD, CTOA) testing and standardization," *Engineering Fracture Mechanics,* vol. 85, pp. 1-46, 2012.

[111] H. Somekawa and T. Mukai, "Fracture toughness in a rolled AZ31 magnesium alloy," *Journal of Alloys and Compounds,* vol. 417, pp. 209-213, 2006.

[112] A. Munitz, R. E. Ricker, D. J. Pitchure, and G. Kimmel, "The influence of thermomechanical treatment on the complex modulus of Mg alloy AZ31," *Metallurgical and Materials Transactions a-Physical Metallurgy and Materials Science,* vol. 36A, pp. 2403-2413, Sep 2005.

[113] Y. Gao and A. Bower, "A simple technique for avoiding convergence problems in finite element simulations of crack nucleation and growth on cohesive

interfaces," *Modelling and Simulation in Materials Science and Engineering*, vol. 12, p. 453, 2004.

[114] H. Jiang, "Cohesive Zone Model for Carbon Nanotube Adhesive Simulation and Fracture/Fatigue Crack Growth," The University of Akron, 2010.

[115] "ABAQUS User's Manual," 2013.

[116] Y. Li, McDowell, D, Zhou, M, "Prediction of material fracture toughness of polycrystalline metals as function of microstructure," *Georgia Tech Invention Disclosure No. 2013-6385*, 2013.

[117] Y. Li, Zhou, M., "Prediction of material fracture toughness of ceramics composites as function of microstructure," *Georgia Tech Invention Disclosure No. 2013-6386*, 2013.